LUND
UNIVERSITY

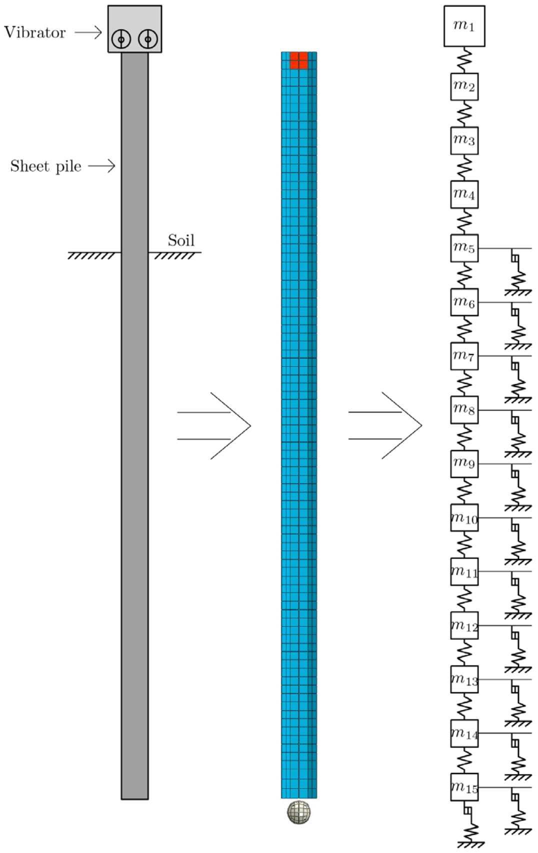

MODELLING AND SIMULATION OF VIBRATORY DRIVEN SHEET PILES

Development of a stop criterion

ANTON ANDERSSON & JOHANNES JONSSON

Structural
Mechanics

Master's Dissertation

DEPARTMENT OF CONSTRUCTION SCIENCES
DIVISION OF STRUCTURAL MECHANICS
ISRN LUTVDG/TVSM--21/5254--SE (1-144) | ISSN 0281-6679
MASTER'S DISSERTATION

MODELLING AND SIMULATION OF VIBRATORY DRIVEN SHEET PILES

Development of a stop criterion

ANTON ANDERSSON & JOHANNES JONSSON

Supervisor: Professor **PER-ERIK AUSTRELL**, Division of Structural Mechanics, LTH.
Assistant Supervisors: Professor **KENT PERSSON**, Division of Structural Mechanics, LTH;
Dr **ERIKA TUDISCO**, Geotechnical Engineering, LTH and Dr **KENNETH VIKING**, Trafikverket .
Examiner: **PETER PERSSON**, Associate Professor, Division of Structural Mechanics, LTH.

Printed by V-husets tryckeri LTH, Lund, Sweden, June 2021 *(Pl)*.

For information, address:
Division of Structural Mechanics,
Faculty of Engineering LTH, Lund University, Box 118, SE-221 00 Lund, Sweden.
Homepage: www.byggmek.lth.se

Abstract

During excavations, steel sheet piles are often installed through vibratory driving, to establish a retaining wall that resists soil instability and ground water leakage. The method of vibratory driving is that the sheet pile is driven into the soil with a vertical vibratory motion. This is especially effective in soft soils. In parts of Sweden, however, the most common type of soil is the glacial till, which is generally compact and contains a large range of grain sizes, where cobbles and boulders are not unusual. Thus, when installing sheet piles in glacial till, there is a risk of impact with objects of high stiffness, which may result in damage to the sheet piles. Any damage to the sheet piles may result in insufficient soil stability and ground water resistance, requiring additional expensive measures to regain it. Hence, there is a need for a stop criterion that can be used to detect these hazardous situations, and that stops the driving before the sheet pile is severely damaged. The purpose of the dissertation is to investigate how numerical models may be used to simulate a situation where a sheet pile encounters a boulder during vibratory driving, and to investigate the possibility of developing a stop criterion based on these numerical models.

Three different numerical models were created to simulate the vibratory driving: a single degree of freedom (SDOF) model, a uniaxial multi degree of freedom (MDOF) model, and a finite element (FE) model. The SDOF model and uniaxial MDOF model was created and simulated using the numeric computing platform MATLAB. The FE model was created and simulated using the FE analysis software Abaqus. The simulations were carried out through explicit time integration in all three models. The external actions on the sheet pile, i.e., the vibrator force, soil resistances and obstacle resistances were estimated with methods found in literature. The models were then calibrated against a field study by using the results from that field study as input in the models. The encounter with a rigid object (boulder), was simulated in different ways. In the SDOF model and uniaxial MDOF model, the encounter was simulated with an elasto-plastic contact force. In the FE model, a solid body with high stiffness representing a boulder was introduced, and the encounter was simulated by driving the sheet pile into the solid body, resulting in repeated impacts.

The results of the numerical models show promising resemblance with the results of the field study. Both the global driving speeds and the accelerations of the sheet pile corresponds well with the reference case for all three models. This suggests that rather simple numerical models may be used to simulate vibratory driving of sheet piles. In addition, the simulations indicate that impacts may be detected through abrupt changes in acceleration amplitude along the sheet pile, created from the compression waves ensuing an impact. This suggest that a future stop criterion for vibratory driving could be based on a change in acceleration amplitude. Such a stop criterion could be enforced by attaching accelerometers to the sheet piles, and creating a system that will cease the driving when a significant increase in acceleration amplitude is detected.

Sammanfattning

Vid markarbeten installeras stålspont ofta genom vibrationdriving, för att åstadkomma en stödkonstruktion som motverkar jordras och grundvattenläckage. Vibrationsdrivning innebär att sponten drivs ner i jorden med en vertikal vibrationsrörelse. Detta är framför allt effektivt vid drivning i lättpackade jordar. I delar av Sverige är dock den vanligast förekommande jordarten morän, som generellt är väldigt kompakt och innehåller ett stort intervall av kornstorlekar, där stenar och block inte är ovanligt förekommande. Således, vid drivning i morän finns det en risk för kollision med objekt av hög styvhet som kan orsaka skada på sponten. Därför finns det ett behov av ett stoppkriterium som kan upptäcka dessa riskfyllda situationer och stoppa drivningen innan sponten tar allvarlig skada. Syftet med detta examensarbete är att undersöka ifall numeriska modeller kan användas till att simulera en situation där en vibrationsdriven spont kolliderar med ett block, och att undersöka möjligheten att utveckla ett stoppkriterium utifrån dessa numeriska modeller.

Tre olika numeriska modeller skapades för att simulera vibrationsdrivningen: en single degree of freedom (SDOF)-modell, en enaxiell multi degree of freedom (MDOF)-modell, och en finita element (FE)-modell. De två förstnämnda modellerna skapades och simulerades i det numeriska beräkningsprogrammet MATLAB, medan den sistnämnda modellen skapades och simulerades i FE-programmet Abaqus. Simuleringarna genomfördes med explicit tidsintegration i alla tre modeller. Yttre laster som påverkar sponten, det vill säga vibrationskrafter, jordmotstånd och motstånd från ett stenblock, beräknades med metoder från litteratur. Modellerna kalibrerades sedan mot en fältstudie genom att använda fältstudiens förutsättningar som ingångsvärden i modellerna. Kollisioner med styva objekt, som ett block, simulerades med olika metoder. I SDOF-modellen och den enaxiella MDOF-modellen simulerades kollisioner med en elastoplastisk kontaktkraft. I FE-modellen skapades en solid kropp med hög styvhet som efterliknade ett block, och kollisioner simulerades genom att driva en spont in i blocket.

Resultaten från de numeriska modellerna visar lovande likheter med fältförsöket. Alla de tre modellerna uppvisar globala neddrivingshastigheter och accelerationer som stämmer väl överens med resultaten från fältförsöket. Detta indikerar att förhållandevis enkla modeller kan användas för att simulera vibrationsdrivining av stålspont. Vidare visar simuleringarna att kollisioner sannolikt kan detekteras genom plötsliga förändringar i accelerationsamplitud längs med sponten. Detta indikerar att ett framtida stoppkriterium för vibrationsdrivning skulle kunna baseras på förändringar i accelerationsamplitud. Ett sådant stoppkriterium skulle kunna implementeras praktiskt genom att fästa accelerometrar på sponten och skapa ett system där vibrationsdrivningen avbryts när en signifikant ökning av accelerationsamplitud detekteras.

Acknowledgements

This master's dissertation was carried out at the Division of Structural Mechanics at LTH, Lund University, from January to June 2021.

We would like to extend our greatest thanks to our supervisor Professor Per-Erik Austrell at the Division of Structural Mechanics, LTH, who contributed with the original idea of how to establish the models, along with guidance and support throughout the work with the dissertation. We also thank our assistant supervisors: Professor Kent Persson at the Division of Structural Mechanics, LTH, Dr Erika Tudisco at the Division of Geotechnical Engineering, LTH, and Dr Kenneth Viking at Trafikverket for valuable input and guidance.

Finally, thanks to our friends and families who have supported us throughout our time at LTH.

Lund, June 2021
Anton Andersson & Johannes Jonsson

Notations and symbols

Latin letters

a – acceleration amplitude
a_{ci} – centrifugal acceleration
A_p – sheet pile area
c_b – bar velocity
c_d – dilatational wave speed
$\boldsymbol{C}$ – global damping matrix
E_s – Young's modulus for steel
f_d – driving frequency
f_n – natural frequency for mode n
f_y – yield stress
F_c – centrifugal force
F_d – driving capacity
F_l – leader force
F_m – weight of dynamic masses
F_v – unbalanced vertical force
F_0 – static surcharge force
FR – friction ratio from CPT test
g – gravitational acceleration
$\boldsymbol{K}$ – global stiffness matrix
$\boldsymbol{K_e}$ – element stiffness matrix
L – empirical liquefaction factor
L_{min} – smallest element size in the mesh
L_p – sheet pile length
m_c – hydraulic clamp mass
m_{dyn} – dynamic mass of vibrator and sheet pile
m_{eb} – excitor block mass
m_{ei} – eccentric mass
m_{sp} – sheet pile mass
m_v – dynamic vibrator mass
m_0 – bias mass
$\boldsymbol{M}$ – global mass matrix
$\boldsymbol{M_e}$ – element mass matrix
M_e – eccentric moment
p_i – force at the time i
q_d – dynamic toe resistance
q_l – liquefied toe resistance
q_s – static toe resistance
Q_s – shaft quake
Q_t – toe quake
r_{ei} – eccentric radius

R_c – clutch resistance at the clutch between sheet piles
R_s – soil resistance along the shaft of the sheet pile
R_t – soil resistance at the toe of the sheet pile
S_0 – free-hanging displacement amplitude
S_{rsp} – realistic maximum specific displacement amplitude
S_{sp} – maximum specific displacement amplitude
T – crane force
T_n – period time of the highest frequency mode
u_i – displacement at the time i
$\dot{u}_i$ – velocity at the time i
$\ddot{u}_i$ – acceleration at the time i

Greek letters

α – mass-proportional damping constant
α_r – acceleration ratio
β – stiffness-proportional damping constant
Δt – time increment
ζ_n – damping ratio at mode n
θ – rotation angle of eccentric mass
ρ_s – density of steel
τ_d – dynamic shaft resistance
τ_l – liquefied shaft resistance
τ_s – static shaft resistance
ω – angular frequency
ω_n – natural frequency for mode n
Ω_p – sheet pile perimeter

Contents

1 Introduction

This introduction gives a background to the master's dissertation and its purpose, and describes the method used to achieve it. Furthermore, the dissertations limitations and disposition are presented, as well.

1.1 Background

Retaining walls are used to prevent soil instability and ground water leakage during excavation. Steel sheet piles are commonly used to form retaining walls, where the soil stability and water tightness is achieved by forming a wall of interlocked sheet piles. A common way of installing the sheet piles is through vibratory driving, which implies that the sheet piles are driven with a vertical vibratory motion. This method is especially convenient when sheet piles are driven through soft soil. In parts of Sweden, however, the most common type of soil is the glacial till, which generally is very compact and contains a large range of grain sizes, where large grains such as cobbles and boulders are not unusual. Thus, when installing sheet piles in glacial till, there is a risk of impact with stiff objects, which may result in damage to the sheet piles. Experiences in the field have shown that this is a costly and time-consuming issue, where additional measures are needed to ensure stability and water tightness as a result of the damage. Hence, there is a need to detect hazardous situations, and to stop the driving before the sheet pile is severely damaged. Finding a criterion to shut down the driving is of high priority.

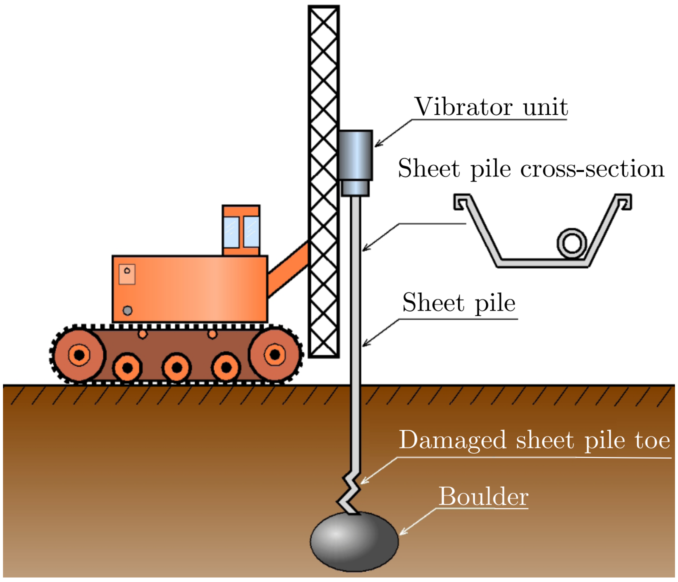

Figure 1.1: Illustration of vibratory driving of a sheet pile. Illustration: Zadig B.

1.2 Purpose and method

The purpose of the master's dissertation is to investigate how numerical models may be used to simulate vibratory driving of a sheet pile, including situations where rigid objects are encountered, and to investigate the possibility of developing a stop criterion based on these numerical simulations.

The method used to fulfil the purpose, was to establish three different numerical models, with decreasing level of complexity, that have the ability to simulate vibratory driving of sheet piles. These models include the behaviour of the sheet pile, the vibratory actions from the vibrator, and the resistance from the surrounding soil.

The first step in creating the models was to research literature for suggestions regarding how the different parts of the system should be modelled, and how the simulations could be carried out. The literature review resulted in a decision that three different models were to be created: a single degree of freedom (SDOF) model, a uniaxial multi degree of freedom (MDOF) model, and a Finite Element (FE) model. It was also decided that explicit time-integration was to be used to run the simulations. All three models were calibrated against an experimental field study of a sheet pile being vibratory driven, to confirm their legitimacy. Thereafter, a rigid obstacle was introduced into the models, to simulate the effects of an impact during vibratory driving. The resulting compressive accelerations from the impacts were then studied, to draw conclusions regarding a potential stop criterion.

The numerical computing platform MATLAB was used to create the SDOF model and uniaxial MDOF model, and the simulations using these models were also carried out in MATLAB. In these two models, the impact with a rigid object was simulated using an elasto-plastic contact force. Further studies of the vibratory parameters were conducted with these models, to gain a better understanding of the dynamics in the vibratory driving process.

The FE model was created and simulated using the software Abaqus. In this model, the impact with a rigid object was simulated by vibratory driving the sheet pile into an introduced solid body with high stiffness, mimicking an impact with a boulder.

1.3 Limitations

Several limitations and simplifications have been introduced in the master's dissertation:

- A specific type of vibrator and a specific type of steel sheet pile was considered. The geometry of the considered sheet pile was simplified.
- Three different impacts were studied, using the FE model. In reality, there is a large number of possible impacts.
- Only the behaviour of a single individual sheet pile was studied, meaning that effects of the sheet pile interlock were neglected.

1.4 Disposition

The disposition of the master's dissertation follows as:

- A literature review on sheet piles, vibratory driving, the occurring mechanical behaviours during vibratory driving and previously used vibro-driveability models are presented in Chapter 2.
- Chapter 3 holds a description of the numerical procedures used in the master's dissertation, as well as some theory regarding dynamic material behaviour.
- A reference case, that is based upon an experimental field study of a vibratory driven sheet pile, is showcased in Chapter 4.
- The parameters of the numerical models established in the dissertation are documented in Chapter 5, and are based upon the reference case.
- Chapter 6 describes the procedures, and the results of a FE model of vibratory driving of a sheet pile, ending with an analysis of the results.
- Chapter 7 describes the procedures, and the results of a uniaxial MDOF model, ending with an analysis of the results.
- Chapter 8 describes the procedures, and the results of a SDOF model, ending with an analysis of the results.
- Chapter 9 gives a general discussion of the dissertation, as well as a comparison of the three established models.
- Finally, concluding remarks, and suggestions for further investigations, are presented in Chapter 10.

2 Vibratory driving of sheet piles

The literature review in this chapter aims to create an understanding of the vibratory driving process, which is needed in order to establish the models in the later part of the dissertation. The chapter starts with a general description of sheet piles in Section 2.1. A description of the general machinery used during vibratory driving is found in Sections 2.2 and 2.3. The mechanical actions that are present during vibratory driving, including soil resistance, are described in Sections 2.4 and 2.5. Finally, in Section 2.6, some methods to predict vibro-driveability are presented.

2.1 Sheet piles and retaining walls

Sheet piles are a category of retaining walls, having as main function to prevent soil instability during construction, and to prevent ground water flow from reaching the excavated area [1].

Individual sheet piles are driven into the soil separately. To achieve a functioning retaining wall, a sequent individual sheet pile is connected to the interlock of the previous sheet pile before being installed. With added sealing, usually concrete, this system can be considered sufficiently waterproof. Because of the interlocks, potential additional friction between the sheet piles can interfere with the installation process [1].

The profile of the sheet pile is designed to lower elastic deflections caused by the soil, and to resist plastic deformation. Common steel sheet pile cross-sections that achieve this are the z-shaped *Hoesch* cross-section, and the u-shaped *Larssen* cross-section, seen in Figure 2.1. The interlocking mechanism between the separate sheet piles can also been seen in the figure.

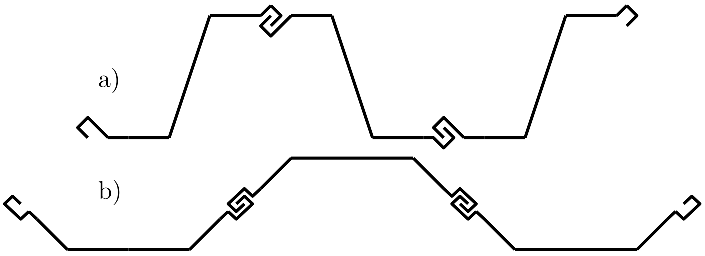

Figure 2.1: Illustrations of common sheet pile cross-sections: a) the z-shaped *Hoesch* profile, and b) the u-shaped *Larssen* profile, modified after Viking [2].

During installation, the sheet piles are driven deeper than the planned excavation level for the ground structure, making the sheet pile wall function as a cantilever. The horizontal soil pressure creates a moment around a rotation point at the excavation level. This moment is being resisted by a reaction moment below the excavated level, and the bending stiffness along the sheet pile's length. An illustration of this can be seen in Figure 2.2. In some situations, this resistance is not enough. Therefore, additional horizontal stability can be contributed to the sheet pile wall by adding either anchor ties, parallel beams, or struts [1].

If the installation of the sheet pile is unsuccessful, and a sufficient penetration depth is not reached, or a failure mode of the sheet pile is conceived, the sheet pile wall may not serve as a functioning retaining wall and may not provide water tightness. Additional resources are then needed to achieve a safe and water-proof construction site. Moreover, if large plastic deformations occurs in the sheet pile, a retraction of it will be difficult. The deformation will cause the sheet pile to be wedged in the surrounding soil and drag a large volume of soil with it when the sheet pile is being retracted. This requires additional time and resources to repair the damages [2].

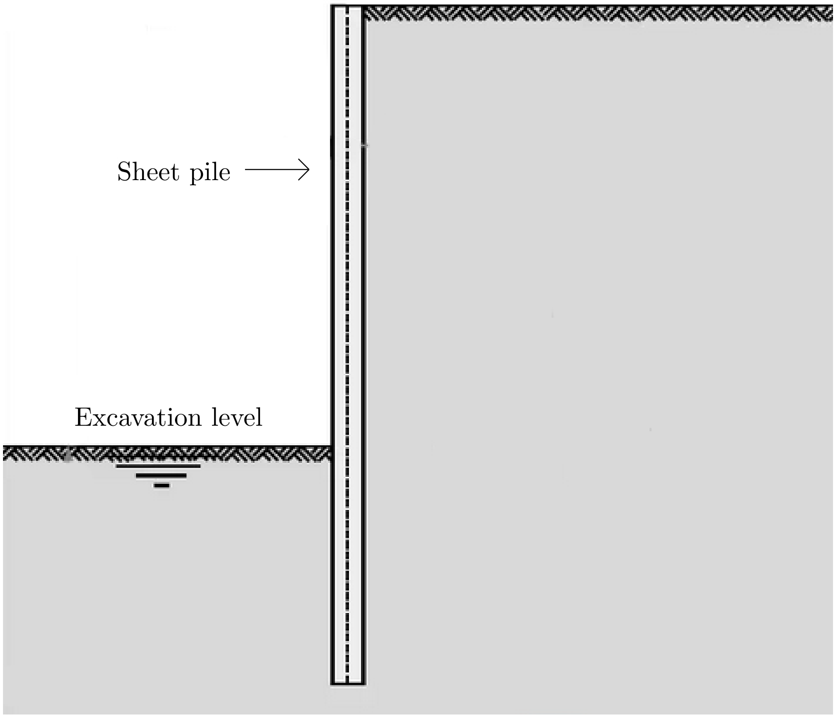

Figure 2.2: Illustration of a sheet pile wall working as a cantilever, modified after ThyssenKrupp [3].

Sheet pile failure modes

Studies regarding failure of sheet piles during vibratory driving are, to our knowledge, none existing. There have, however, been some studies of the failure behaviour of impact driven offshore piles [4] [5]. These conclude a broad range of possible failure modes, and how they are initiated. Some examples of failure modes for offshore piles are: local axial buckling, local non-axial buckling, ovalisation, lateral ring buckling, global buckling, denting damage, yielding, and material failure. All of these are not relevant for vibratory driven sheet piles. Viking and Garcia Benito [6], assumes that the following four failure modes are relevant for steel sheet piles:

- **Local buckling caused by axial loading**
  When the tip of the sheet pile hit an obstacle centrically, axial stresses large enough to cause buckling in the web or flanges may be induced.
- **Local buckling caused by non-axial loading**
  When the tip of the sheet pile hit an obstacle eccentrically, non-axial stresses large enough to cause buckling in the web or flanges may be induced.
- **Extrusion buckling**
  When the sheet pile has buckled or have an initial deformation, and the yield stress of the steel is exceeded, plastic deformation will occur, making the sheet pile unusable.
- **Material fracture**
  If enough plastic deformation occurs, and the fracture stress of the steel is exceeded, the sheet pile will fracture at its tip.

Figure 2.3 shows an example of a sheet pile that has been damaged during driving.

Figure 2.3: Damaged sheet pile, from Viking and Garcia Benito [6]. Photo: Viking K. Example of local axial buckling and material fracture due to round boulder encountered.

2.2 Vibratory driving systems

There are two different general methods of vibratory driving, free-hanging systems, and leader-mounted systems, with the latter being the most frequently used in Sweden. Both systems are described in the following two sections, which are based on Viking [2].

2.2.1 Free-hanging systems

Summarised, a free-hanging system is composed of five major components: a hydraulic power source, a power transmitter, the vibratory driver and a carrying system. These can be seen in Figure 2.4. The hydraulic power source provides the vibratory motors with energy, and hydraulic pressure to the clamps through the power transmitter. The vibrator and its inner components have a massive weight, meaning that a powerful crane often is needed, hence making it a “free-hanging”-system.

Advantages with the free-hanging system are low costs during construction projects, as a crane often is situated at larger construction sites where sheet piles are needed. In addition, the use of a crane gives the system a large reach and mobility.

A disadvantage with the free-hanging system is that it is difficult to position correctly, and to manoeuvre. As the vibratory system is carried by a crane, the possible downward maximum static force is therefore lessened due to the upwards crane force. In addition, there is no ability to provide a larger static surcharge force, if needed.

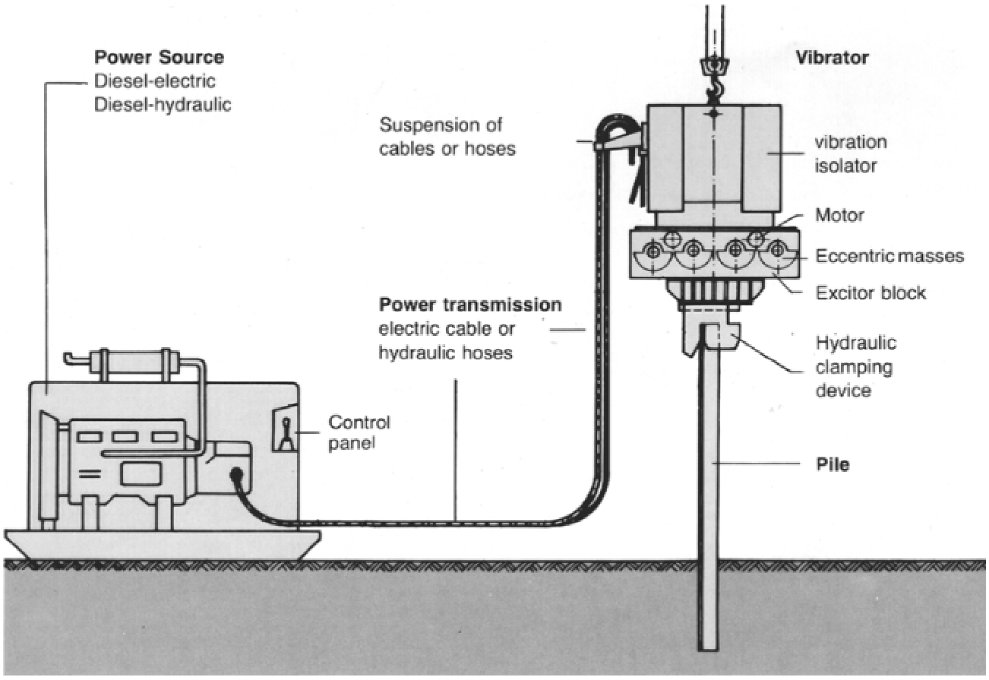

Figure 2.4: Illustration of a typical free-hanging system, with explanatory text, from Viking [2].

2.2.2 Leader-mounted systems

The leader-mounted system, that can be seen in Figure 2.5, basically works the same way as the free-hanging system. The defining difference is that the vibrator unit is carried by a telescopic leader, rather than by a crane. This telescopic leader is often mounted to a regular excavator, where the power supplier and transmitter is mounted as well.

Advantages with the leader-mounted system are a high precision and mobility, provided by the excavator. The ability to vibrate at an angle is also possible. As the vibrator components are mounted to a telescopic leader, the static surcharge force can be both lowered and increased depending on the needs.

Disadvantages with the leader-mounted system are the large cost, and the lack of ability to use the equipment to other things than vibratory driving. The increased weight of the excavator could also result in soil instability around the construction site. The ability to increase the static surcharge force may be a double-edged sword, as too much additional force may result in a structural failure of the sheet pile.

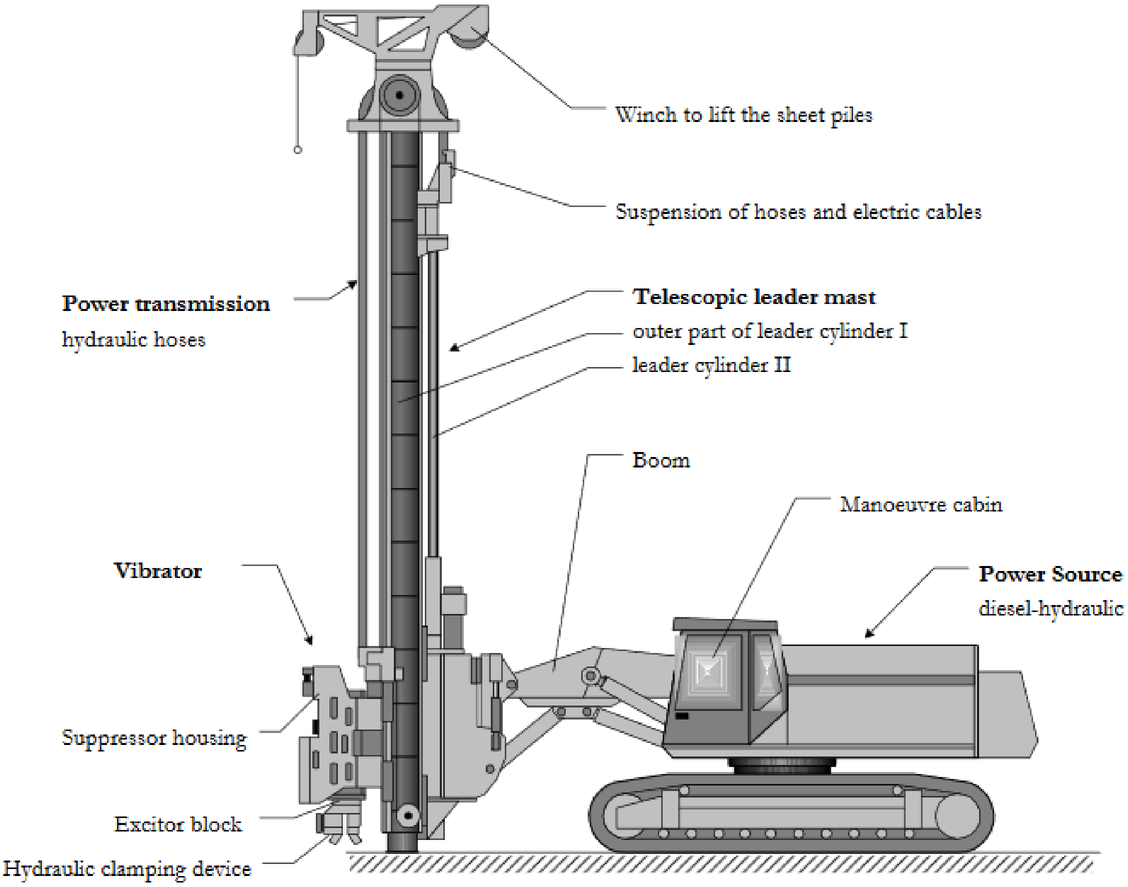

Figure 2.5: Illustration of a typical leader-mounted system, with explanatory text, from Viking [2].

2.3 Vibrator unit

There are many different types of vibrator units from several different manufacturers, but most of them essentially consist of the same components. This section gives a description of the most essential parts of a vibrator unit. This section is largely based on Viking [2].

Most vibrator units on the market today have the same four essential components: a suppressor housing, elastomer pads, an exciter block, and a clamping device. These components can be seen in Figure 2.6.

The suppressor housing holds all components together, while simultaneously being a protective casing around the other more sensitive components. External forces from the system carrying the vibrator, i.e., the crane or the leader, are exerted upon the suppressor housing.

The elastomer pads are steel reinforced rubber pads that are attached in between the suppressor housing and the other components. These pads work as damping isolators, which reduces vibrations in the suppressor housing during vibratory driving. Without them, the carrying crane or excavator could be damaged by the ongoing vibrations. These elastomer pads may have a dampening effect on the whole dynamic structure during vibratory driving.

The excitor block holds eccentrically rotating masses that create a harmonic vertical force. When the vibratory driving is initiated, the eccentric masses are slowly extended from the centre of rotation while rotating at a pre-set frequency, which increases the magnitude of the dynamic vertical force.

The clamping device connects the sheet pile to the vibratory driver. The connection becomes rigid, and the static surcharge- and dynamic forces are transferred into the sheet pile. The clamp can, in addition, be made in all kinds of shapes and sizes to fit the profile being vibratory driven.

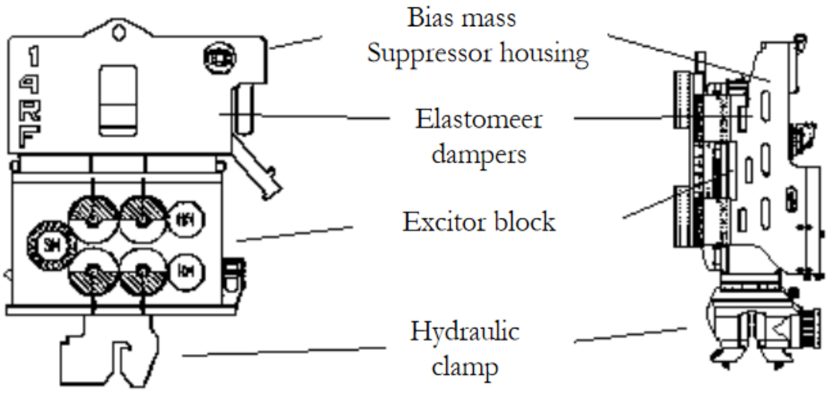

Figure 2.6: Illustration of typical vibratory driver components, from Viking [2]. Free-hanging model to the left, eccentric masses stacked laterally, and leader-mounted model to the right, eccentric masses stacked vertically.

2.4 Mechanics of vibratory driving

Some understanding of the general motion of the sheet pile and the loads that are present during vibratory driving is needed to create accurate models. The free body diagrams in Figure 2.8 provides a visualisation of the forces that are present during the upward and downward motion of the vibratory driving. This section contains a description of the vibrator-related mechanical actions during the vibratory driving process, while Section 2.5 covers the soil-related actions. This section is based on Viking [2] unless something else is stated.

2.4.1 Vibrator forces

The driving capacity F_d is the theoretical driving force that is exerted upon the sheet pile during vibratory driving. It can be expressed as

$$F_d = F_0 + F_v \tag{2.1}$$

where F_0 is the static surcharge force, and F_v is the unbalanced vertical force. The peak theoretical driving force F_d will occur when the unbalanced vertical force reaches its downwards amplitude $\hat{F}_v$. The driving force F_d and its peak magnitude, can be seen in Figure 2.7, where theoretical driving force is plotted versus time.

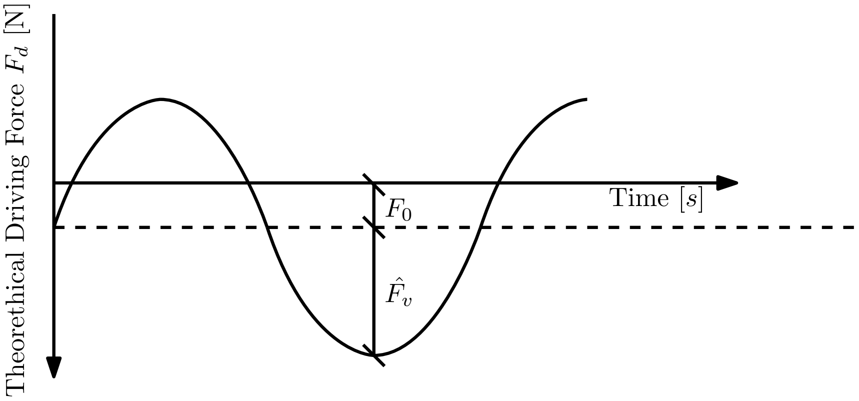

Figure 2.7: Theoretical driving force F_d versus time, modified after Viking [2].

Static surcharge force

Depending on the vibratory method used, the magnitude of the static surcharge force F_0 will differ. For a free-hanging system, the upwards lifting force of the crane T needs to be subtracted from the static surcharge force. For a leader-mounted system, the hydraulic force from the leader F_l, which can be either negative or positive, is added to the static surcharge force. The static surcharge force for a free hanging system and a leader mounted system, respectively, can be expressed as

$$F_0 = m_0 \cdot g - T \tag{2.2}$$

$$F_0 = m_0 \cdot g + F_l \tag{2.3}$$

where m_0 is the suppressor housing mass and g is the gravitational acceleration.

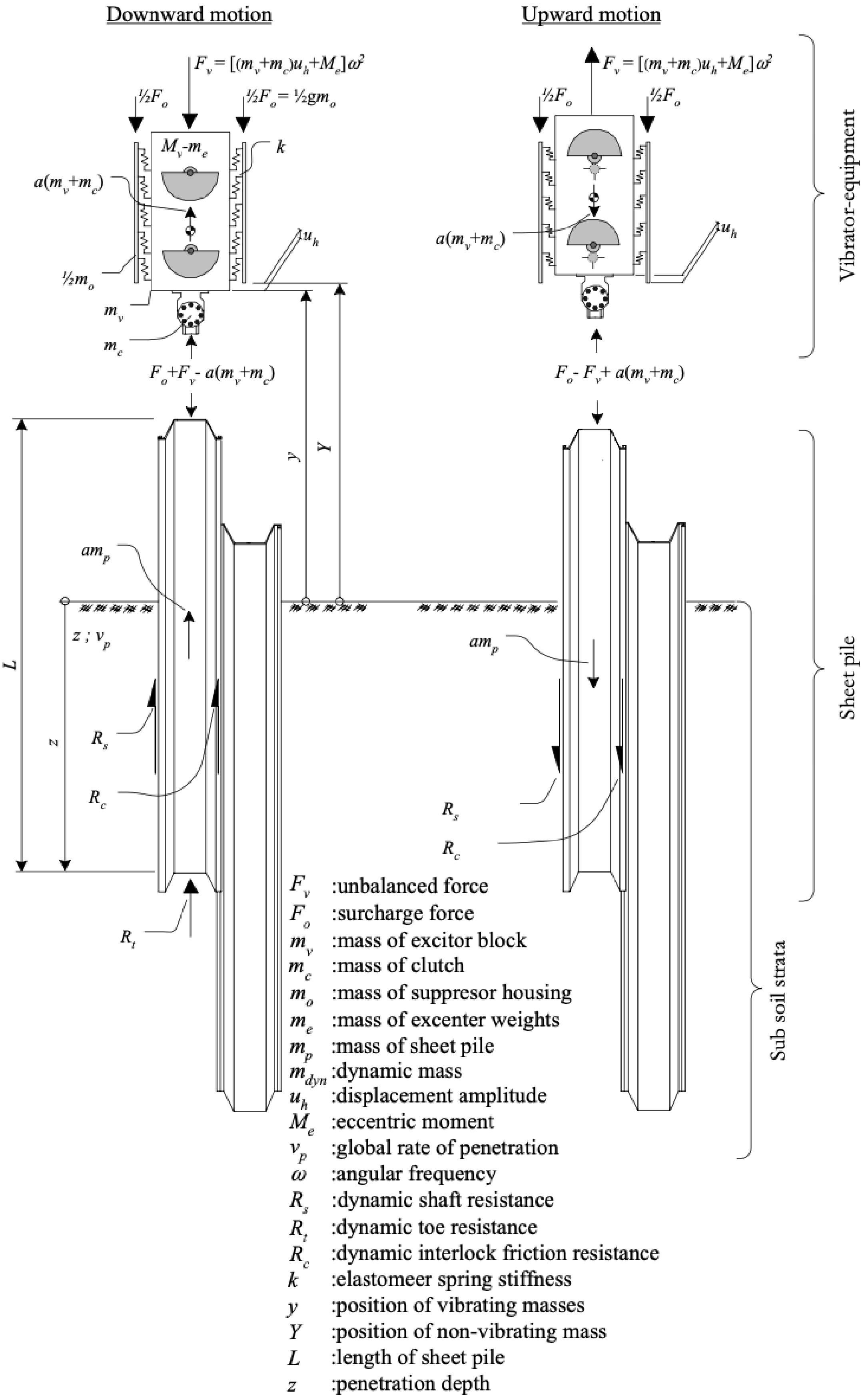

Figure 2.8: Free body diagrams of a sheet pile and vibrator during upward and downward motion, from Viking [2].

Unbalanced vertical force

The unbalanced vertical force F_v is the resultant of the sum of centrifugal forces F_c, generated by the eccentrically rotating masses in the vibrator. When an even number of identical eccentric masses rotate in opposite direction to each other, the horizontal components of the centrifugal forces cancel out. This leaves only the vertical components, which often is referred to as the unbalanced vertical force F_v, calculated as

$$F_v = F_c \cdot \sin\theta \tag{2.4}$$

where θ is the rotation angle of the eccentric mass.

The centrifugal force F_c is affected by two parameters: the eccentric moment M_e, and the angular frequency ω, at which the eccentric masses are rotating. Therefore, the centrifugal force can be expressed as

$$F_c = m_{ei} \cdot a_{ci} = m_{ei} \cdot r_{ei} \cdot \omega^2 = M_e \cdot \omega^2. \tag{2.5}$$

This expression is based on Newton's second law, where the centrifugal acceleration a_{ci} can be expressed with the eccentric radius r_{ei} of the eccentrically rotating masses, and the angular frequency ω, at which the eccentric masses are rotating. The eccentric moment M_e is the product of the eccentric mass m_{ei} and the eccentric radius r_{ei}. Figure 2.9 illustrates the parameters that affect the centrifugal force.

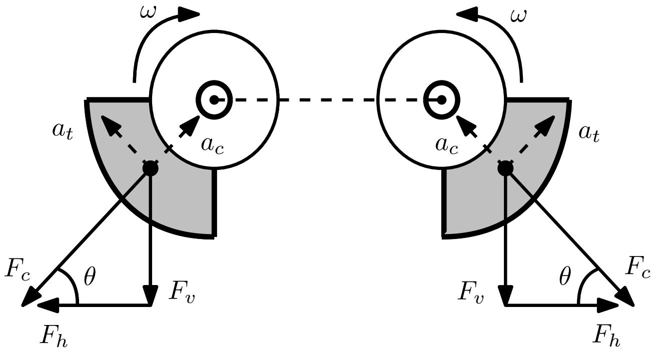

Figure 2.9: Illustration of two eccentric masses rotating in the opposite direction, modified after Viking [2].

2.4.2 Other vibrator related parameters

There are other parameters that likewise affect the dynamic behaviour of the sheet pile. The mass of the sheet pile and the vibrator, with its components, influences the performance of the vibratory driving. The free-hanging displacement amplitude is another parameter that influences the behaviour during vibratory driving. These parameters are described briefly in the following subsections.

Dynamic mass

The dynamic mass m_{dyn} of the structure refers to the inertia of the structure's parts that are moving in the longitudinal direction during vibratory driving, meaning the mass of the excitor block m_{eb}, the hydraulic clamp m_c, and the mass of the steel sheet pile being driven m_{sp}. This can be expressed as

$$m_{dyn} = m_{eb} + m_c + m_{sp}. \tag{2.6}$$

The mass of a structure has an immense contribution to its dynamic behaviour, affecting everything from the structure's displacements to its resonant frequencies.

Free-hanging double displacement amplitude

The free-hanging displacement amplitude S_0 refers to the movement of the vibratory unit without any additional static surcharge force being applied, and without a sheet pile being attached to it. This is a way of characterising a vibratory unit and comparing different vibratory products. The term maximum specific displacement amplitude S_{sp} is sometimes used and is defined as the double of the free-hanging displacement amplitude, as seen in Figure 2.10. These displacement amplitude parameters can be expressed as

$$S_{sp} = 2S_0 = 2\frac{M_e}{m_{eb} + m_c} \tag{2.7}$$

where M_e is the eccentric moment, m_{eb} is the excitor block mass, and m_c is the mass of the hydraulic clamp.

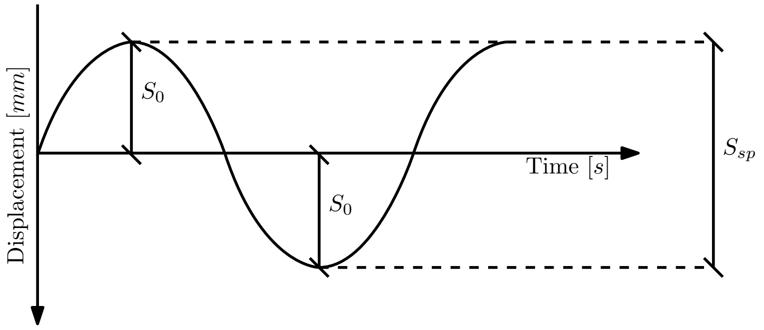

Figure 2.10: Comparison between displacement amplitudes for a free-hanging vibratory system, by Viking [2].

In reality, when driving through soil, the vibratory driving displacements will not be as large as the free-hanging displacements. With the added mass from the sheet pile, and the shaft- and toe resistance from the soil, the displacement amplitudes will be lowered. Therefore, the sheet pile mass m_{sp} may be added to the expression, such as

$$S_{rsp} = \frac{m_{eb} + m_c}{m_{eb} + m_c + m_{sp}} S_{sp} \tag{2.8}$$

to get a more realistic displacement amplitude prediction.

2.5 Soil resistance

The penetrative movement of the sheet pile is resisted by the dynamic soil resistance along the sheet pile shaft and at the sheet pile toe. This section contains a description of the soil resistances and how they can be estimated. Some theory regarding soil liquefaction is also presented.

2.5.1 Soil models

Generally, there seems to be a lack of studies that have attempted to create an accurate material model describing the variation of the shaft resistance and toe resistance during vibratory driving of sheet piles. However, two models were found during the literature review, and these models are presented below. Note that the models presented below do not provide any guidance of how the amplitude values of the dynamic soil resistances should be calculated and that a method to estimate these are presented in Section 2.5.3.

Linear soil models

Moulai-Khatir et al. [7] presented the linear soil models shown in Figure 2.11, where the shaft resistance R_s (force) varies linearly between the maximum shaft resistance $R_{s,max}$ and minimum shaft resistance $-R_{s,max}$. The toe resistance R_t (force) varies linearly between the maximum toe resistance $R_{t,max}$ and 0.

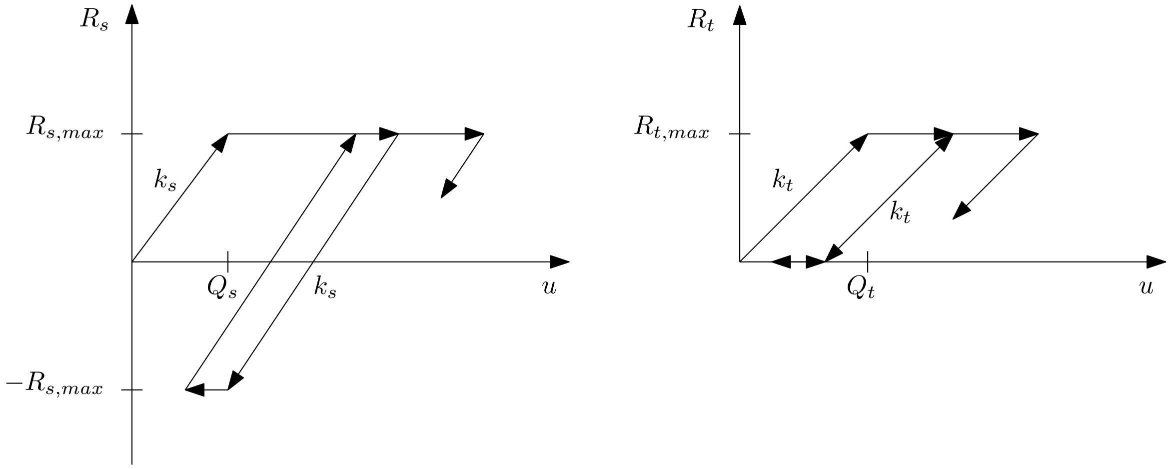

Figure 2.11: Variation of shaft resistance R_s, and toe resistance R_t with the displacement u, modified after Moulai-Khatir et al. [7].

The loading and unloading stiffness for the shaft resistance is determined based on the maximum shaft resistance $R_{s,max}$ and the shaft quake Q_s (maximum elastic soil deformation) as

$$k_s = \frac{R_{s,max}}{Q_s}. \tag{2.9}$$

The loading and unloading stiffness for the toe resistance is determined based on the maximum toe resistance $R_{t,max}$ and toe quake Q_t as

$$k_t = \frac{R_{t,max}}{Q_t}. \tag{2.10}$$

Table 2.1 shows parameters for the linear soil model that, according to Moulai-Khatir et al. [7], were obtained from large scale laboratory tests.

Table 2.1: Parameters for linear soil model, based on Moulai-Khatir et al. [7].

	Pipe pile	H pile
Toe quake, Q_t	3 mm	2.8 mm
Shaft quake, Q_s	2.5 mm	2.5 mm

Hyperbolic soil models

Moulai-Khatir et al. [7] also presented the hyperbolic soil models shown in Figure 2.12 where the shaft resistance τ (stress) varies between the maximum shaft resistance τ_{max} and minimum shaft resistance τ_{min}. The toe resistance q (stress) varies between the maximum toe resistance q_{max} and 0. The formulas describing the loading and unloading curves for the hyperbolic soil models are included in Appendix A.1 together with recommended soil parameters.

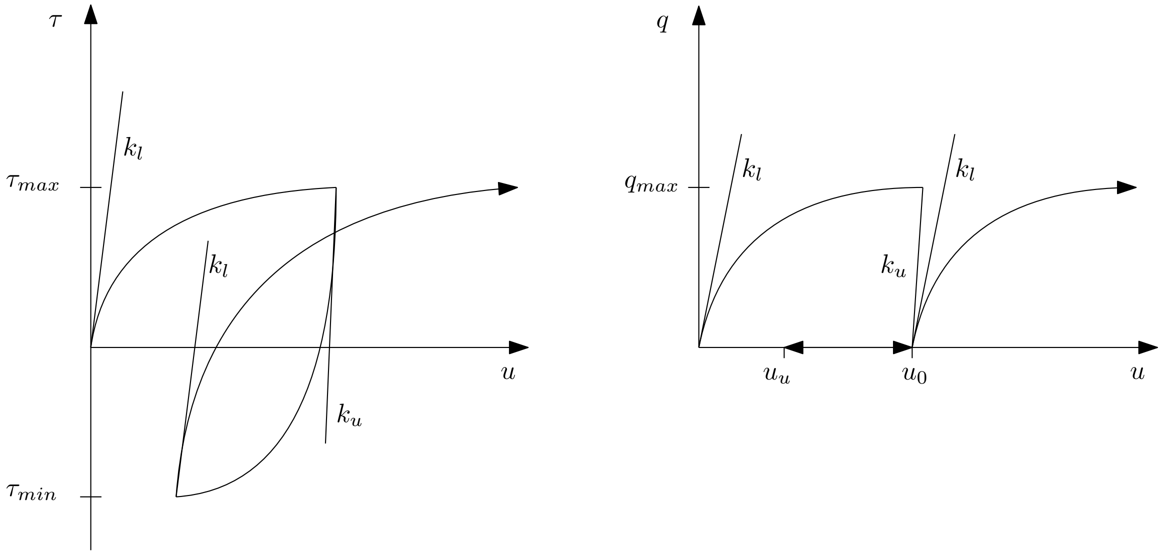

Figure 2.12: Variation of shaft resistance τ, and toe resistance q with the displacement u, modified after Moulai-Khatir et al. [7].

2.5.2 Soil liquefaction

This section contains a description of the phenomenon known as soil liquefaction, the section is based on Viking [2]. Liquefaction is argued to be the main reason why the method of vibratory driving steel sheet piles is the most effective installation method.

During vibratory driving, a reduction in shear-strength occurs in the soil. This occurrence is theorised to partially be a result of the soil mechanical phenomenon liquefaction. When exposed to additional acceleration, e.g., during an earthquake or vibratory driving, the soil grains are moved rapidly towards a new location. Furthermore, while moving, the soil grains are temporarily carried by the internal pore water pressure. This results in all exerted inertial forces having to go through the pore water, and in addition, a lower effective containing stress and effective shear stress. Hence, a reduction of the soil shear-strength will occur.

However, laboratory tests have shown that a reduction in shear-strength also occurs in soils with no moisture. When peak accelerations of the granular soil exceed a threshold of around 1.0–1.5g, the movement of the grains results in the effective vertical confining stress going towards zero in magnitude. As soils are unable to withstand tension, the separation of the soil grains concludes to no compression being able to be sustained either. By exposing a cyclic load, as vibratory driving, to the soil, a constant reduction in the soil shear-strength occurs. This reduction, however, becomes lesser the deeper the sheet pile is driven, as the effective stresses are larger at a deeper penetration depth.

Figure 2.13 illustrates how the shear-strength of the soil is reduced due to liquefaction.

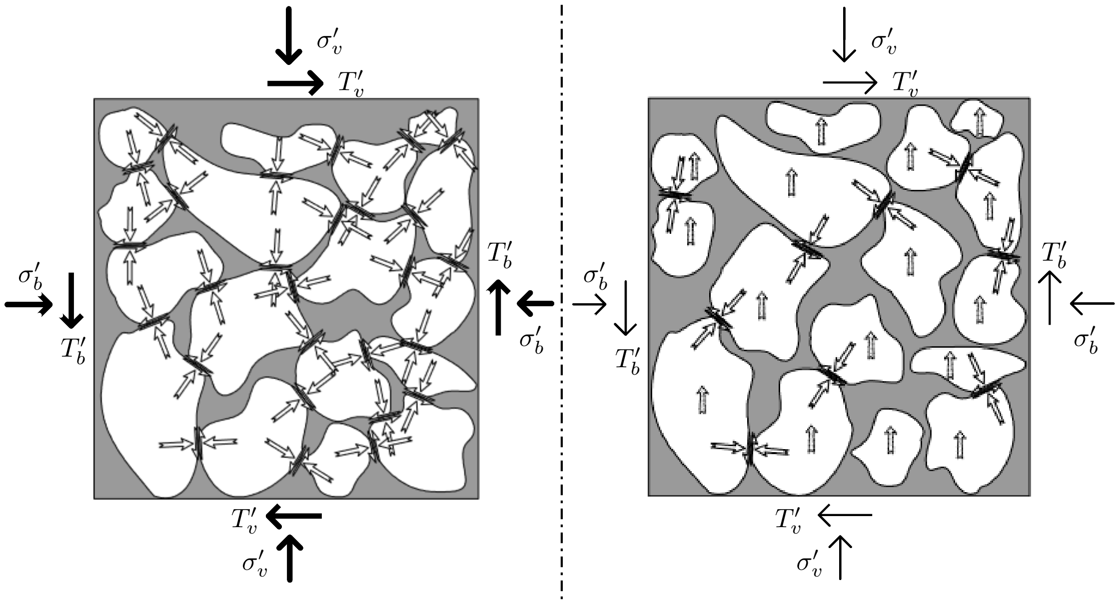

Figure 2.13: Cubically packed assemblage of soil grains affected by effective confining stresses and effective shear stress, which gets reduced when a cyclic inertial force is exerted on the soil. The arrows opposite to each other symbolise inner contact forces, while the stand-alone arrows symbolise inertial forces. Modified after Viking [2].

2.5.3 Amplitude value of dynamic soil resistances

A method to estimate the amplitude values of the dynamic soil resistances $R_{s,max}$ and $R_{t,max}$ (forces) is needed in order to utilise the soil models that were presented in Section 2.5.1.

The method that was used in the dissertation to estimate the amplitude values of the dynamic soil resistances was presented by Van Rompaey et al. [8]. The method consists of four steps that estimates dynamic soil resistances by reducing static soil resistances obtained from cone penetration tests (CPT). Each step of the method is described below.

1. Estimate the acceleration amplitude

The acceleration amplitude a of the sheet pile is estimated based on the dynamic mass m_{dyn}, the vibration frequency ω, and the eccentric moment M_e as

$$a = \frac{M_e \omega^2}{m_{dyn}}. \tag{2.11}$$

The acceleration ratio α_r is then calculated based on the acceleration amplitude as

$$\alpha_r = \frac{a}{g} \tag{2.12}$$

where g is the standard gravity.

The acceleration ratio is later used in step 3 when estimating the dynamic soil resistances, where it is used as a weighting factor. A higher acceleration amplitude results in dynamic soil resistances weighted more towards the liquefied soil resistances while lower acceleration amplitudes results in dynamic soil resistances weighted more toward the static soil resistances.

2. Calculate liquefied shaft resistance and toe resistance

The liquefied soil resistances τ_l and q_l (stresses) are calculated based on the static soil resistances τ_s and q_s (stresses), friction ratio FR and dimensionless empirical liquefaction factor L as

$$\tau_l = \tau_s \cdot \left[(1 - \frac{1}{L}) \cdot e^{-\frac{1}{FR}} + 1/L \right] \tag{2.13}$$

$$q_l = q_s \cdot \left[(1 - \frac{1}{L}) \cdot e^{-\frac{1}{FR}} + 1/L \right] \tag{2.14}$$

where the static soil resistances are determined based on the sleeve friction f_s and tip resistance q_c from CPTs. The friction ratio FR is also determined based on CPTs as $FR = 100 \cdot f_s/q_c$. The dimensionless empirical liquefaction factor L is taken in the range $4 \leq L \leq 10$, where L is assumed higher for saturated and loose sands.

The liquefied soil resistances represents a state where the soil is fully liquefied and where the strength of the soil is reduced considerably.

3. Calculate dynamic shaft resistance and toe resistance

The dynamic soil resistances τ_d and q_d (stresses) are calculated based on the static and liquefied soil resistances and the acceleration ratio as

$$\tau_d = (\tau_s - \tau_l) \cdot e^{-\alpha_r} + \tau_l \tag{2.15}$$

$$q_d = (q_s - q_l) \cdot e^{-\alpha_r} + q_l \tag{2.16}$$

where the acceleration ratio is used a weight function. The above expressions reveal that the dynamic soil resistances are almost completely weighted towards the liquefied soil resistances for acceleration ratios above above 5g.

Finally, the amplitude value of the dynamic shaft resistance $R_{s,max}$ is calculated by integrating the dynamic shaft resistance τ_d over the shaft area of the sheet pile, and the amplitude value of the dynamic toe resistance $R_{t,max}$ is calculated by multiplying the dynamic toe resistance q_d at the sheet pile toe with the area of the sheet pile.

$$R_{s,max} = \Omega_p \int_0^z \tau_d \, dz \tag{2.17}$$

$$R_{t,max} = q_d(z) A_p \tag{2.18}$$

where Ω_p is the perimeter of the sheet pile, A_p is the area of the sheet pile, and z is the depth of the sheet pile toe.

4. Estimate new acceleration amplitude

A new acceleration is calculated, now taking the shaft resistance into consideration, as

$$a = \frac{M_e \omega^2 - \delta R_{s,max}}{m_{dyn}} \tag{2.19}$$

where δ is a dimensionless damping factor. The steps above are then repeated until the acceleration amplitude converges.

2.6 Vibro-driveability models

Some different approaches have previously been used to predict vibro-driveability, i.e., to estimate if and how a sheet pile can be installed through vibratory driving. Holeyman [9] describes four different methods of predicting the vibro-driveability:

- Methods based on force equilibrium.
- Methods based on energy conservation.
- Methods based on momentum conservation.
- Methods based on integration of laws of motion.

These approaches are described briefly in the following sections.

2.6.1 Methods based on force equilibrium

These methods investigates if the vibrator delivers a large enough force to overcome the soil resistance. The general approach is to test if the sum of the driving forces, i.e., the vibrator force, inertia force of the dynamic mass and static surcharge force, is larger than the soil resistance. These methods only compare the magnitudes of the driving forces and resisting forces, and thus do not provide an estimate of the global penetration speed. [9]

2.6.2 Methods based on energy conservation

These methods rely on the assumption that there should be energy equilibrium between the vibrator and the resisting soil. The general approach is to formulate an equilibrium where the power consumed by the soil resistance is set equal to the sum of the power delivered to and generated by the sheet pile-vibrator system. The penetration speed can then be estimated from the power equilibrium. [9]

2.6.3 Methods based on momentum conservation

These methods rely on the assumption that the momentum of the sheet pile–vibrator system for a full cycle is balanced by an impulse of the soil resistance. The general approach is to formulate a momentum equilibrium where the momentum of the total mass of the sheet pile–vibrator system accumulated by gravity during a full cycle is set equal to a soil resistance impulse. The penetration speed can then be estimated from the momentum equilibrium. [9]

2.6.4 Methods based on integration of laws of motion

Methods based on integration of laws of motion predict the penetrative movement of the sheet pile by fulfilling inertial equilibrium at all times, i.e., that there is equilibrium between external forces and inertial forces [9].

Single degree of freedom models

Viking [2] describes a method where the vibrator and sheet pile can be modelled as a single degree of freedom (SDOF) system, by assuming that they behave like a rigid body. Newton's second law can then be used to estimate the acceleration a of the vibrating masses m_{dyn}, and thus, the penetrative motion of the sheet pile can be estimated. The equation of motion for a sheet pile and vibrator modelled as an SDOF system can according to Viking [2] be formulated as

$$F_0 + F_v + F_m - R_s - R_t - R_c = a \cdot m_{dyn} \tag{2.20}$$

where F_0 is the static surcharge force, F_v is the vibrator force, F_m is the weight of the dynamic masses, R_s and R_t are the soil resistances along the shaft and at the toe of the sheet pile and R_c is the clutch resistance.

The rigid body assumption, which the SDOF model relies on, might not be accurate for all situations, Massarsch [10] suggested that the diagram shown in Figure 2.14 can be used to estimate if a pile behaves like a rigid body.

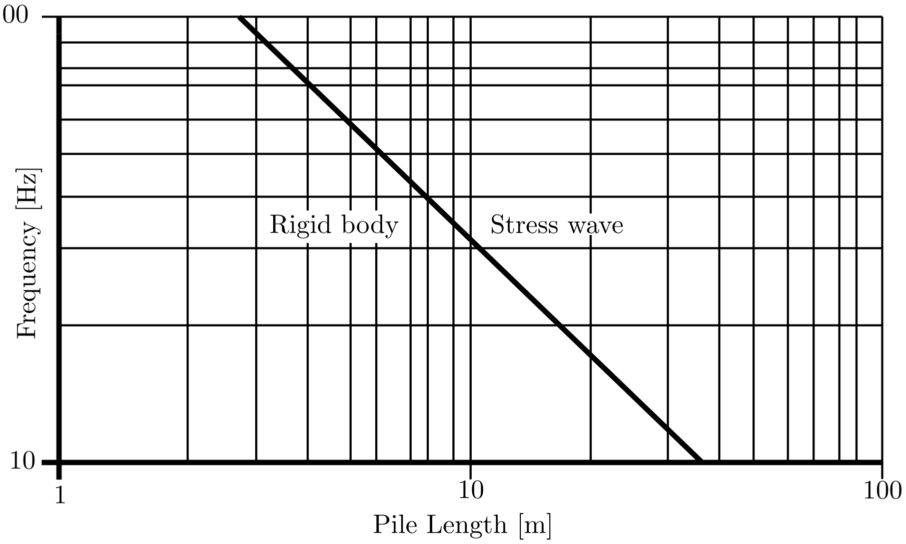

Figure 2.14: Diagram used to determine if a steel pile behaves like a rigid body or not, modified after Massarsch [10].

Viking [2] argues that the rigid body assumption is justifiable as the resonance frequencies of the sheet piles generally are higher than the driving frequency. Viking [2] suggests that the resonance frequency for mode n can be estimated as

$$f_n = n\frac{c_b}{2L} \tag{2.21}$$

where c_b is the bar velocity, and L_p is the sheet pile length. Viking [2] illustrates this with an example where the bar velocity is assumed to $c_b = 5100$ m/s and the sheet pile length is assumed to $L_p = 18$ m, where the result is a first resonance frequency of about 141 Hz which is significantly higher than the usual driving frequencies of around 30–40 Hz.

Longitudinal uniaxial models

According to Holeyman [9], a method to predict the vibro-driveability that has been used previously is to include the longitudinal behaviour of the sheet pile by using a longitudinal uniaxial model. An example of such a model is shown in Figure 2.15, where the vibrator is modelled as two masses separated by a spring, and where one of the masses is subjected to a sinusoidal force representing the rotating masses. The sheet pile is modelled as masses and springs, and the soil resistances are modelled using springs, sliders and dashpots.

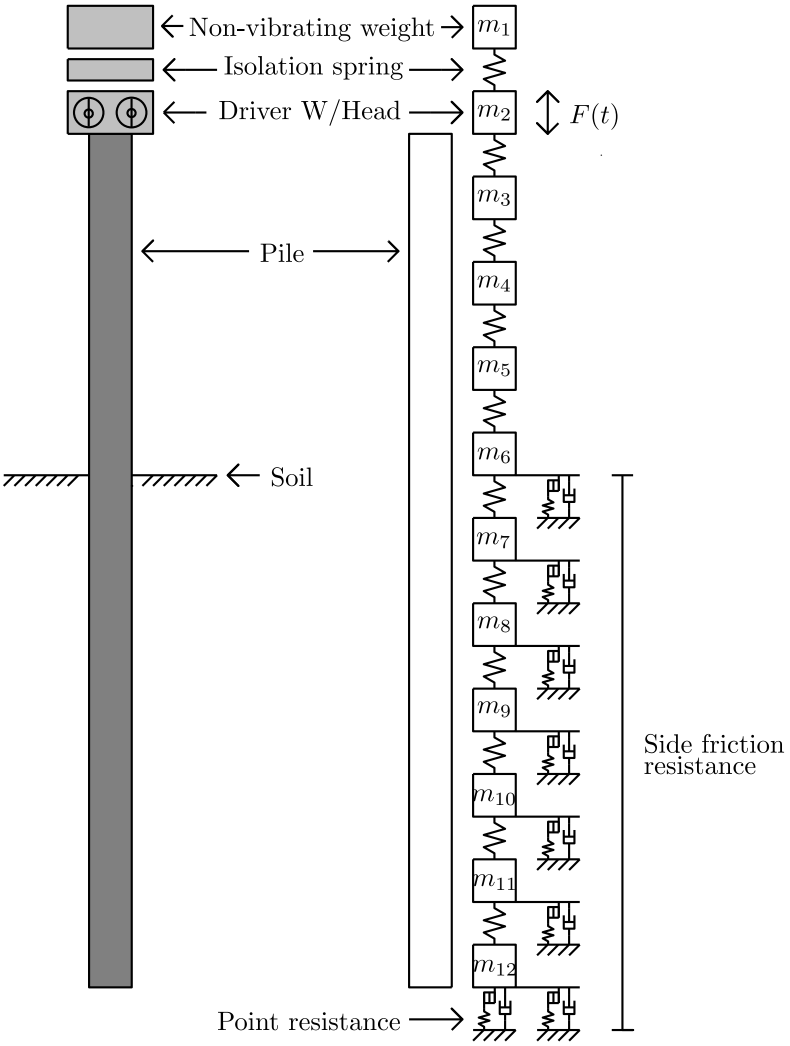

Figure 2.15: Illustration of a longitudinal uniaxial model of vibrator, sheet pile and soil, modified after Holeyman [9].

3 Numerical procedures

This chapter aims to describe the numerical procedures that were used when simulating the vibratory driving. Section 3.1 describes the time-stepping method known as the Central Difference Method. Section 3.2 provides a description of the commercial FE analysis software Abaqus explicit. A brief introduction to the Finite Element Method (FEM) is provided in Section 3.3. Finally, a short description of Rayleigh damping is presented in Appendix A.3.

3.1 Central Difference Method

Dynamic processes can be analysed using explicit numerical time-stepping. Explicit methods refer to numerical methods were the solution at time $i+1$ is determined exclusively from an equilibrium derived at time i. The Central Difference Method is an example of an explicit time-stepping method which is rather simple, while also being efficient in handling non-linear dynamic problems. This section contains a brief description of the Central Difference Method, which is based on Chopra [11], where further information about the Central Difference theorem can be found.

In the Central Difference Method, the velocity $\dot{u}_i$ and acceleration $\ddot{u}_i$ at time i is expressed as

$$\dot{u}_i = \frac{u_{i+1} - u_{i-1}}{2\Delta t} \tag{3.1}$$

and

$$\ddot{u}_i = \frac{\frac{u_{i+1}-u_i}{\Delta t} - \frac{u_i - u_{i-1}}{\Delta t}}{\Delta t} \tag{3.2}$$

where u_i is the displacement of the section at the time i, and Δt is the time step length, which is constant for all time steps. The velocity and acceleration are then inserted into the equation of motion

$$m\ddot{u} + c\dot{u} + f_s = p, \tag{3.3}$$

and rearranged to solve for the next displacement u_{i+1}. In the dissertation the sheet pile is modelled linearly while the soil resistance is modelled non-linearly. Thus, the expression for the next displacement for the sheet pile can be written as

$$\left[\frac{m}{(\Delta t)^2} + \frac{c}{2\Delta t}\right] u_{i+1} = p_i - \left[\frac{m}{(\Delta t)^2} - \frac{c}{2\Delta t}\right] u_{i-1} + \frac{2m}{(\Delta t)^2} u_i - (f_s)_i \tag{3.4}$$

where p_i is external forces from the vibrator, m is the mass of the sheet pile and vibrator and c is the damping of the sheet pile. The non-linear internal forces from the soil resistances and the linear internal forces in the sheet pile are represented by $(f_s)_i$.

For the iteration of Equation (3.4) to function, the initial displacement u_0, and initial velocity $\dot{u}_0$ is required to be known. Thereafter, the initial acceleration $\ddot{u}_0$ can be computed by solving the equation of motion. With these known, the remaining time increments of the dynamic process can be iterated. The iteration process is visualised in Figure 3.1, where the velocity $\dot{u}_i$ is defined as the difference in displacement over the previous and preceding time increment, while the acceleration $\ddot{u}_i$ is defined as the difference in mid-interval velocity. The mid-interval velocities are represented by the filled in circles in Figure 3.1.

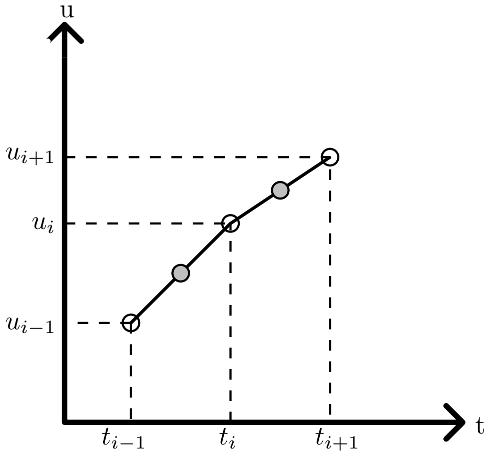

Figure 3.1: Illustration of the methodology of the Central Difference Method.

The stability requirement of the Central Difference Method is expressed as

$$\frac{\Delta t}{T_n} < \frac{1}{\pi} \tag{3.5}$$

where T_n is the period time of the highest natural frequency. The stability of the method refers to the lack of growing numerical round-off errors that occur during the iterations. Too large time increments will, therefore, result in inaccurate results. When the size of the time increments goes towards infinitesimal, the numerical result will go towards a converged solution.

Iteration schemes for the Central Difference Method for non-linear SDOF and MDOF systems are shown in Tables 3.1 and 3.2.

Table 3.1: Central Difference Method for SDOF systems, after Chopra [11].

- Initial calculations
  - $\ddot{u}_0 = \dfrac{p_0 - c\dot{u}_0 - (f_s)_0}{m}$
  - $u_{-1} = u_0 - \Delta t \dot{u}_0 + \dfrac{(\Delta t)^2}{2}\ddot{u}_0$
  - $\hat{k} = \dfrac{m}{(\Delta t)^2} + \dfrac{c}{2\Delta t}$
- Calculations for time step i
  - $\hat{p}_i = p_i - \left[\dfrac{m}{(\Delta t)^2} - \dfrac{c}{2\Delta t}\right] u_{i-1} + \dfrac{2m}{(\Delta t)^2} u_i - (f_s)_i$
  - $u_{i+1} = \dfrac{\hat{p}_i}{\hat{k}}$
  - $\dot{u}_i = \dfrac{u_{i+1} - u_{i-1}}{2\Delta t}$
  - $\ddot{u}_i = \dfrac{u_{i+1} - 2u_i + u_{i-1}}{(\Delta t)^2}$

Table 3.2: Central Difference Method for MDOF systems, after Chopra [11].

- Initial calculations
  - Solve : $\boldsymbol{M}\ddot{\boldsymbol{u}}_0 = \boldsymbol{p}_0 - \boldsymbol{C}\dot{\boldsymbol{u}}_0 - (\boldsymbol{f}_s)_0$
  - $\boldsymbol{u}_{-1} = \boldsymbol{u}_0 - \Delta t \dot{\boldsymbol{u}}_0 + \dfrac{(\Delta t)^2}{2}\ddot{\boldsymbol{u}}_0$
  - $\hat{\boldsymbol{k}} = \dfrac{\boldsymbol{M}}{(\Delta t)^2} + \dfrac{\boldsymbol{C}}{2\Delta t}$
  - $\boldsymbol{a} = \dfrac{\boldsymbol{M}}{(\Delta t)^2} - \dfrac{\boldsymbol{C}}{2\Delta t}$
  - $\boldsymbol{b} = -\dfrac{2\boldsymbol{M}}{(\Delta t)^2}$
- Calculations for time step i
  - $\hat{\boldsymbol{p}}_i = \boldsymbol{p}_i - \boldsymbol{a}\boldsymbol{u}_{i-1} - \boldsymbol{b}\boldsymbol{u}_i - (\boldsymbol{f}_s)_i$
  - Solve : $\hat{\boldsymbol{k}}\boldsymbol{u}_{i+1} = \hat{\boldsymbol{p}}_i$
  - $\dot{\boldsymbol{u}}_i = \dfrac{\boldsymbol{u}_{i+1} - \boldsymbol{u}_{i-1}}{2\Delta t}$
  - $\ddot{\boldsymbol{u}}_i = \dfrac{\boldsymbol{u}_{i+1} - 2\boldsymbol{u}_i + \boldsymbol{u}_{i-1}}{(\Delta t)^2}$

3.2 Abaqus Explicit

Abaqus Explicit is a commercial Finite Element analysis software that uses the Central Difference Method (see Section 3.1) to solve dynamic problems through time stepping. This section contains a general description of Abaqus Explicit, based on [12].

Firstly, for the explicit analysis to work, every active degree of freedom must have an inertia. The element masses must, in addition, be lumped in the mass-matrix. Other than that, the same previous prerequisites for the Central Difference Method are the same.

In Abaqus, the stability requirement of the Central Difference Method is based on either the model's smallest element sizes, or the highest frequency affecting the whole model. If Abaqus deems the globally highest affecting frequency to give a too large stability time increment size, the program opts for the conservative method of element-by-element estimation. Hence, for a general shell-model, the required time increment size for stability is approximated by the defined transverse shear stiffness of the shell-elements in the mid-plane. An approximate required time increment size can be expressed as

$$\Delta t \approx \frac{L_{min}}{c_d} \tag{3.6}$$

where L_{min} is the smallest element size in the mesh, and c_d is the dilatational wave speed of the element. In general, Abaqus will, for a three-dimensional model, chose a stability requirement that is 1 to $1/\sqrt{3}$ times lesser than this estimate. If the stability requirement is not met, results of the model will oscillate, and the total energy balance in the system will change drastically. Another criteria for Abaqus to choose the conservative stability requirement over the global one, is if one of the following example capabilities are included in the model: too thick shells, dashpots or material damping.

In explicit dynamic analyses, in Abaqus, linear bulk viscosity is automatically added. It generates a bulk viscosity pressure that is linear in the volumetric strain rate, which is based upon the dilatational mode of each element. The dampening effect that follows is not intended as a material or structural damping, but rather as a numerical damping that lessens the contribution from high frequencies.

The explicit analysis can use small time increment sizes without iterations and tangent stiffness matrices to be formed, while the solution still is proceeding. The explicit analysis also facilitates models where impact occurs, as impacts happen during short periods of time. The small time increments of the explicit integration can therefore capture the resulting behaviour, making it ideal for the dynamic impact simulations required in the dissertation. The alternative would be implicit integration, where the stability is unconditional, and its time increments are based upon dynamic equilibrium. A comparison would conclude that explicit integration is to prefer for analyses that require large computational cost, that occur during small periods of time, and where stress wave propagation is of relevance.

3.3 Finite Element Method

This section contains a brief description of the Finite Element Method. For a more in-depth explanation of the required procedures, and set-up, of the Finite Element Method, see for example Ottosen and Petersson [13].

The Finite Element Method is a numerical method of approximating solutions for differential equations that describe physical problems. The solutions for the differential equations are acquired by dividing the studied body into smaller parts (finite elements) and approximating a solution for each element [13]. The method is visualised in Figure 3.2.

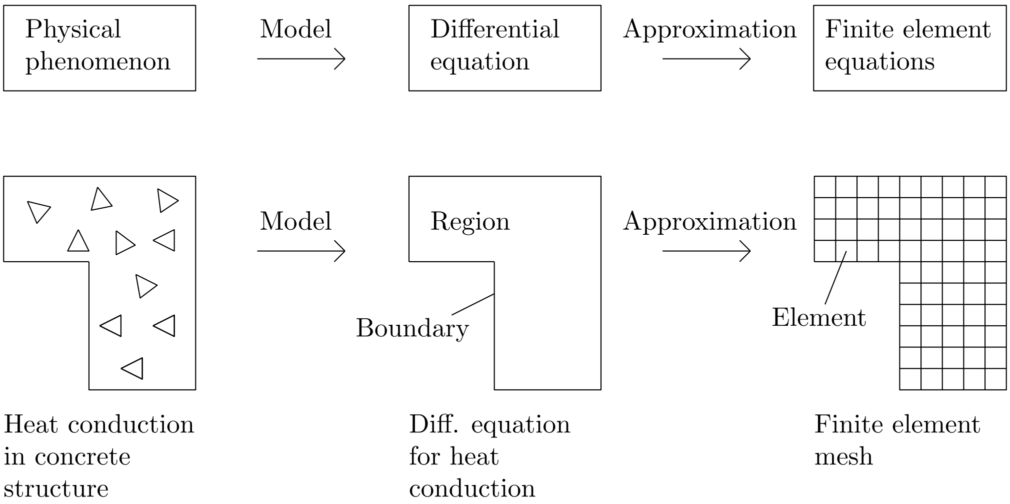

Figure 3.2: Visualisation of the Finite Element Method, modified after Ottosen and Petersson [13].

The general Finite Element formulation of the equation of motion can be expressed as

$$\boldsymbol{M}\ddot{\boldsymbol{u}} + \int_V \boldsymbol{B}^T \boldsymbol{\sigma} dV = \boldsymbol{f} \tag{3.7}$$

where $\boldsymbol{\sigma}$ can define any inner constitutive relation, while $\boldsymbol{f}$ is the external forces exerted upon the structure. The Finite element formulation of the mass matrix $\boldsymbol{M}$ of the structure is defined as

$$\boldsymbol{M} = \int_V \rho \boldsymbol{N}^{\boldsymbol{T}} \boldsymbol{N} \, dV \tag{3.8}$$

where the density ρ is integrated over the volume V of the structure, while $\boldsymbol{N}$ is the form function matrix. The internal, and external forces may be determined in numerous ways.

As the Finite element method is an approximate solution, the smaller the element size used is, the more correct the solution becomes. When the element sizes go towards infinitesimal, the solution converges towards the exact solution [13].

4 Reference case

A field study of vibratory driving of steel sheet piles that was conducted by Viking [2] was used as a reference case. The purpose of using a reference case was to base the models on realistic soil properties and to facilitate comparison between numerical results (from the master's dissertation) and experimental results (from the field study by Viking [2]), resulting in the possibility to calibrate the models in the master's dissertation. This chapter gives a brief description of the reference case, starting with the prerequisites of the field study and ending with the results of the field study as well as some comments on the results.

4.1 Field study

The field study, by Viking [2], was performed in Vårby, outside of Stockholm, and included vibratory driving of various sheet pile cross-sections, vibratory driving with and without clutch friction, and with and without attached sensors. Furthermore, cone penetration tests (CPT) were performed during the field study. CPT is an in-situ method used to determine, for example, soil strata and soil properties. The method consist of pressing steel cones, see Figure 4.1, into the ground while measuring quantities as tip resistances q_c and sleeve friction f_c, which is the soil resistance (stress) at the tip of the cone and along the sleeve of the cone, respectively. For more in-depth information about CPT, see Larsson [14]. The following sections contain a brief description of the prerequisites for the field test and CPTs, based on Viking [2].

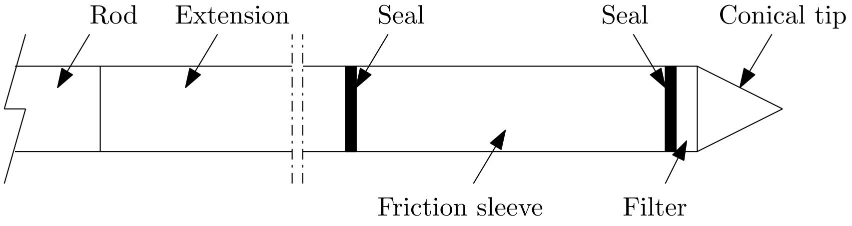

Figure 4.1: Geometry and components of a CPT probe, modified after Larsson [14].

.

4.1.1 Soil conditions

The soil at the test site consisted of 1.5–2.0 m of topsoil and clay on top of over 40 m of glacial sand, varying between silty sand and gravelly sand. The soil conditions and soil properties at the test site were estimated by Viking [2] based on CPT and soil samples. These showed that the soil mainly consisted of variations of sand, with a soil friction angle around 30° and a shear modulus between 50–90 MPa. Results from one of the cone penetration tests conducted at the test site are shown in Figure 4.2, where the variation of the tip resistance q_c and sleeve friction f_c are shown.

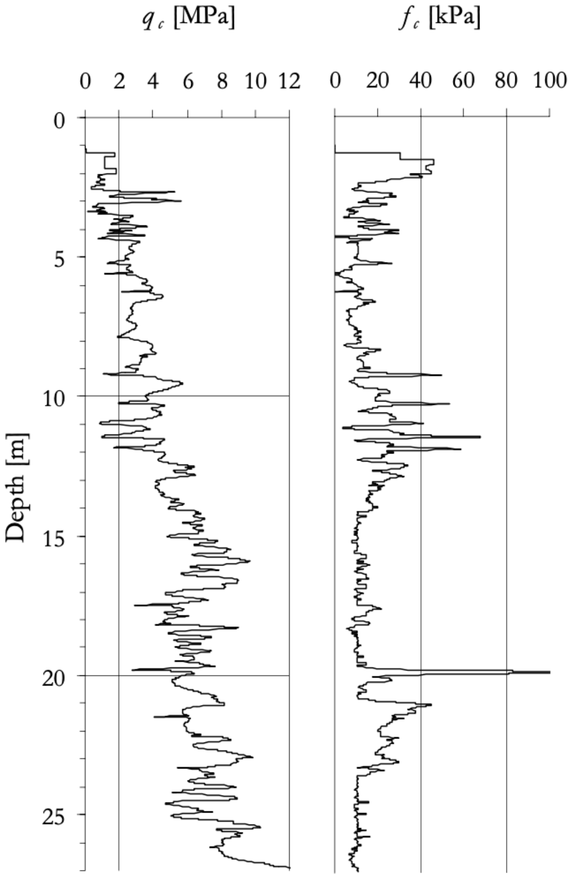

Figure 4.2: Results from the CPT test conducted at the test site, from Viking [2], where q_c is the tip resistance, and f_c is the sleeve friction.

4.1.2 Vibrator

A leader mounted vibrator from ABI (MRZV 800V) was used during the field test. The properties of the vibrator are shown in Table 4.1.

Table 4.1: Vibrator properties, modified after Viking [2].

Parameter	Value	Unit
Maximum frequency	41	Hz
Eccentric moment	0–12	kgm
Maximum driving force	800	kN
Dynamic mass of vibrator unit	2,450	kg
Maximum pile weight	2,000	kg
Maximum driving force, leader cylinder	70	kN
Maximum driving force, support cylinder	90	kN
Maximum extraction force, leader cylinder	140	kN
Maximum extraction force, support cylinder	175	kN

Vibrator settings

The driving frequency was, according to Viking [2], set to 41 Hz during the field test. No information was found (by the authors of the master's dissertation) regarding the exact setting of the eccentric moment, but Viking [2] assumed the eccentric moment to 6 kgm when evaluating the results of the field study.

4.1.3 Sheet piles

Two types of sheet piles were installed during the field study: LX-16 profiles and PU-16 profiles, however only the PU-16 profiles were equipped with sensors. The section properties for the PU-16 sheet pile are shown in Table 4.2, and Figure 4.3. The length of the sheet piles was 14 m.

Table 4.2: Sheet pile PU-16 section properties, after Viking [2].

Parameter	Value	Unit
Mass per meter	74.7	kg/m
Cross-section area, A	95.2	cm^2
Perimeter, Ω	2,018	mm
Section modulus, W_x	1,600	cm^3
Moment of inertia, I_x	5,560	cm^4

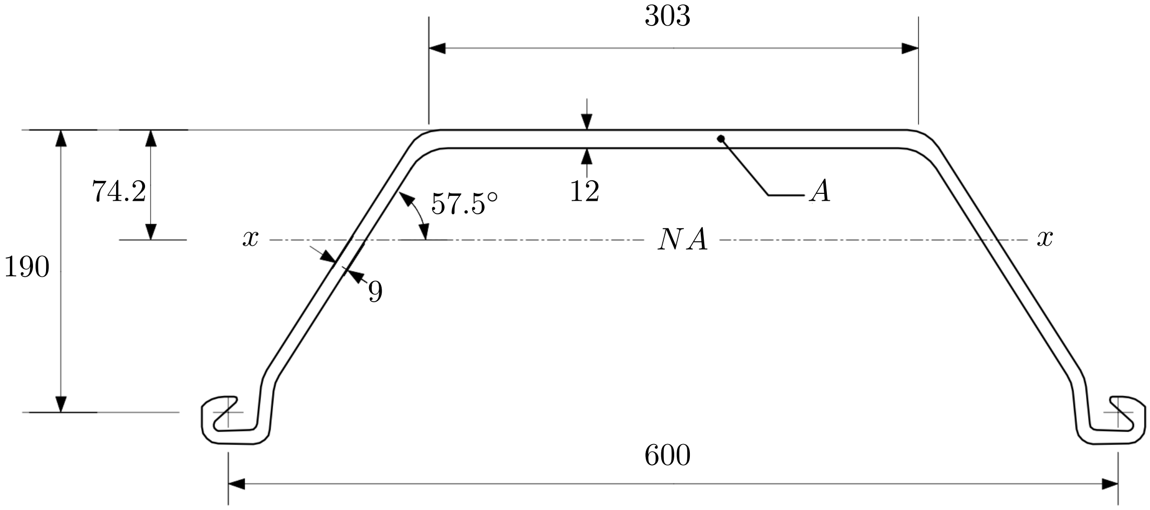

Figure 4.3: Illustration of sheet pile PU-16's cross section with dimensions in millimetres, modified after Viking [2]. NA indicates the neutral axis in the x-direction.

4.2 Field study results

In this section, results from the field study by Viking [2] are shown. The results are from the installation of sheet pile A4, which was of the type PU-16. Sheet pile A4 was chosen as it was installed without clutch friction, and because there was plenty of measurements available. Some brief comments on the results are also presented.

Figure 4.4 shows the vibro-driveability of the sheet pile presented as penetration depth versus driving time, and global penetration speed versus penetration depth.

Figure 4.4 suggests that the vertical penetration speed was to be kept at a rather constant level, at around 120–130 mm/s. To achieve this, the magnitude of the exerted surcharge force would probably need to be varied depending on the penetration depth. At a deeper penetration depth, the total soil resistance is larger than at shallower penetration depths. Therefore, the surcharge force must restrain the sheet pile at shallower depths, whilst pushing the sheet pile and providing additional driving capacity at deeper depths. A dip in the penetration speed can be seen around 0–2 m, in Figure 4.4, where the penetration speed goes down to around 80 mm/s before reaching a more or less constant level between 4–11 m. A possible explanation for this, with the assumption that the penetration speed should be kept constant, might be that it took some time to find the correct loading rate.

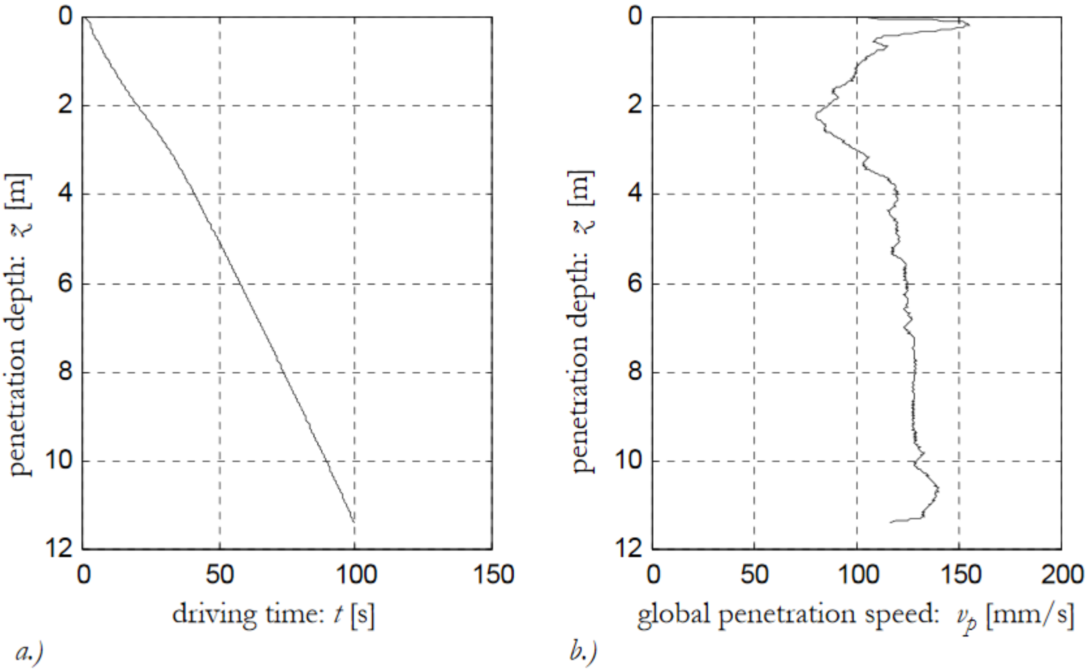

Figure 4.4: Vibro-driveability of sheet pile A4, presented as penetration depth versus (a) driving time and (b) global penetration speed, from Viking [2].

Figure 4.5 shows the peak lateral acceleration and peak vertical toe acceleration versus penetration depth. Figure 4.5 shows that the peak vertical acceleration of the sheet pile is rather constant regardless of the penetration depth, with magnitudes of approximately 15–18g during the study.

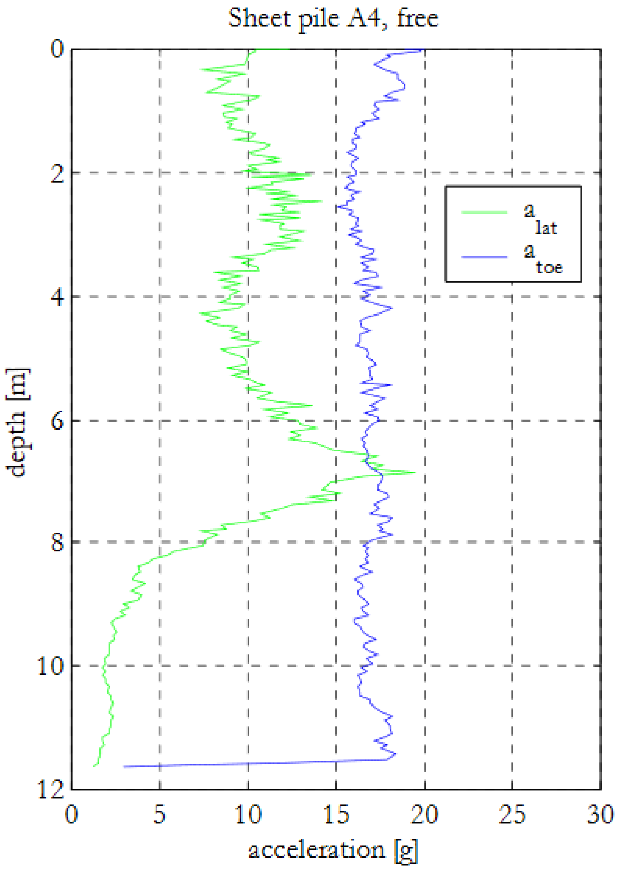

Figure 4.5: Peak acceleration amplitude versus penetration depth of sheet pile A4, from Viking [2].

Figure 4.6 shows the vertical and lateral acceleration of the sheet pile toe versus time, for penetration depths of two, six and ten metres. Positive acceleration indicate downwards motion, while negative acceleration indicate upwards motion.

Figure 4.6 shows that at two metre penetration depth, the acceleration varies between about 11g in the downward direction and 15g in the upward direction. At a six metre penetration depth, the acceleration varies between about 12g in the downward direction and 18g in the upward direction. At a ten metre penetration depth, the acceleration varies between about 12g in the downward direction and 15g in the upward direction.

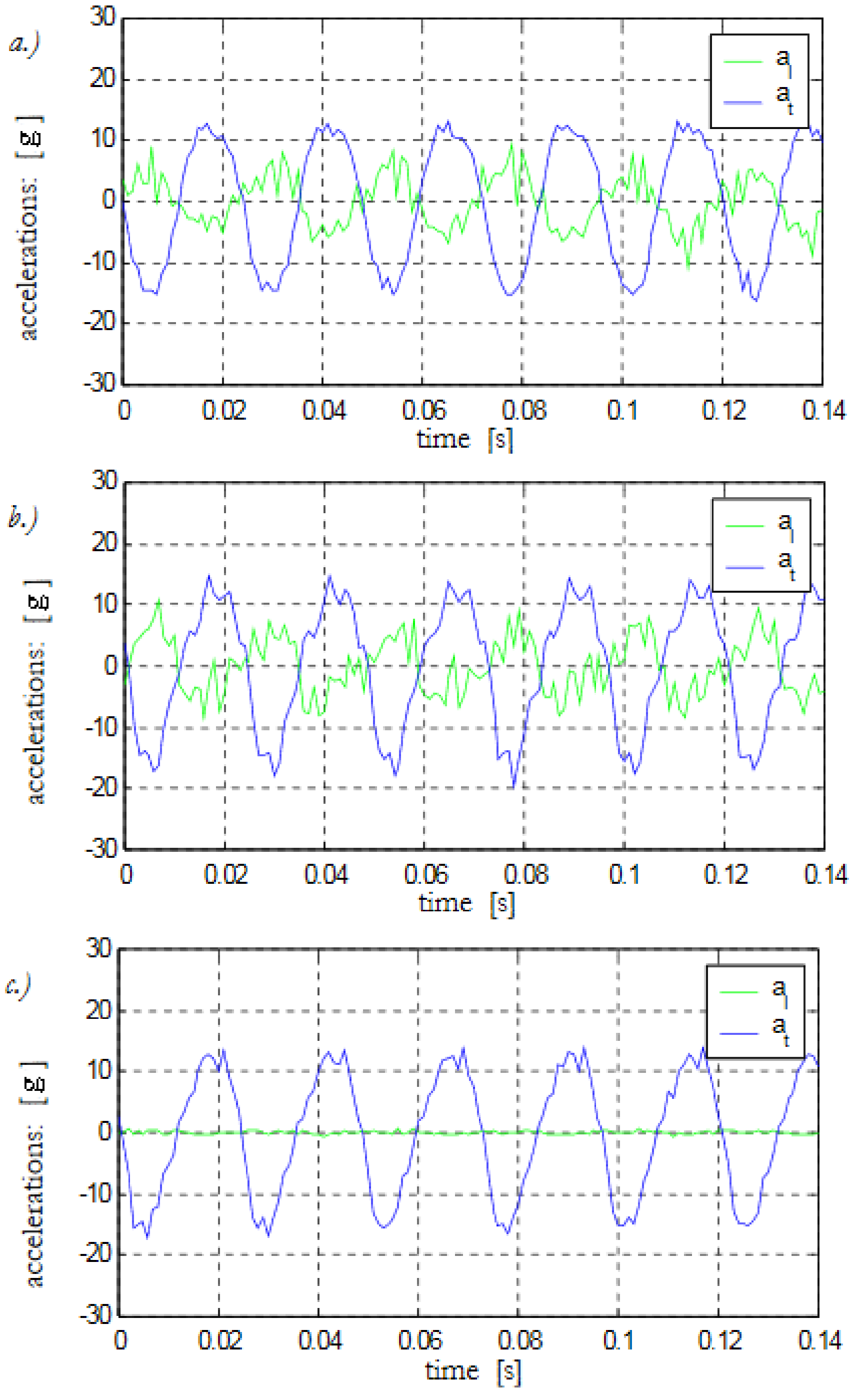

Figure 4.6: Acceleration of sheet pile A4 versus time, corresponding to penetration depths of (a) 2.0 (b) 6.0 and (c) 10.0 m, modified after Viking [2].

Figure 4.7 shows the displacement of the sheet pile versus time, for penetration depths of two, six and ten metres.

The downward displacement of the sheet pile during each cycle is about 5 mm, regardless of the penetration depth, as seen in Figure 4.7. The upward displacement of the sheet pile during each cycle is about 2.5 mm at six and ten metres penetration depth while it is slightly larger, about 3 mm, at two metres penetration depth. This could probably explain why the penetration speed is lower at two metres penetration depth, than at a six and ten metres penetration depth, as previously seen in Figure 4.4.

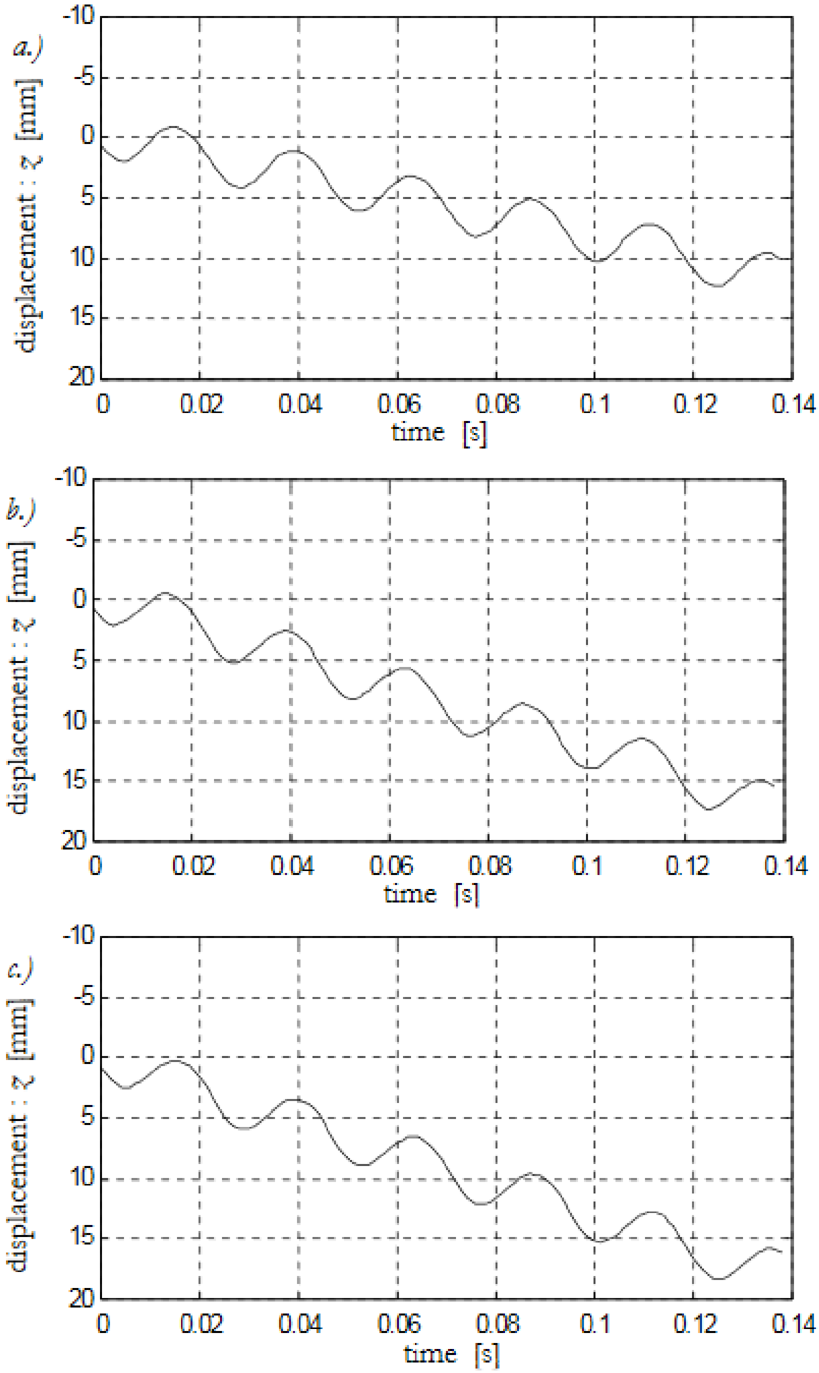

Figure 4.7: Displacement of sheet pile A4 versus time, corresponding to penetration depths of (a) 2.0 (b) 6.0 and (c) 10.0 m, from Viking [2].

5 Model parameters

In this chapter, the model parameters, that all three models have in common, are described. The same soil conditions, the same type of sheet pile and the same type of vibrator was assumed in all models. Section 5.1 provides a description of the assumed soil profile while dynamic soil resistances are derived from the assumed soil profile in Section 5.2. Section 5.3 presents the assumed soil model. Finally, Sections 5.4 and 5.5 provide descriptions of the assumed vibrator and sheet pile.

5.1 Soil profile

The soil profile in the models was assumed to be the same as the soil profile in the reference case, i.e., a couple of metres of topsoil and clay on top of a very thick layer of glacial sand. However, the ground level in the dissertation (0 m depth) was assumed to be at the level corresponding to 1 m below the ground in the reference case, as the first CPT data was from this level. Simplified profiles of the tip resistance q_c and skin friction f_c were created based on the CPT results in Figure 4.2, by estimating a linear stress variation for each metre of penetration depth. The simplified profiles are shown in Figure 5.1, where also the friction ratio FR is shown, estimated as $FR = 100 \cdot f_c/q_c$.

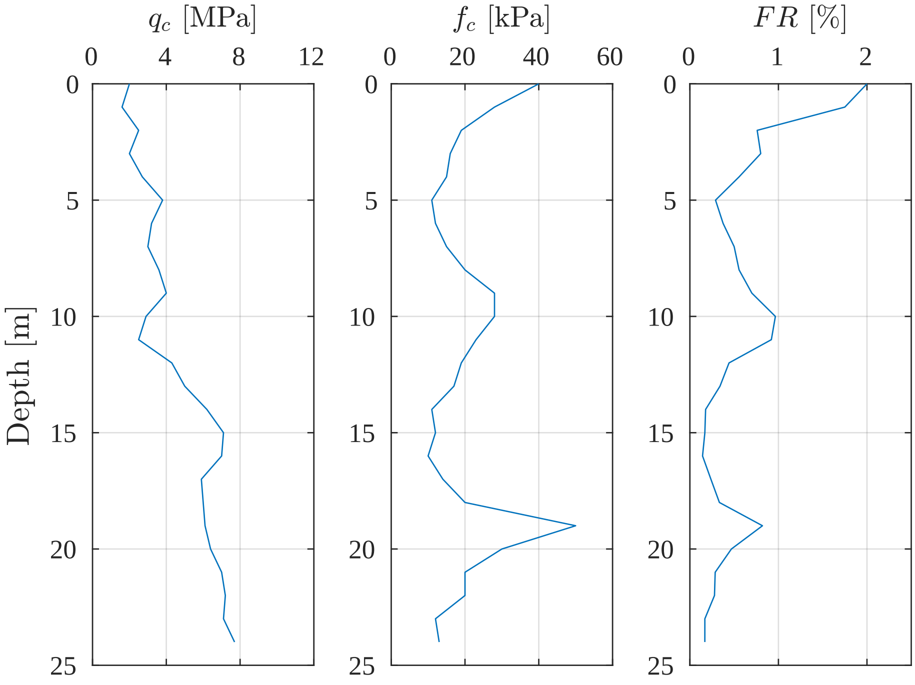

Figure 5.1: Simplified tip resistance q_c, skin friction f_c, and friction ratio FR, plotted versus soil depth.

5.2 Dynamic soil resistances

The profiles for the amplitude values of the dynamic shaft resistance τ_d and dynamic toe resistance q_d (stresses) were estimated with the method described in Section 2.5.3. The simplified profiles for the tip resistance and skin friction in Figure 5.1 were taken as the static soil resistances, i.e., $q_s = q_c$ and $\tau_s = f_c$. Furthermore, the friction ratio profile in Figure 5.1 was used, and the empirical liquefaction factor L was assumed to 7. The resulting profiles for the dynamic toe and shaft resistances are shown in Figure 5.2, while the calculations are described more in-depth in Appendix A.2.

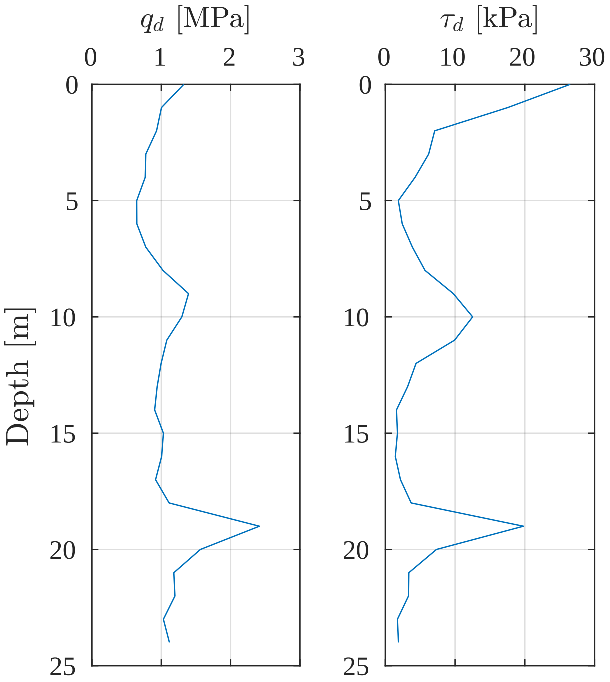

Figure 5.2: Estimated dynamic toe resistance q_d, and dynamic shaft resistance τ_d, plotted versus penetration depth.

The amplitude values of the dynamic soil resistances $R_{s,max}$ and $R_{t,max}$ (forces) are then determined as

$$R_{s,max} = \Omega_p \int_0^z \tau_d \, dz \tag{5.1}$$

$$R_{t,max} = q_d(z) A_p \tag{5.2}$$

where Ω_p is the perimeter of the sheet pile, A_p is the area of the sheet pile, and z is the depth of the sheet pile toe.

5.3 Soil model

A soil model describing how the dynamic soil resistances R_t and R_s vary between the previously determined amplitude values $R_{t,max}$ and $R_{s,max}$ during the vibratory driving is needed to model and simulate vibratory driving.

After testing both the linear and hyperbolic soil models described in Section 2.5.1, it was decided to only go forward with the linear soil models. There were two main reasons for this decision: Firstly, the hyperbolic soil models along with the recommended input parameters gave results that were very different from the ones seen in the reference case. Secondly, it was realised that the hyperbolic soil models would be rather hard to implement in the FE model.

The parameters in Table 5.1 were assumed for the linear soil models shown in Figure 5.3. The parameters correspond to the values recommended by Moulai-Khatir et al. [7].

Table 5.1: Parameters for the linear soil models.

Parameter	Value	Unit
Toe quake, Q_s	2.5	mm
Shaft quake, Q_t	2.8	mm

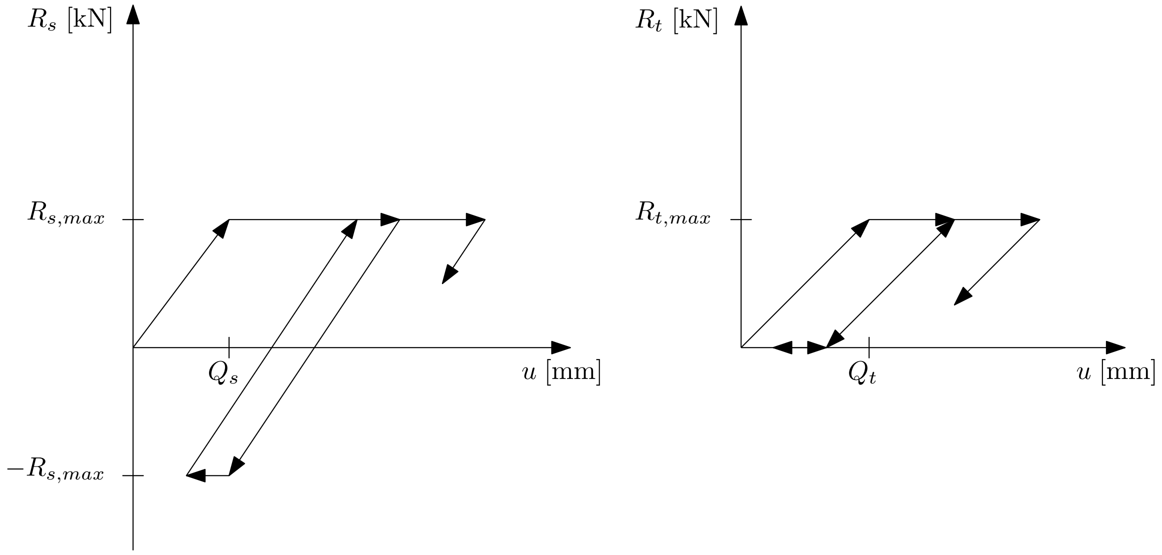

Figure 5.3: Linear soil models for the shaft resistance R_s and toe resistance R_t.

5.4 Vibrator

The vibrator used in the field study by Viking [2] was a MRZV 800V from ABI. The same model of vibrator was assumed in the master's dissertation. The driving frequency was assumed to 41 Hz, corresponding to the field study by Viking [2]. The bias mass of the vibrator unit was estimated based on the dynamic mass (2,450 kg) from Table 4.1, and the total mass (3,470 kg) from a data sheet for the MRZV 800V vibrator. Finally, it was assumed that the leader could exert an upwards directed force on the vibrator, with a magnitude corresponding to the maximum extraction force of the leader (140 kN) and a downwards directed force with a magnitude corresponding to the maximum driving force of the leader (70 kN). This force will from here on be referred to as leader force. The assumed vibrator parameters are summarised in Table 5.2.

Table 5.2: Summarized vibrator properties.

Parameter	Value	Unit
Driving frequency, f_d	41	Hz
Eccentric moment, M_e	0–12	kgm
Dynamic weight of vibrator unit, m_v	2,450	kg
Bias mass of vibrator unit, m_0	1,020	kg
Leader force, F_l	−140–70	kN

.

5.5 Sheet pile

A simplified cross section, where the interlocks were omitted, was created based on the PU-16 sheet pile used in the field study by Viking [2]. The simplified cross section is shown in Figure 5.4, while properties and assumed material parameters are shown in Table 5.3. The length of the sheet pile was assumed to 14 meters, as in the field study by Viking [2].

Table 5.3: Sheet pile properties and material parameters.

Parameter	Value	Unit
Length, L_p	14	m
Area, A_p	84.98	cm^2
Perimeter, Ω_p	170.6	cm
Moment of inertia, I_x	4,890	cm^4
Moment of inertia, I_y	27,957	cm^4
Plastic section modulus, $W_{pl,x}$	369	cm^3
Plastic section modulus, $W_{pl,y}$	1,363	cm^3
Young's modulus, steel, E_s	210	GPa
Yield stress, steel, f_y	355	MPa
Density, steel, ρ_s	7,800	kg/m^3

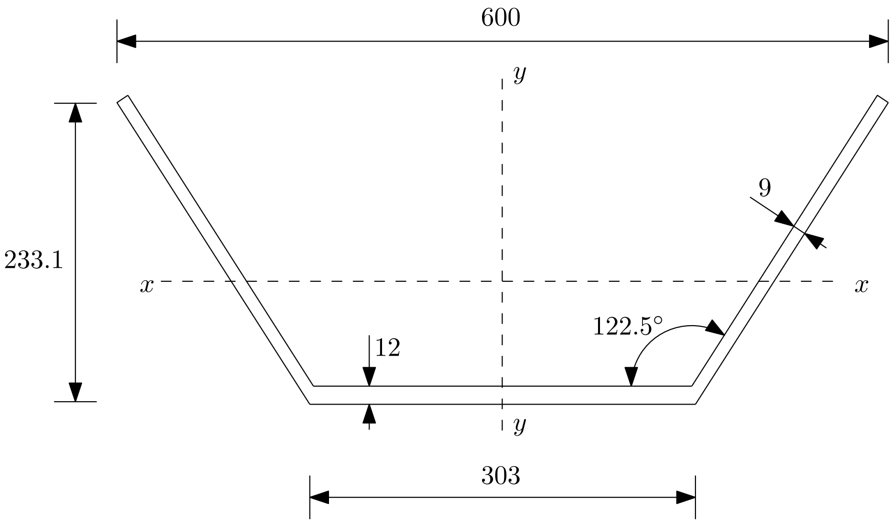

Figure 5.4: Illustration of the simplified cross section of a PU-16 sheet pile.

6 Finite Element model

The first model established of vibratory driving of steel sheet piles was a Finite Element (FE) model, in the commercial FE analysis software Abaqus. The model was to simulate the reference case, in Chapter 5, with vibratory driving-, and impact simulations, to conclude whether a potential stop criterion may potentially be formed, or not. The procedures followed to establish this FE model are documented in this chapter.

The input code for the FE model may be seen in Appendix C.

6.1 Model of steel sheet pile

This section handles the modelling of the sheet pile, seen in Figure 6.1. Its properties and other parameters are described in the following subsections.

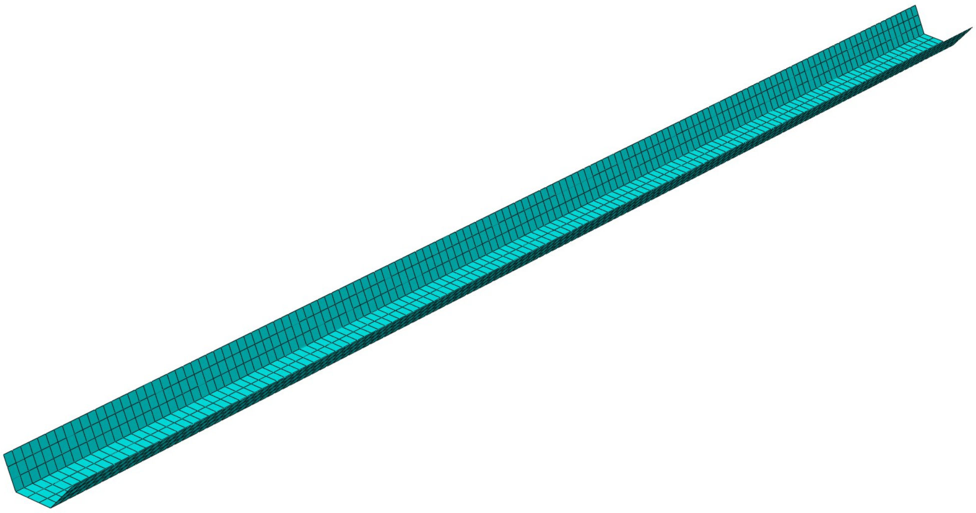

Figure 6.1: FE model of the steel sheet pile in Abaqus.

6.1.1 Properties

The sheet pile part was modelled as a three-dimensional, deformable, homogeneous shell section. The simplified cross-section of the sheet pile, that is described in Chapter 5, was modelled as the top surface, to create a homogeneous cross section. The properties of the sheet pile, and vibratory parameters, may be seen in Table 6.1.

Table 6.1: Model parameters of the sheet pile and vibrator unit.

Parameter	Value	Unit
Sheet pile length, L_p	14	m
Sheet pile cross-section area, A_p	84.98	cm^2
Sheet pile perimeter, Ω_p	170.6	cm
Young's modulus, steel, E_s	210	GPa
Yield stress, steel, f_y	355	MPa
Density, steel, ρ_s	7,800	kg/m^3
Driving frequency, f_d	41	Hz
Eccentric moment, M_e	0–12	kgm
Dynamic mass of vibrator unit, m_v	2,450	kg
Bias mass of vibrator unit, m_0	1,020	kg
Leader force, F_l	−140–70	kN

6.1.2 Damping

Material damping, in the form of β-damping, was added to the FE model. The internal viscous damping from the explicit simulation, and the hysteresis damping from the soil resistance was not considered to reduce the effects of vibratory overtones and natural frequencies enough. The damping coefficient β was set to 3.03E-05, to give a damping ratio ζ of 0.01 at 105 Hz. This was done to merely reduce the influence of high frequencies in the simulations. β-damping is described more thoroughly in Appendix A.3.

Furthermore, the potential mechanical damping from the elastomere pads in the suppressor housing was neglected. The reason for this was that not enough information about the potential damping these provide to the whole vibratory system was found.

6.1.3 Loads

To replicate the reference case in Chapter 4, the same exerting forces from the reference case was applied to the FE model. As the driving capacity F_d is transferred to the sheet pile through a hydraulic clamp, the driving capacity in the FE model was applied likewise. An area of 0.2 by 0.2 metres was partitioned in the model, as a common hydraulic clamp was assumed to be of that size. However, the size of the partitioned area was deemed irrelevant, if no yield stresses occur in the partitioned area. All exerting forces were then applied in this area as surface traction stresses. This includes the weight of the bias mass and the dynamic mass, the leader forces, and the driving capacity of the vibrator. The dynamic mass was, in addition, added as an inertia, in the same imagined clamping area, to give the dynamic system a realistic mass. Figure 6.2 shows the partitioned clamp area.

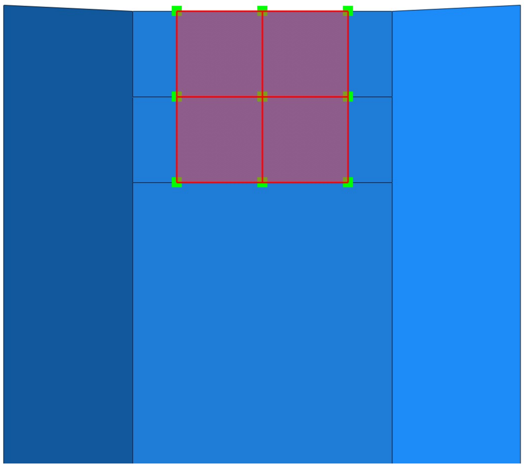

Figure 6.2: The head of the sheet pile, with the partitioned area marked in red, and the added inertia marked in green.

6.1.4 Boundary conditions

Due to the lateral support of the soil acting upon the sheet pile during vibratory driving, no global buckling phenomena have been documented. In a previous master's dissertation regarding vibratory driving of sheet piles, by Lund Tebäck [15], the lateral soil support was modelled with the Winkler model, where the soil is simulated as lateral springs. Lund Tebäck [15] concluded that the lateral springs had a neglectable influence on the impact behaviour of the sheet pile. Therefore, for simplicity, displacement boundary conditions in the lateral plane were applied to the sheet pile along the soil depth, preventing any displacements in the lateral plane. This was not applied to the sheet pile toe, to accurately be able to capture the local buckling behaviour there. A similar boundary condition was applied to the top of the sheet pile, where the partitioned area was created. This was done to simulate the hydraulic clamp's rigid connection to the sheet pile, which hinders the sheet pile from moving in the lateral plane.

An initial velocity was given to the sheet pile at the beginning of all simulations, to reduce the time it takes for the vibratory driving to reach a steady state behaviour. The initial velocity was determined based on the driving parameters of previously run simulations. Further, the velocity at the time of a new vibratory driving period was, therefore, chosen as the initial velocity.

6.1.5 Mesh

The element type S4R, with linear interpolation order, and reduced integration was used. The elements were of quadratic shape, and distributed structurally along the sheet pile, as seen in Figure 6.3.

The use of reduced integration can cause a reduction in stiffness at the element level. This has the potential to interfere with the results from the simulations. The reduction in stiffness becomes larger as the element sizes is decreased. This was considered in the performed convergence study, seen in Section 6.3, by monitoring the total energy in the dynamic system. Additionally, the element sizes used in the simulations can be seen in Section 6.3, where a global element size of 50 mm for the sheet pile was determined, and an element size of 25 mm for the sheet pile toe was decided upon. This was done to minimise the required computing time, and to have a fine enough mesh in the sheet pile toe to properly capture local buckling during an impact.

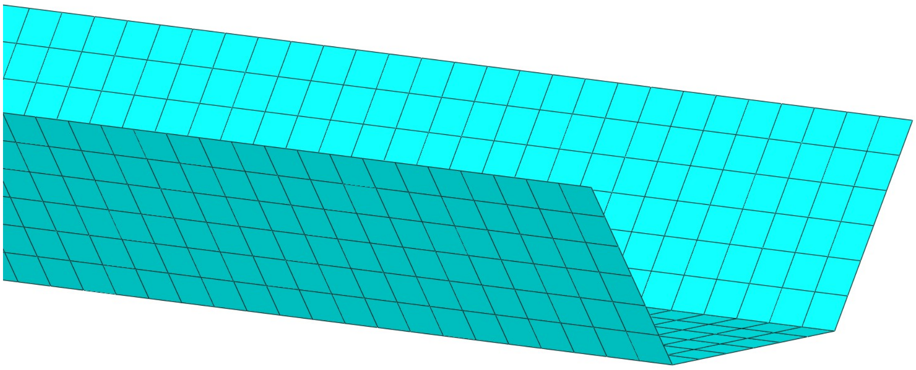

Figure 6.3: Mesh of the sheet pile-head, with an element size of 50 mm.

6.2 Model of soil and obstacle

This section handles the method of modelling the soil and the impact obstacle in the FE model.

6.2.1 Shaft resistance

The soil shear-strength was modelled with the use of Connector elements, as seen in Figure 6.4. The connectors were placed in intervals of one-metre, and represent the integrated total friction shear force in between those intervals. Depending on the penetration depth of the sheet pile, the number of connectors vary. The behaviour of each connector was determined from the model soil resistance in Chapter 5, that was based upon the CPT performed in the reference case in Chapter 4. One end of the connectors was defined at one of four partitioned intersections at each interval, as shown in Figure 6.4, while the other end was defined in an arbitrary point connected to the ground.

The connector's category was set to basic, with the connector type set to solely translational cartesian, to follow the global coordinate system. Thereafter, the characteristic of the shaft resistance, seen in Figure 5.3, were replicated with linear elastic behaviour, and non-linear plastic behaviour.

Another possible method of defining connector elements, instead of using the manual Abaqus interface, is to rewrite the input-file. Connector elements could, thereby, have been assigned to every node, rather than in intervals, and perhaps given a more realistic shaft friction model. With a fine enough mesh, a low amount of connector elements might cause yielding in the nodes they are connected to. This potential problem would be avoided with a larger amount of connector elements.

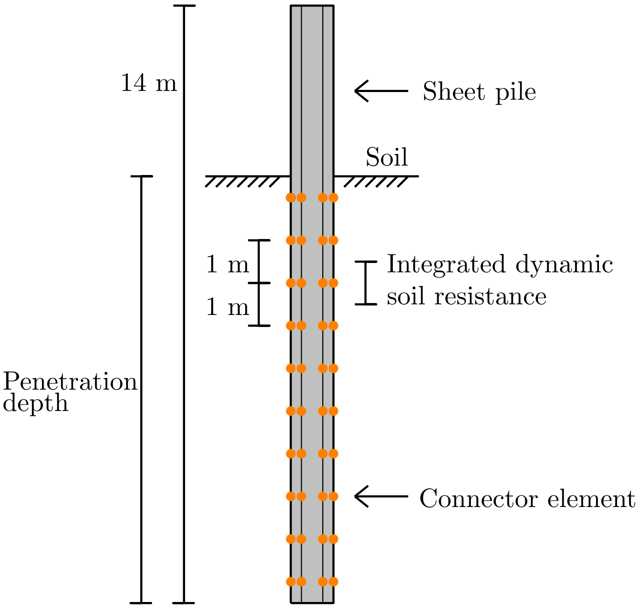

Figure 6.4: Illustration showing the defined connector elements along the sheet pile at a penetration depth of ten metres.

Beforehand, a similar method of defining the connector elements was tested. Each interval only had one connector element, instead of four. This element was connected to an arbitrary ground in one end, and to a reference point in the other end. Further, this reference point was coupled to the same four partitioned intersections mentioned earlier. By having a multitude of nodes coupled to a singular reference point, implicit simulation methods had to be applied to solve the restriction in vertical displacement that occurred, making the model behave unrealistic, and therefore making it unusable.

6.2.2 Toe resistance

The simulations with the FE model mainly focused on impacts, where the soil toe resistance is replaced with the resistance of an obstacle instead. Furthermore, the modelled soil resistances, in Chapter 5, shows that the toe resistance is merely a fraction of the magnitude of the shaft resistance. Making the effect of the toe resistance have a potential insignificant influence on the results. This, and the complexity of adding the toe resistance behaviour, are reasons why it was not implemented into the FE model.

However, as the FE model was calibrated towards the reference case model, where toe resistance occurred during the vibratory driving, the FE model was lacking that contribution during non-impact simulations.

6.2.3 Impact obstacle

The obstacle used during explicit impact simulations can be seen in Figure 6.5. A solid sphere, with a diameter of 0.4 metres was modelled. The Young's modulus of the obstacle was set to 50,000 MPa, the same magnitude as good quality granite, to hinder potential interference during impacts. A more advanced model would take failure modes of the obstacle, and potential displacement of the obstacle into account as well, but this is beyond the scope of the dissertation.

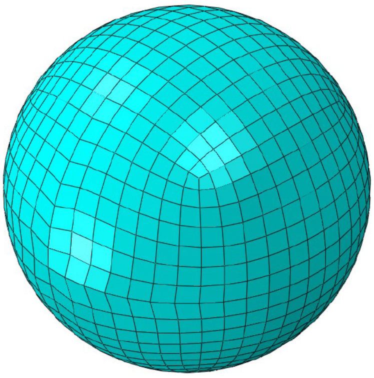

Figure 6.5: FE model of the impact obstacle, simulating a boulder.

The mesh of the obstacle was set using elements of the type C3D8R, with linear geometric order, reduced integration, and hourglass control. The element size was chosen as 25 mm, as to match the element size of the sheet pile toe.

The interaction between the obstacle and the sheet pile was modelled to have a penalty tangential behaviour, and hard contact normal behaviour. Penalty interaction implies that regular Coulomb friction is applied, while hard contact interaction implies that pressure between the sheet pile and obstacle only occur during contact. This may be altered into a continuous reduction in pressure after contact ceases, e.g., a linear or exponential reduction change.

The surface of the modelled boulder was assumed to be rough, and the whole circumference of the sheet pile toe was assumed to be supported by lateral soil pressure. Therefore, next to no slip between the sheet pile and the boulder was assumed to occur. Thus, the friction coefficient for the interaction was set to a sizeable value.

6.3 Convergence study

A convergence study was performed on the impact simulation at a ten-metre penetration depth at the middle of the web, to reassure accurate results without consuming too much computing power. The reference case in Chapter 4 functioned as a template, and the effects of the impact was assured to be captured properly.

6.3.1 Element size

The effect of the chosen element size of the sheet pile was studied, to find out at what element size the result had converged and gave sufficient results. Due to computational limitations of the software, and the hardware, no smaller element sizes than 25 mm were studied. The number of increments became too large for Abaqus, and the CPU time required to run the simulations were unreasonable when using any smaller element size. Additionally, with the added material damping, the required time increment size for stability was lowered drastically, resulting in even larger amounts of computing power being required to run the simulations.

A purpose of the master's dissertation is to achieve a general understanding of the vibratory driving process, rather than producing highly accurate results. Therefore, only a minor study was conducted, where a global element size was chosen for the sheet pile, while a smaller element size was chosen for the sheet pile toe and obstacle. The element sizes tested, the number of nodes in the simulation, and the stability time increment size required can be seen in Table 6.2.

Table 6.2: Convergence study of element sizes of the sheet pile during vibratory driving.

Element size of the sheet pile [mm]	Element size of the sheet pile toe, and obstacle [mm]	Number of nodes	Stability time increment size [s]
100	50	7,231	8.74e-07
100	25	11,123	2.45e-07
50	25	14,623	2.45e-07
25	25	24,073	2.45e-07

The result of the convergence study can be seen in Figure 6.6, where the peak acceleration during vibratory driving versus the number of nodes used to simulate the process can be seen. It was concluded that the accelerations were still converging with an increasing number of nodes in the simulation. Due to the computational limitations mentioned before, a global element size of 50 mm was chosen to be used for the final simulations. The element size of the sheet pile toe was chosen as 25 mm, to capture the local buckling behaviour as realistically as possible.

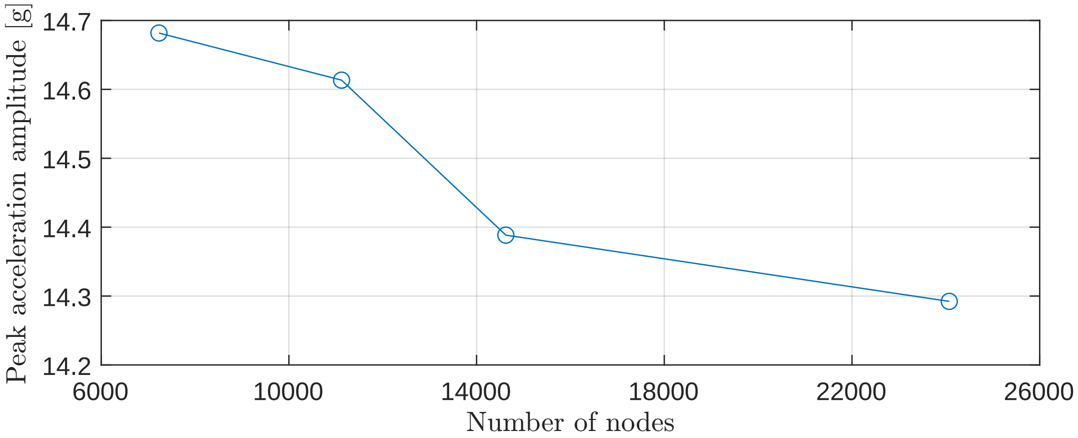

Figure 6.6: Peak acceleration, one-metre below the sheet pile-head, during vibratory driving versus the number of nodes used to simulate the process.

6.3.2 Time increment

As described in Section 3.2, Abaqus estimates the stability requirement of the time increment for the iterations. This is based either on the smallest element size, or the highest frequency affecting the whole model. This is handled automatically by Abaqus. The time increment size may be fixed manually if that is desired. However, Abaqus will not perform an energy oscillation control then, meaning no reassurance that the total energy in the system does not change drastically. This could, nonetheless, be checked manually, although it would not be as efficient.

In addition, as described in Section 3.1, all time increments used in the Central Difference Method, which is used in the explicit Finite Element simulations, are of constant length. With these two factors holding true, there is no need for a converge study of the time increment size, as the stability requirements are deemed to give accurate enough results, and a convergence study has been performed of the element sizes. Furthermore, as mentioned before, immense accuracy is not in the essence of the dissertation, as a more general understanding of the vibratory driving scenarios is sought after.

The time increment size for stability, that Abaqus uses as the time increment size for each individual increment varies with the element size. Table 6.2 shows the estimated stability requirement time increment size during the element size convergence study. These time increments are minuscule, and only a fraction of the period time that the sheet pile is vibratory driven downwards at. This concludes that the increment size is small enough.

6.4 Simulations

The following three simulations were performed with the FE model. The added leader force, and initial velocity to the vibratory driving simulations, and impact simulations were determined in Section 7.4.

6.4.1 Quasi-static buckling

Quasi-static buckling simulations were carried out to study how the contact force between the sheet pile toe and boulder varies with the vertical displacement of the sheet pile, which could create an understanding of how forces develop during impact. Furthermore, the behaviour observed in these simulations were used to model the impact in the SDOF and MDOF models.

The necessary vertical contact force for local buckling to occur was concluded in quasi-static explicit simulations. Three local buckling scenarios were studied: local buckling of the middle of the web, local buckling of the corner between the flange and the web, and local buckling of the edge of the flange. The obstacle described in Section 6.2.3 was pressed against these three locations of the sheet pile toe, as illustrated in Figure 6.8. During the simulation, the obstacle was driven into the sheet pile at a constant velocity, and then retracted at the same pace. To save computing power, only the lowest one-metre of the sheet pile was modelled, as local buckling merely at the toe of the sheet pile was assumed to occur.

During the quasi-static explicit simulations, mass scaling was used to reduce the dynamic effects on the results. The mass of the sheet pile was increased to a magnitude 100,000 times its original mass, to remove the influence of acceleration in the results.

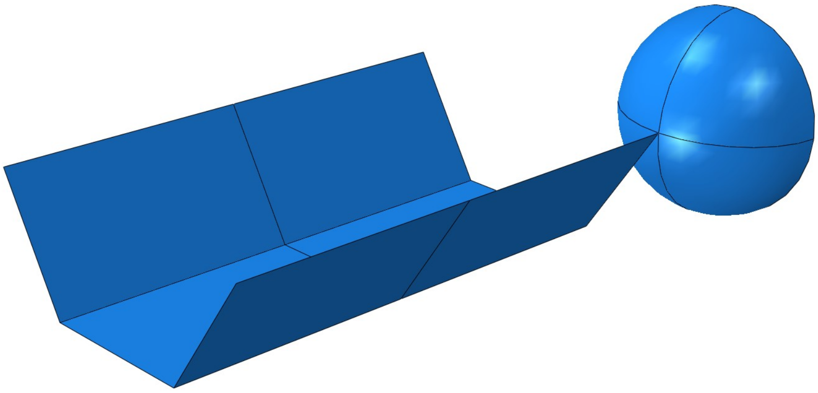

Figure 6.7: Set-up of the displacement driven buckling simulations of the sheet pile toe.

6.4.2 Vibratory driving

Vibratory driving simulations, with the same conditions as in the reference case in Chapter 4 were performed, at the penetration depth of two, six and ten metres. The FE model was calibrated to give resembling results to the reference case, to confirm its applicability as a vibratory driving model, and to confirm that the FE model gives realistic results. If regular vibratory driving cannot be realistically simulated, then the impact results would be irrelevant. The model was deemed to be eligible when the periodic displacements, global penetration speed, and acceleration of the sheet pile were comparable to the reference case. The chosen input parameters can be seen in Table 6.3.

Table 6.3: Input parameters for the vibratory driving simulations.

Penetration depth [m]	Eccentric moment M_e [kgm]	Leader force F_l [kN]
10	6	-30
6	6	-5
2	6	14.5

6.4.3 Impact

Impact simulations, with the same conditions as in the reference case in Chapter 4 were performed, at a penetration depth of ten metres. Three different impact locations were simulated: at the middle of the web, at the corner between the flange and the web, and at the edge of the flange, as shown in Figure 6.8. The obstacle was placed at a vertical distance from the sheet pile determined from the vibratory driving simulations, when the driving process had reached a steady state behaviour and had reached its maximum velocity. At each of the three locations, the effect of two different eccentric moment magnitudes were simulated. These magnitudes were: the reference case eccentric moment of 6 kgm, and an eccentric moment of 12 kgm. The chosen input parameters can be seen in Table 6.4.

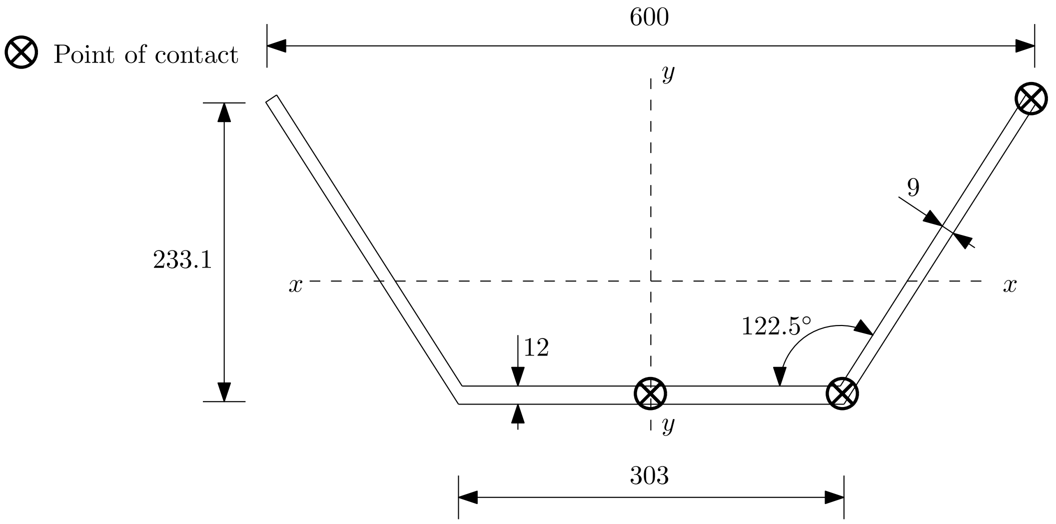

Figure 6.8: Illustration of the three impact locations simulated.

Table 6.4: Input parameters for the impact simulations.

Parameter	Value	Unit
Penetration depth	10	m
Eccentric moment, M_e	6 & 12	kgm
Leader force, F_l	-30	kN

6.5 Results

This section presents the results from the simulations described in Section 6.4. This is followed by an analysis of the results, and the FE model in general in Section 6.6. A more in-depth discussion, and comparisons of the three models are provided in Chapter 9.

6.5.1 Quasi-static buckling

The results of the quasi-static buckling simulations are shown in Figures 6.11–6.12, while the buckling behaviour during a dynamic impact simulation is shown in Figure 6.9.

Figure 6.9 shows the buckling behaviour, when the point of contact is the corner between the flange and the web, for a dynamic impact simulation with an eccentric moment of 12 kgm. The behaviour is similar to the quasi-static behaviour shown in Figure 6.10.

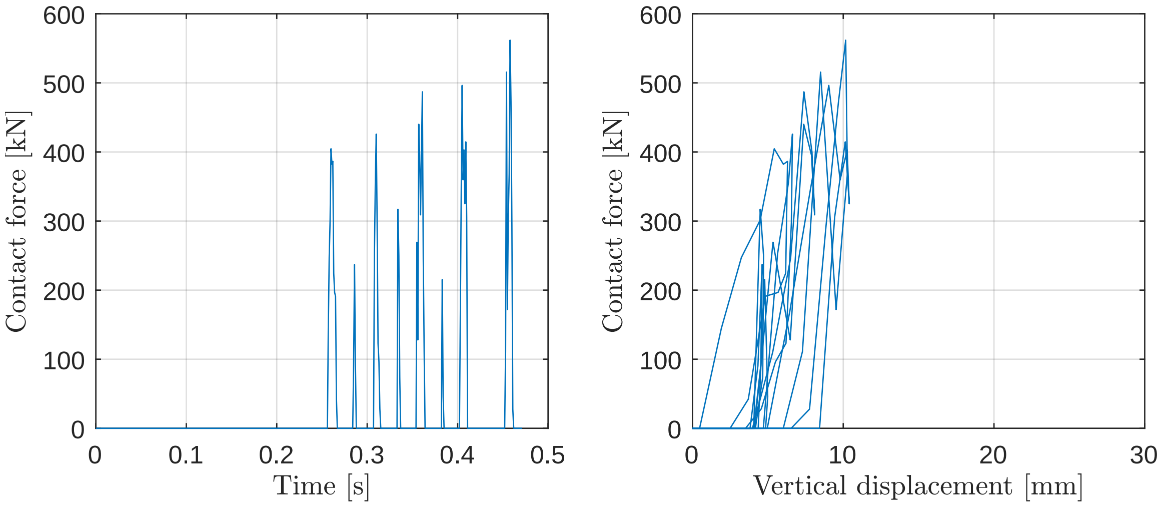

(a) **(b)**

Figure 6.9: Local buckling behaviour of the corner between the web and flange during dynamic impact simulation with an eccentric moment of 12 kgm (a) Contact force versus time. (b) Contact force versus vertical displacement.

Figure 6.10 shows the buckling behaviour when the point of contact is the corner between the flange and the web. The contact force increases linearly to about 200 kN. After this the loading stiffness seem to increase until the load is about 300 kN and then decrease with increasing deformation.

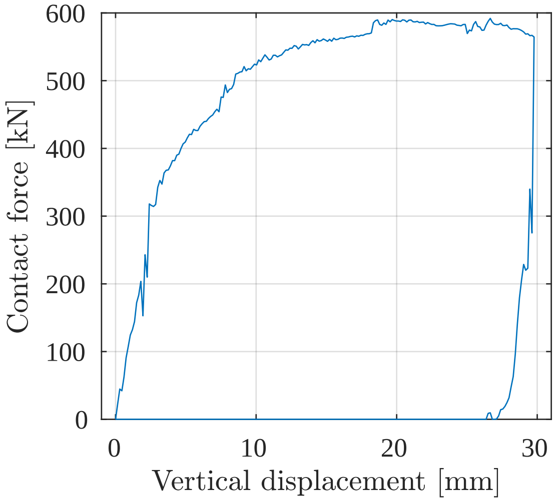

Figure 6.10: Local buckling behaviour of the corner between the web and flange during quasi-static buckling simulation, total contact force versus vertical displacement of the sheet pile.

Figure 6.11 shows the buckling behaviour when the point of contact is the middle of the web. The contact force increases approximately linearly to 270 kN, at which point the vertical displacement is 2.8 mm. After this, the contact force again increases linearly, although with a lower loading stiffness.

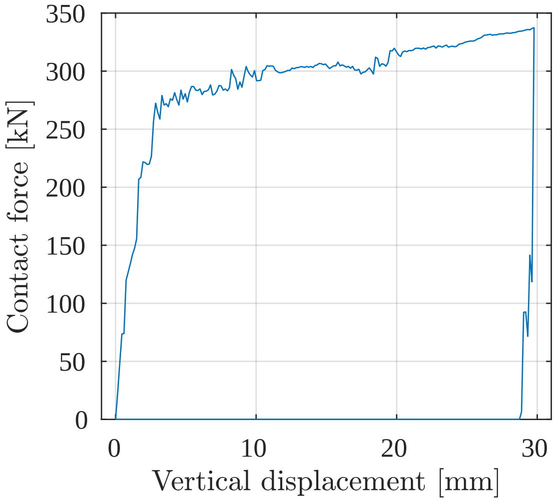

Figure 6.11: Local buckling behaviour of the middle of the web during quasi-static buckling simulation, total contact force versus vertical displacement of the sheet pile.

Figure 6.12 shows the buckling behaviour when the point of contact is the edge of the flange. The contact force increases non-linearly to about 60 kN, at which point the vertical displacement is about 1 mm. After this the contact force varies rather irregularly with the displacement, but the maximum contact force is about 98 kN.

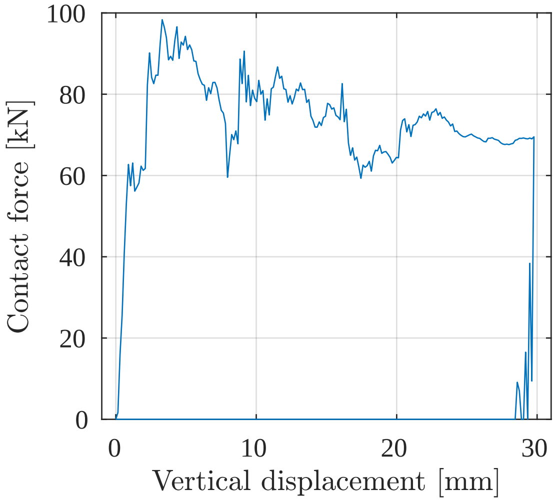

Figure 6.12: Local buckling behaviour of the edge of flange during quasi-static buckling simulation, total contact force versus vertical displacement of the sheet pile.

6.5.2 Vibratory driving

In the following subsections, the displacement and acceleration of a central node in the web of the sheet pile one-metre below the pile head, and the acceleration of a central node in the toe of the sheet pile are plotted versus time, during vibratory driving at penetration depths of two, six, and ten metres.

Note that negative displacements and negative accelerations indicate downwards motion in the soil.

Vibratory driving at two metres penetration depth

A upwards leader force of 14.5 kN was added to the vibratory driving process to reduce the global penetration speed, and an initial upward velocity of 0.45 m/s was added for the driving to reach a steady state more quickly.

The reference case showed a global penetration speed of around 80 mm/s, with an upwards displacement of approximately 3mm, and a downwards displacement of approximately 5 mm, at a penetration depth of two metres. Additionally, the acceleration amplitudes at this penetration depth, in the reference case, showed around 11g for downwards motion, and around 15g for upwards motion.

Figure 6.13 shows that a global penetration speed of 110 mm/s was reached, an upwards displacement of approximately 2.6 mm, and a downwards displacement of approximately 5.4 mm. Figure 6.14 shows that acceleration amplitudes are approximately 12g, for both upwards and downwards motion, near the sheet pile-head. Figure 6.15 shows that acceleration amplitudes are approximately 16g, for both upwards and downwards motion, while being affected by overtone frequencies, at the sheet pile toe.

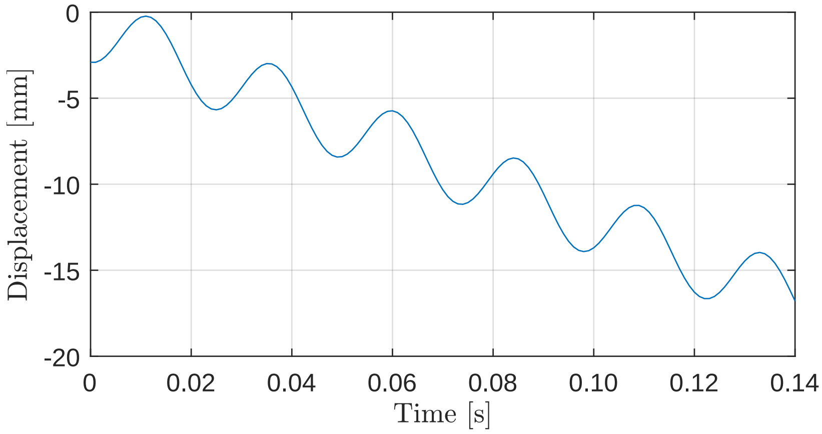

Figure 6.13: Displacement at a penetration depth of two metres, versus time, one-metre below the sheet pile-head.

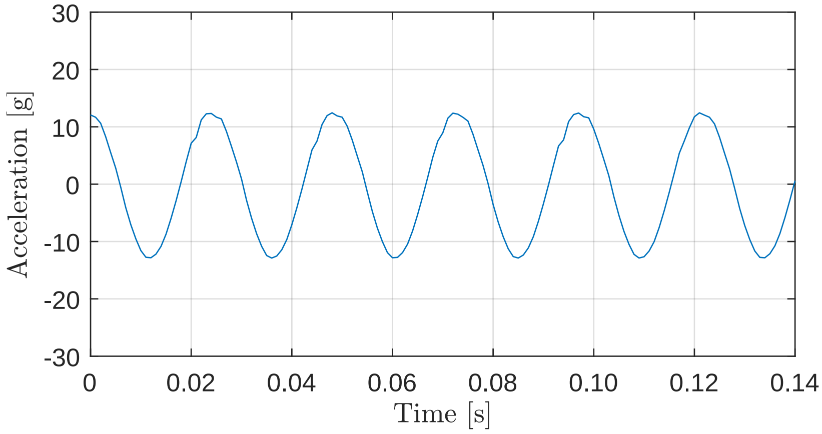

Figure 6.14: Acceleration at a penetration depth of two metres, versus time, one-metre below the sheet pile-head.

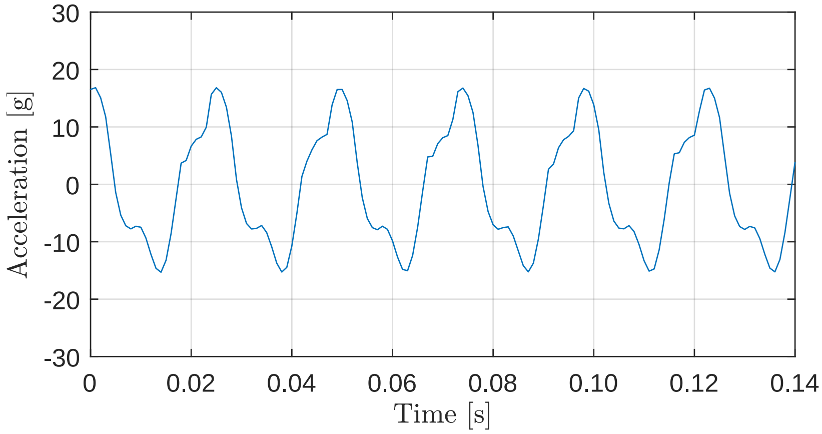

Figure 6.15: Acceleration at a penetration depth of two metres, at the toe of the sheet pile.

Vibratory driving at six metres penetration depth

A downwards leader force of 5 kN was added to the vibratory driving process, and an initial upward velocity of 0.4 m/s was added for the driving to reach a steady state more quickly.

The reference case showed a global penetration speed of around 120 mm/s, with an upwards displacement of approximately 2.5 mm, and a downwards displacement of approximately 5 mm, at a penetration depth of six metres. Additionally, the acceleration amplitudes at this penetration depth, in the reference case, showed around 12g for downwards motion, and around 18g for upwards motion.

Figure 6.16 shows that a global penetration speed of 145 mm/s was reached, an upwards displacement of approximately 2.4 mm, and a downwards displacement of approximately 6 mm. Figure 6.17 shows that the acceleration amplitudes are approximately 12g, for both upwards and downwards motion, near the sheet pile-head. Figure 6.18 shows that the acceleration amplitudes are approximately 19g, for both upwards and downwards motion, while being affected by overtone frequencies, at the sheet pile toe.

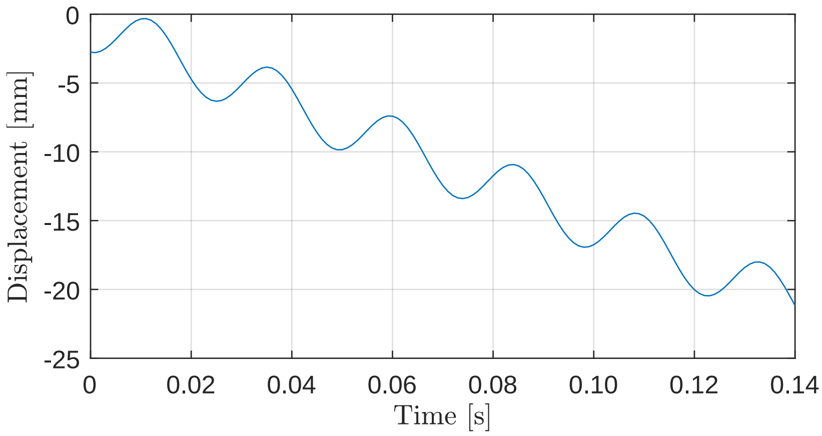

Figure 6.16: Displacement at a penetration depth of six metres, versus time, one-metre below the sheet pile-head.

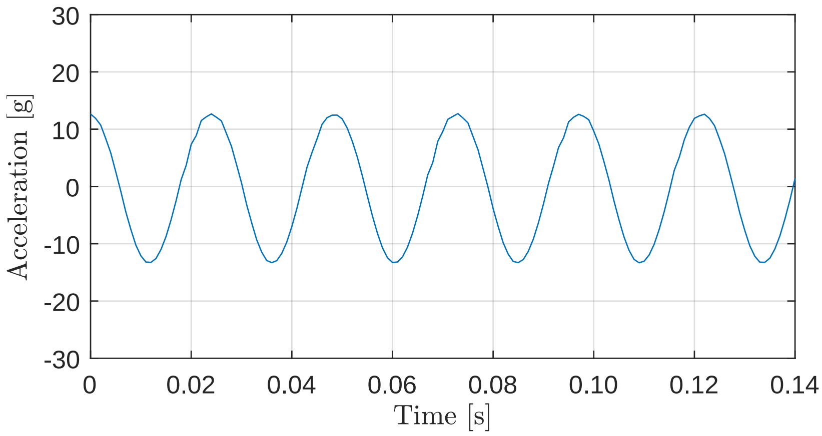

Figure 6.17: Acceleration at a penetration depth of six metres, versus time, one-metre below the sheet pile-head.

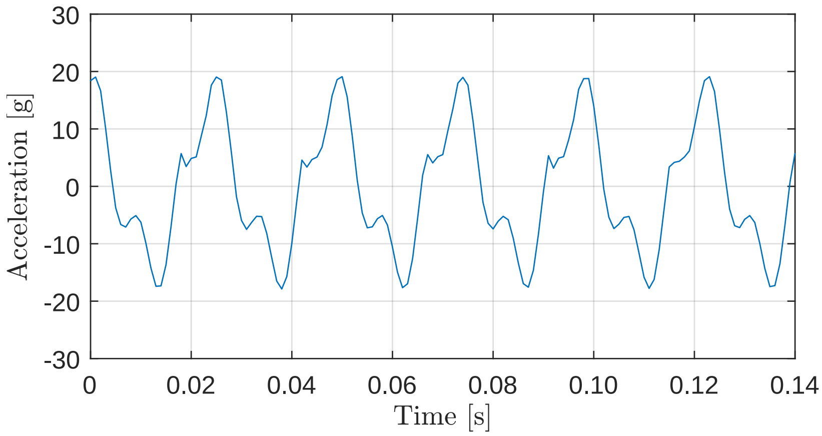

Figure 6.18: Acceleration at a penetration depth of six metres, versus time, at the toe of the sheet pile.

Vibratory driving at ten metres penetration depth

A downwards leader force of 30 kN was added to the vibratory driving process, and an initial upward velocity of 0.4 m/s was added for the driving to reach a steady state more quickly.

The reference case showed a global penetration speed of around 130 mm/s, with an upwards displacement of approximately 2.5 mm, and a downwards displacement of approximately 5 mm, at a penetration depth of two metres. Additionally, the acceleration amplitudes at this penetration depth, in the reference case, showed around 12g for downwards motion, and around 15g for upwards motion.

Figure 6.16 shows that a global penetration speed of 150 mm/s was reached, an upwards displacement of approximately 2.6 mm, and a downwards displacement of approximately 6.4 mm. Figure 6.20 shows that the acceleration amplitudes are approximately 13g, for both upwards and downwards motion, near the sheet pile-head. Figure 6.21 shows that the acceleration amplitudes are approximately 20g, for both upwards and downwards motion, while being affected by overtone frequencies, at the sheet pile toe.

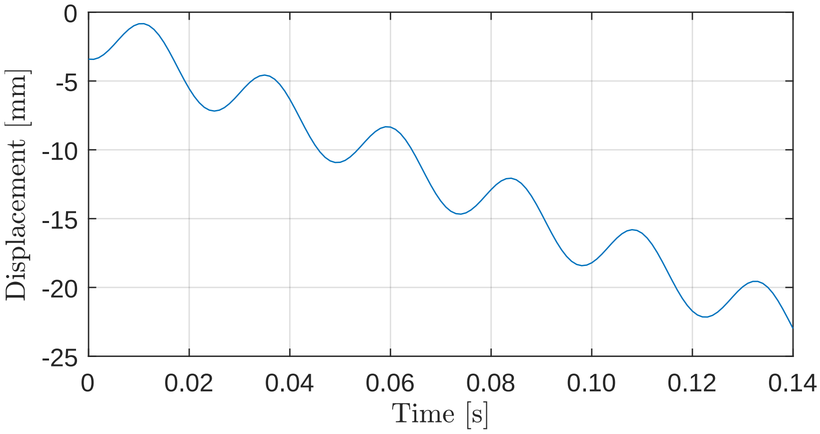

Figure 6.19: Displacement at a penetration depth of ten metres, versus time, one-metre below the sheet pile-head.

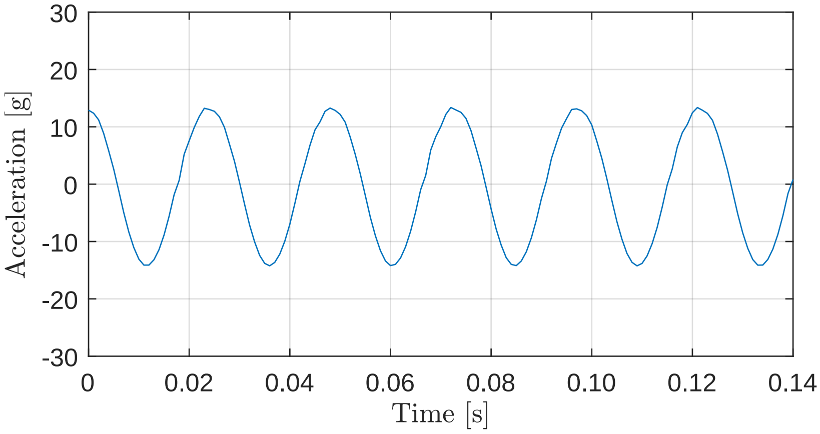

Figure 6.20: Acceleration at a penetration depth of ten metres, versus time, one-metre below the sheet pile-head.

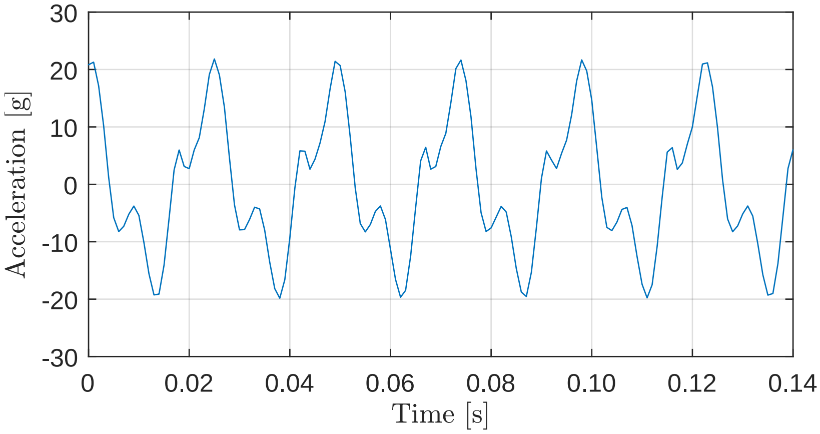

Figure 6.21: Acceleration at a penetration depth of ten metres, versus time, at the toe of the sheet pile.

6.5.3 Impact

In the following subsections, the displacement and acceleration of a central node in the web of the sheet pile one-metre below the pile head, are plotted versus time, before and after impacts. Following this, Fast Fourier Transformations of the acceleration before and after impacts are shown. Thereafter, the local buckling of the sheet pile toe is visualised, with a scale factor of 1.0. This is documented for vibratory driving with an eccentric moment of 6 and 12 kgm, for impacts at three locations, and with a downwards leader force of 30 kN.

Note that negative displacements and negative accelerations indicate downwards motion in the soil, and that the U2-direction refers to the y-axis in the lateral plane.

Impact at the middle of the web–eccentric moment of 6 kgm

The first impact occurs at 0.085 s, and the obstacle is located at a depth corresponding to 17 mm, in Figure 6.22.

Figure 6.23 shows that the acceleration amplitudes are approximately 13g before impact, for both upwards and downwards motion. After the impacts, the acceleration amplitudes are approximately 17g for upwards motion, and 15g for downwards motion, when disregarding potential data deviations. This is a 30% increase for upwards acceleration, and a 15% increase for downwards acceleration. Furthermore, the Fast Fourier Transformations in Figure 6.24 shows an increase in acceleration amplitude from 13g to 16g, at the driving frequency of 41 Hz, after the first impact. This is a 23% increase.

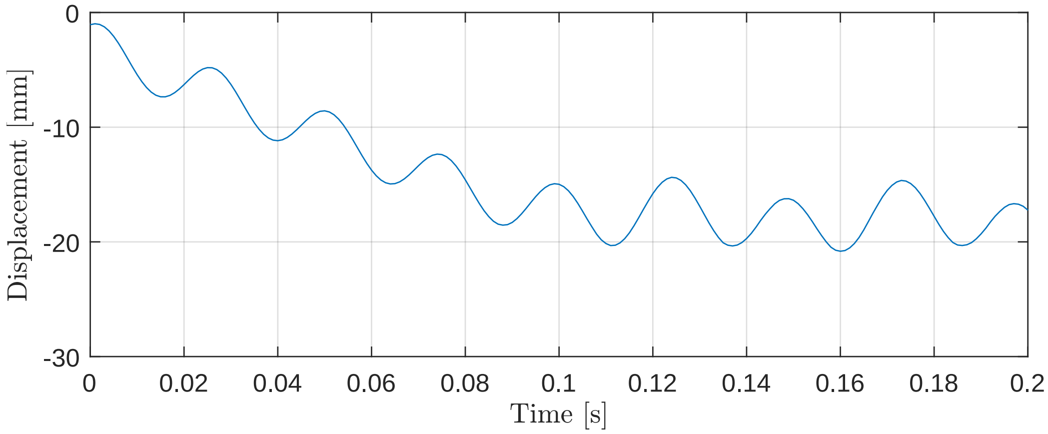

Figure 6.22: Displacement at a penetration depth of ten metres, versus time, one-metre below the sheet pile-head, before and after impacts.

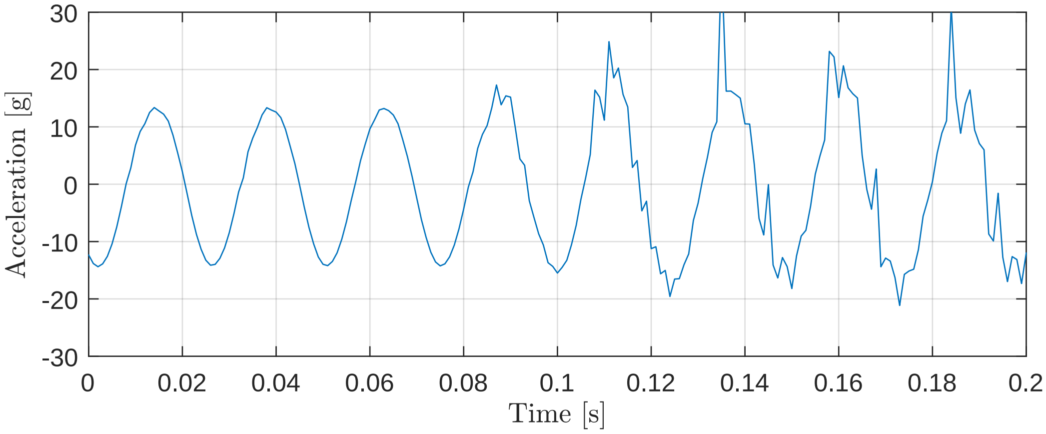

Figure 6.23: Acceleration at a penetration depth of ten metres, versus time, one-metre below the sheet pile-head, before and after impacts.

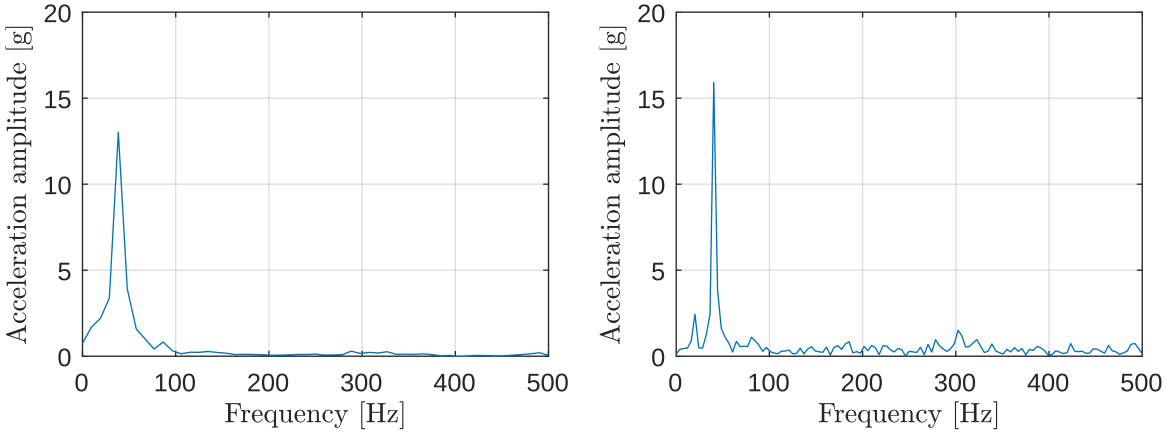

(a) **(b)**

Figure 6.24: (a) Fast Fourier Transformation of the accelerations in Figure 6.23 before an impact. (b) Fast Fourier Transformation of the accelerations in Figure 6.23 after impacts.

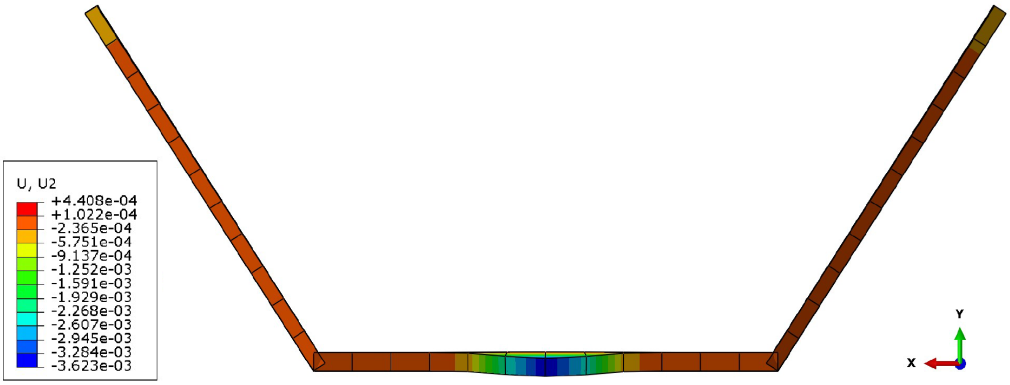

Figure 6.25: Local buckling of the web of the sheet pile toe, seen in the lateral plane, after ten impacts. The displacement in the vertical direction, into the paper, of the middle of the web was approximately 4 mm.

Impact at the corner between the flange and web–eccentric moment of 6 kgm

The first impact occurs at 0.085 s, and the obstacle is located at a depth corresponding to 17 mm, in Figure 6.26.

Figure 6.27 shows that the acceleration amplitudes are approximately 13g before impact, for both upwards and downwards motion. After the impacts, the acceleration amplitudes are approximately 18g for upwards motion, and 16g for downwards motion, when disregarding potential data deviations. This is a 38% increase for upwards acceleration, and a 23% increase for downwards acceleration. Furthermore, the Fast Fourier Transformations in Figure 6.28 shows an increase in acceleration amplitude from 13g to 18g, at the driving frequency of 41 Hz, after the first impact. This is a 38% increase.

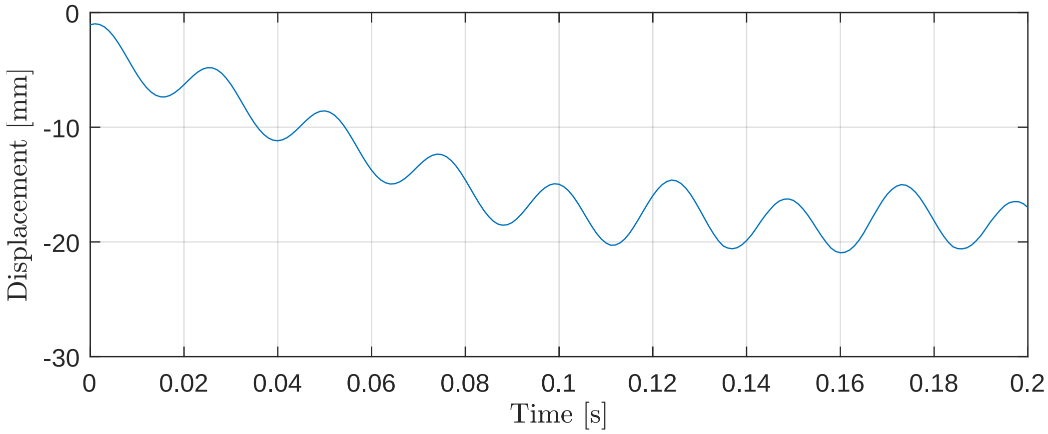

Figure 6.26: Displacement at a penetration depth of ten metres, versus time, one-metre below the sheet pile-head, before and after impacts.

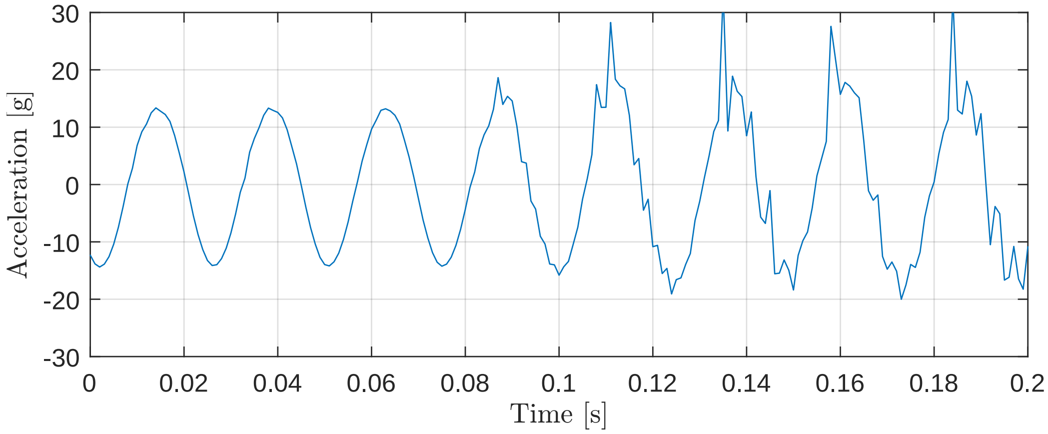

Figure 6.27: Acceleration at a penetration depth of ten metres, versus time, one-metre below the sheet pile-head, before and after impacts.

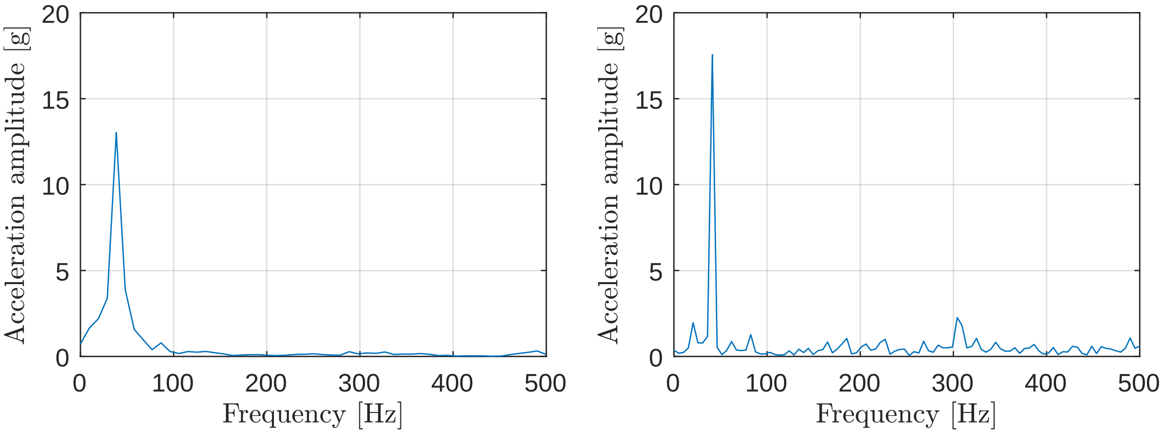

(a) **(b)**

Figure 6.28: (a) Fast Fourier Transformation of the accelerations in Figure 6.27 before an impact. (b) Fast Fourier Transformation of the accelerations in Figure 6.27 after impacts.

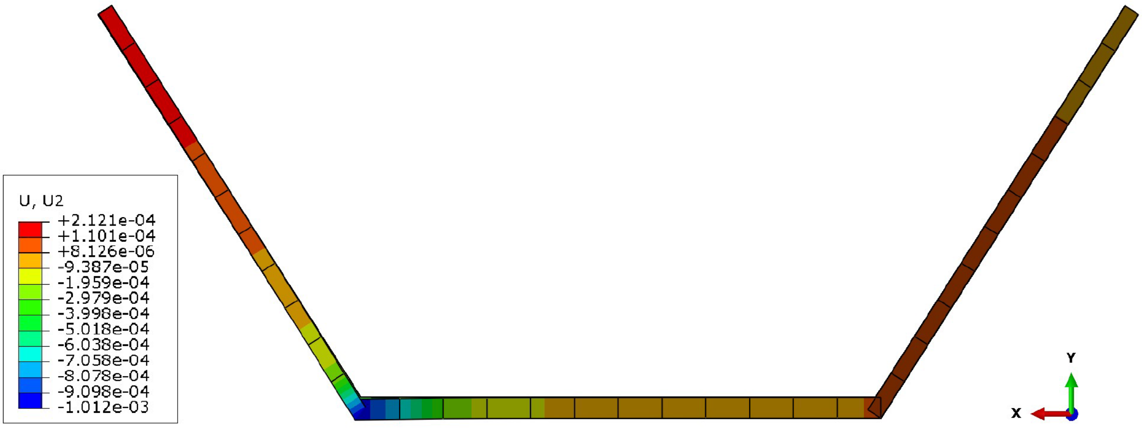

Figure 6.29: Local buckling of the corner between the flange and the web of the sheet pile toe, seen in the lateral plane, after ten impacts. The displacement in the vertical direction, into the paper, of the corner between the flange and the web was approximately 2 mm.

Impact at the edge of the flange–eccentric moment of 6 kgm

The first impact occurs at 0.085 s, and the obstacle is located at a depth corresponding to 17 mm, in Figure 6.30.

Figure 6.31 shows that the acceleration amplitudes are approximately 13g before impact, for both upwards and downwards motion. After the impacts, the acceleration amplitudes are approximately 15g, for both upwards and downwards motion, when disregarding potential data deviations. This is an increase of 15% in acceleration. Furthermore, the Fast Fourier Transformations in Figure 6.32 shows an increase in acceleration amplitude from 13g to 15g, at the driving frequency of 41 Hz, after the first impact. This is a 15% increase.

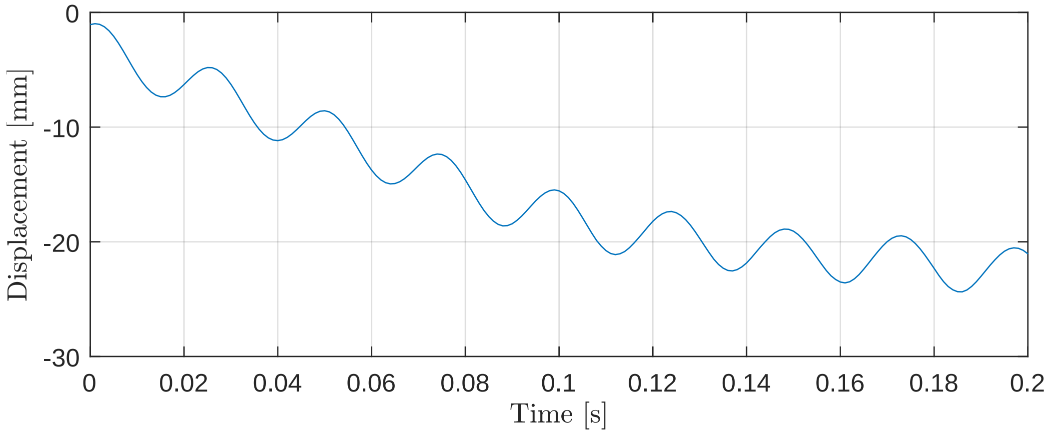

Figure 6.30: Displacement at a penetration depth of ten metres, versus time, one-metre below the sheet pile-head, before and after impacts.

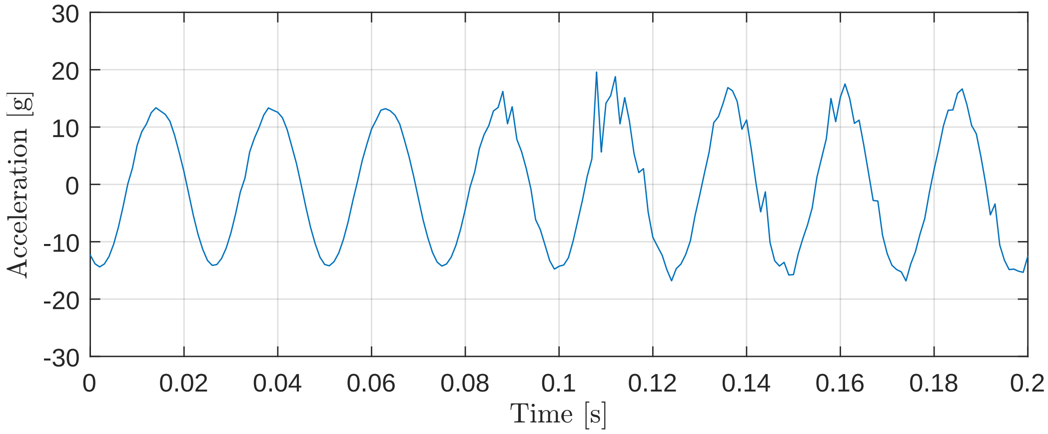

Figure 6.31: Acceleration at a penetration depth of ten metres, versus time, one-metre below the sheet pile-head, before and after impacts.

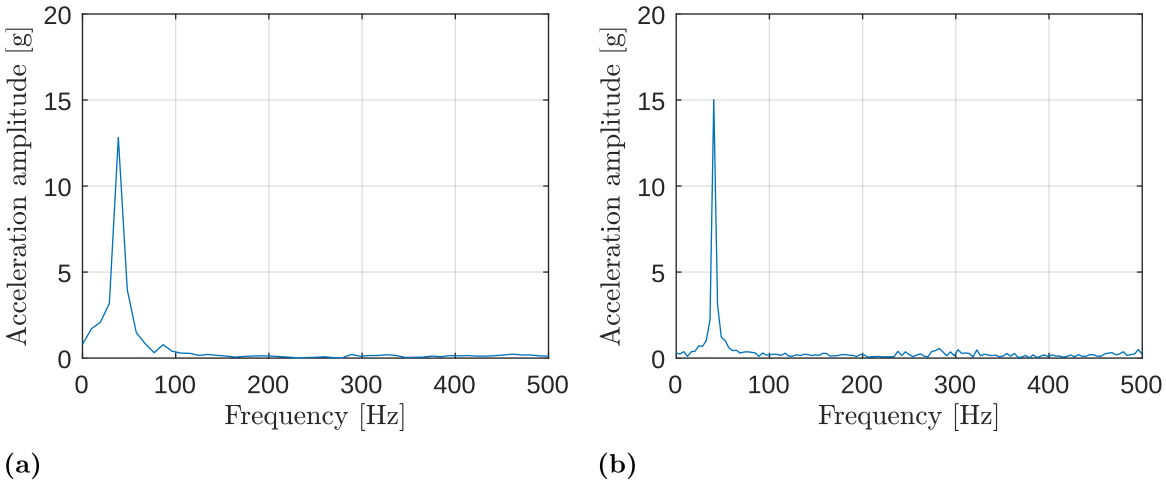

Figure 6.32: (a) Fast Fourier Transformation of the accelerations in Figure 6.27 before an impact. (b) Fast Fourier Transformation of the accelerations in Figure 6.27 after impacts.

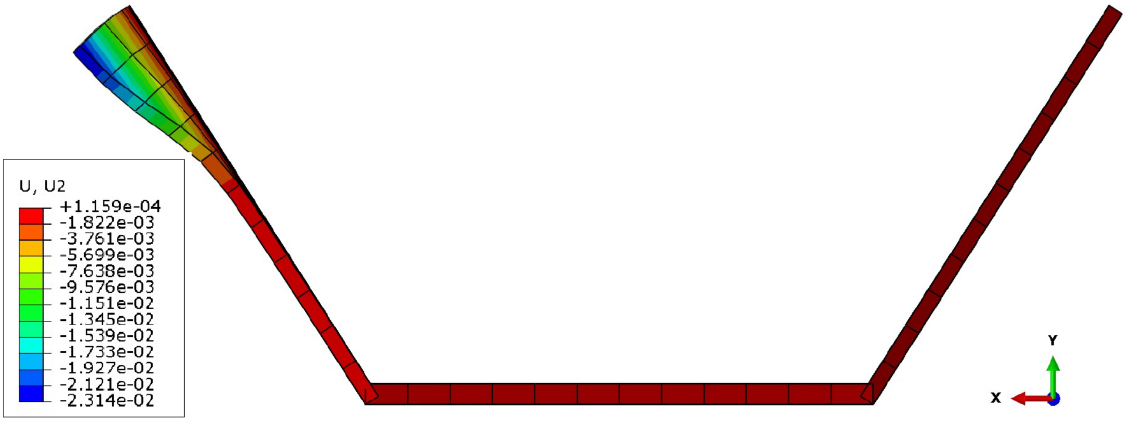

Figure 6.33: Local buckling of the flange of the sheet pile toe, seen in the lateral plane, after ten impacts. The displacement in the vertical direction, into the paper, of the flange was approximately 20 mm.

Impact at the middle of the web–eccentric moment of 12 kgm

The first impact occurs at 0.105 s, and the obstacle is located at a depth corresponding to 60 mm, in Figure 6.34.

Figure 6.35 shows that the acceleration amplitudes are approximately 25g before impact, for both upwards and downwards motion. After impacts the acceleration amplitudes are approximately 34g for upwards motion, and 28g for downwards motion, when disregarding potential data deviations. This is an increase of 36% in upwards acceleration, and an increase of 12% in downwards acceleration. Furthermore, the Fast Fourier Transformations in Figure 6.36 shows an increase in acceleration amplitude from 21g to 30g, at the driving frequency of 41 Hz, after the first impact. This is a 42% increase.

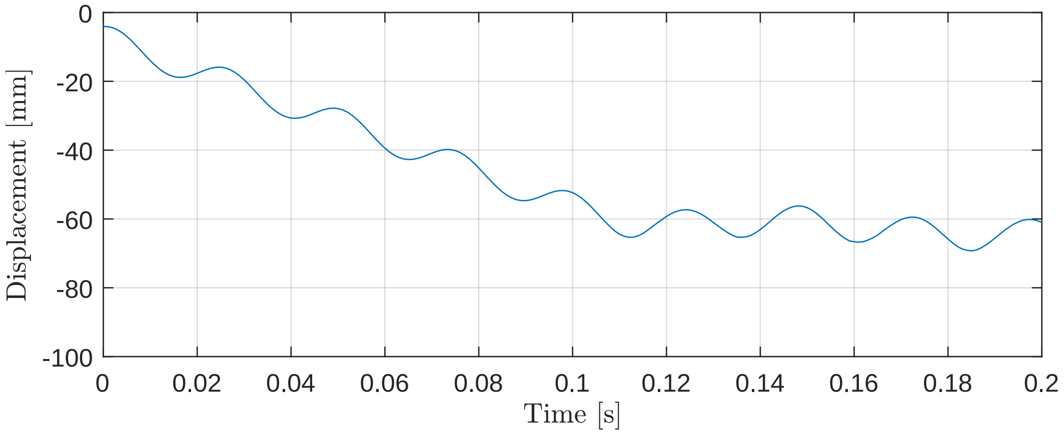

Figure 6.34: Displacement at a penetration depth of ten metres, versus time, one-metre below the sheet pile-head, before and after impacts.

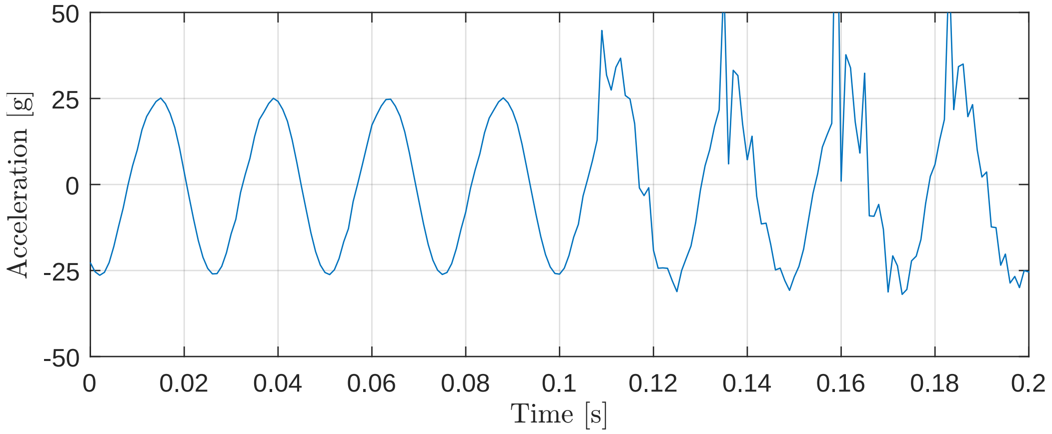

Figure 6.35: Acceleration at a penetration depth of ten metres, versus time, one-metre below the sheet pile-head, before and after impacts.

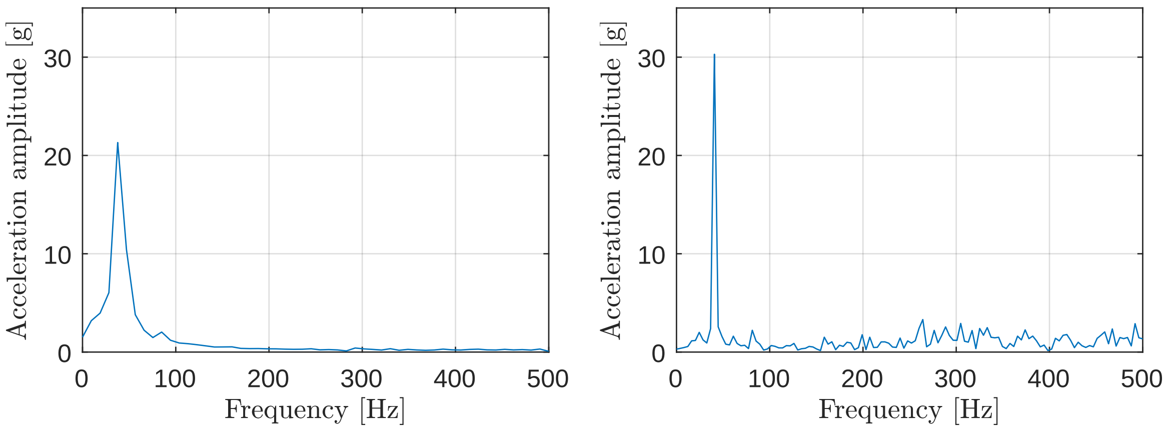

(a) **(b)**

Figure 6.36: (a) Fast Fourier Transformation of the accelerations in Figure 6.35 before an impact. (b) Fast Fourier Transformation of the accelerations in Figure 6.35 after impacts.

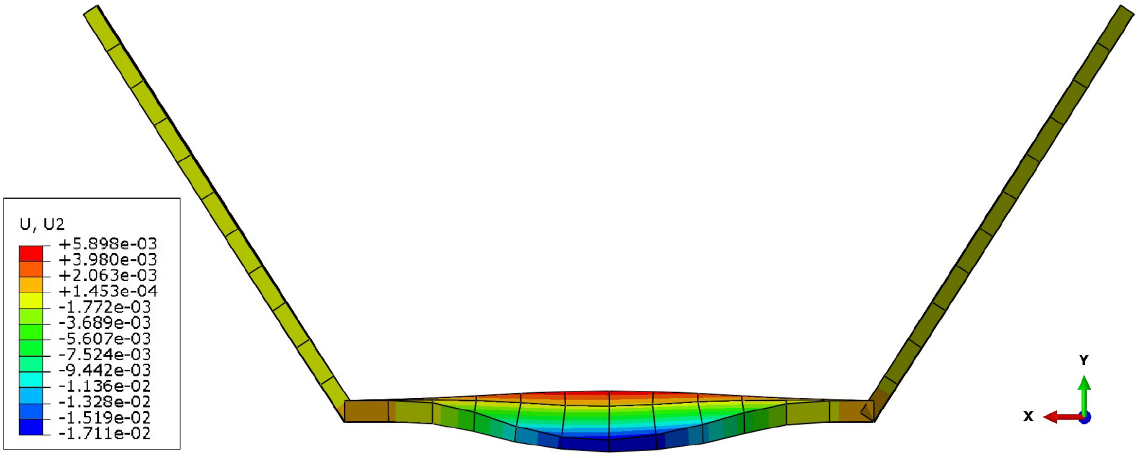

Figure 6.37: Local buckling of the web of the sheet pile toe, seen in the lateral plane, after ten impacts. The displacement in the vertical direction, into the paper, of the middle of the web was approximately 22 mm.

Impact at the corner between the flange and web–eccentric moment of 12 kgm

The first impact occurs at 0.105 s, and the obstacle is located at a depth corresponding to 60 mm, in Figure 6.38.

Figure 6.39 shows that the acceleration amplitudes are approximately 25g, for both upwards and downwards motion. After impacts the acceleration amplitudes are approximately 32g for upwards motion, while being lower for each following impact. For downwards motion the acceleration amplitudes are approximately 28g, when disregarding potential data deviations. This is an increase of 28% in upwards acceleration, and an increase of 12% in downwards acceleration. Furthermore, the Fast Fourier Transformations in Figure 6.40 shows an increase in acceleration amplitude from 21g to 30g, at the driving frequency of 41 Hz, after the first impact. This is a 42% increase.

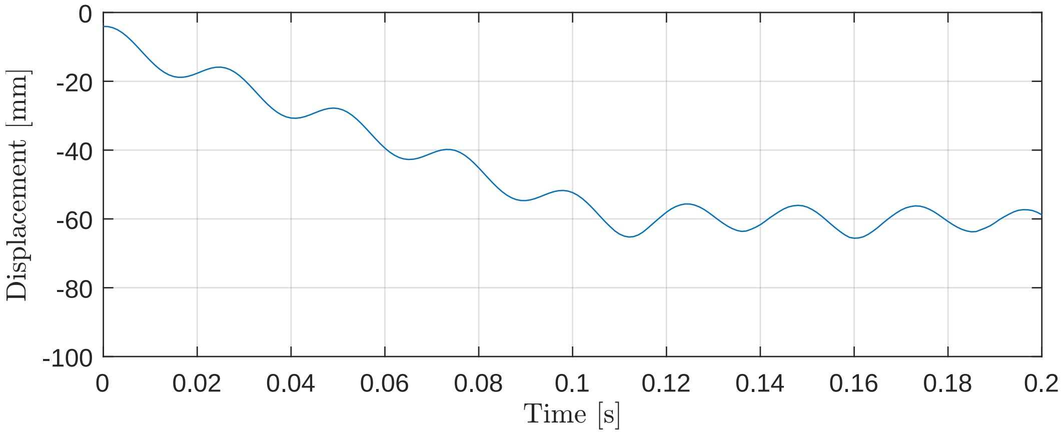

Figure 6.38: Displacement at a penetration depth of ten metres, versus time, one-metre below the sheet pile-head, before and after impacts.

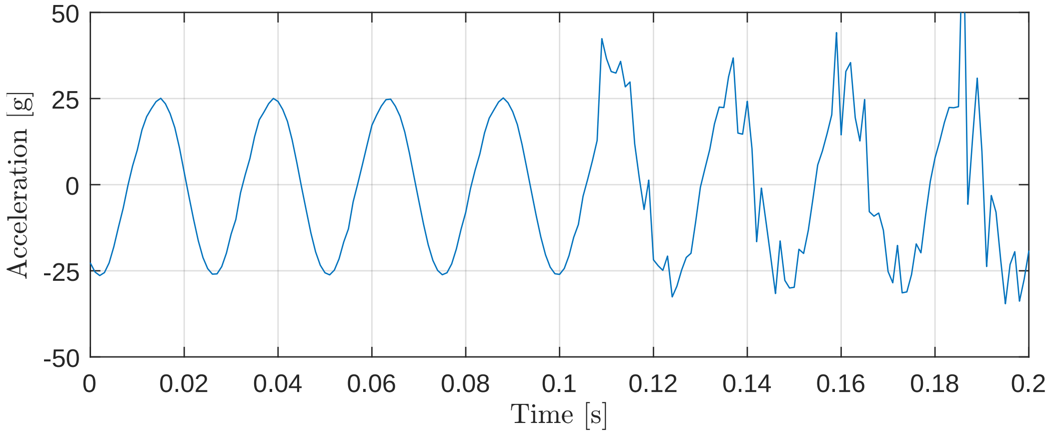

Figure 6.39: Acceleration at a penetration depth of ten metres, versus time, one-metre below the sheet pile-head, before and after impacts.

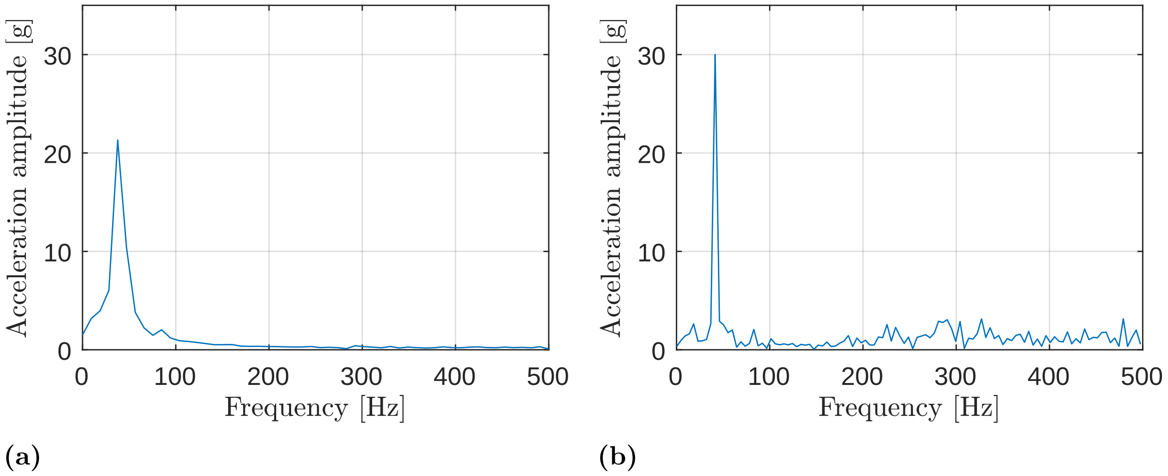

Figure 6.40: (a) Fast Fourier Transformation of the accelerations in Figure 6.39 before an impact. (b) Fast Fourier Transformation of the accelerations in Figure 6.39 after impacts.

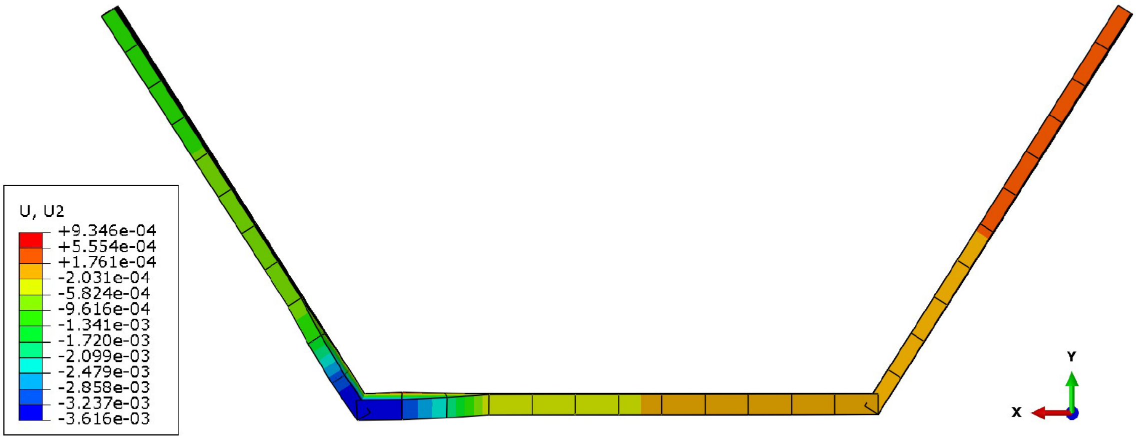

Figure 6.41: Local buckling of the corner between the flange and the web of the sheet pile toe, seen in the lateral plane, after ten impacts. The displacement in the vertical direction, into the paper, of the corner between the flange and the web was approximately 8 mm.

Impact at the edge of the flange–eccentric moment of 12 kgm

The first impact occurs at 0.105 s, and the obstacle is located at a depth corresponding to 60 mm, in Figure 6.42.

Figure 6.43 shows that the acceleration amplitudes are approximately 25g before impact, for both upwards and downwards motion. After impacts the acceleration amplitudes are approximately 25g, for both upwards and downwards motion, when disregarding potential data deviations. Furthermore, the Fast Fourier Transformations in Figure 6.44 shows an increase in acceleration amplitude from 21g to 27g, at the driving frequency of 41Hz, after the first impact. This is a 28% increase.

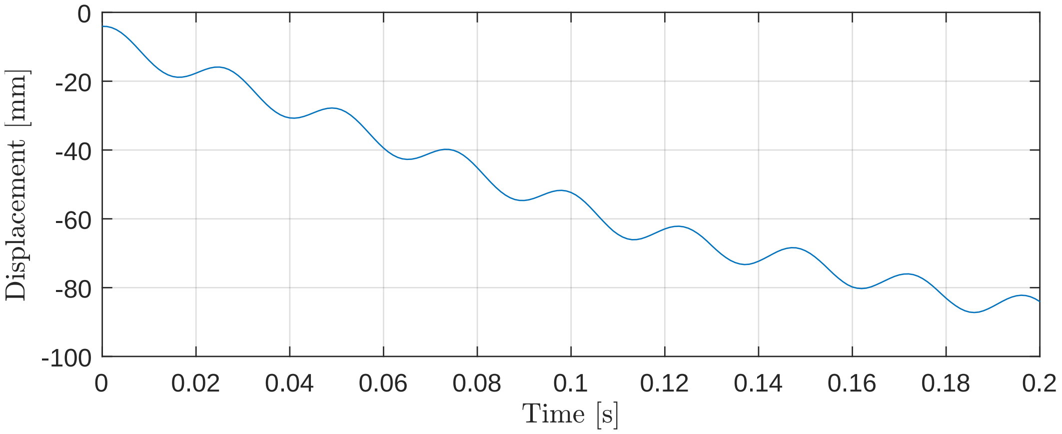

Figure 6.42: Displacement at a penetration depth of ten metres, versus time, one-metre below the sheet pile-head, before and after impacts.

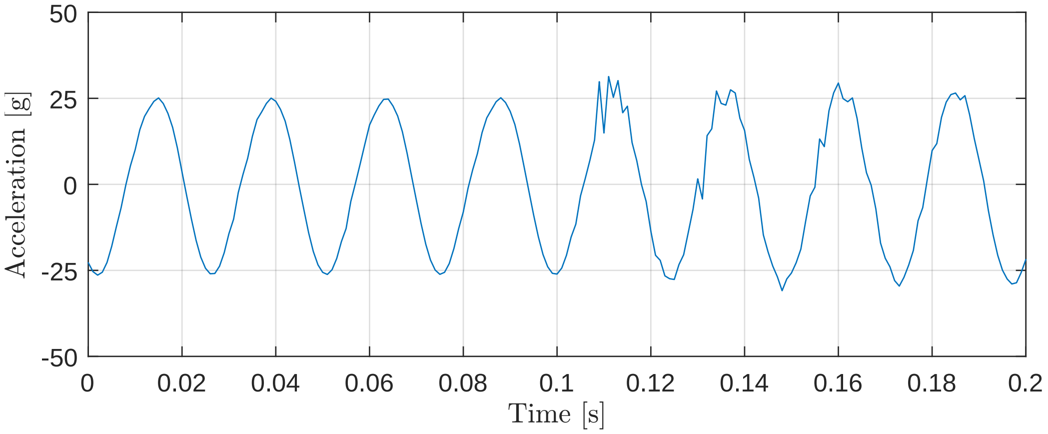

Figure 6.43: Acceleration at a penetration depth of ten metres, versus time, one-metre below the sheet pile-head, before and after impacts.

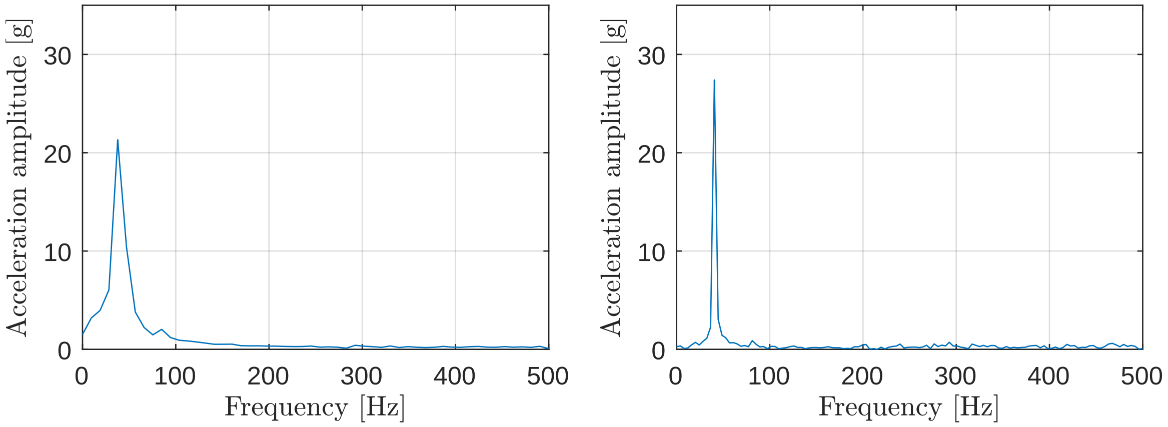

(a) **(b)**

Figure 6.44: (a) Fast Fourier Transformation of the accelerations in Figure 6.43 before an impact. (b) Fast Fourier Transformation of the accelerations in Figure 6.43 after impacts.

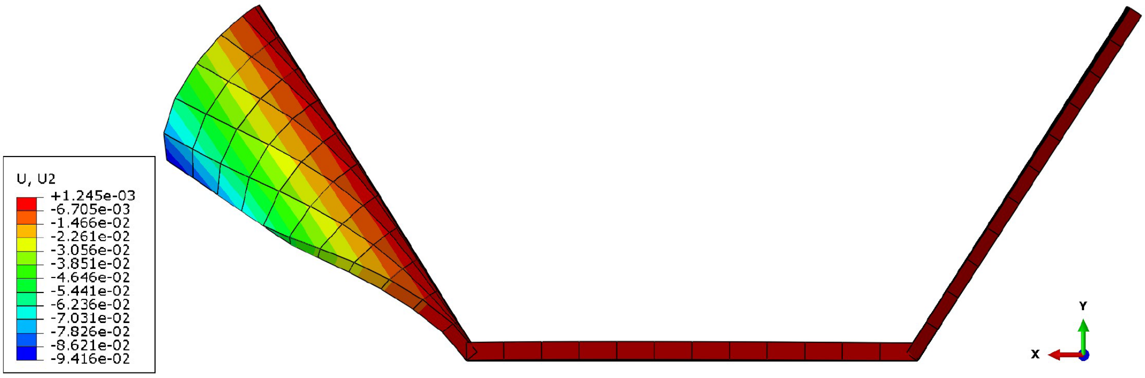

Figure 6.45: Local buckling of the flange of the sheet pile toe, seen in the lateral plane, after ten impacts. The displacement in the vertical direction, into the paper, of the flange was approximately 125 mm.

6.6 Analysis

In this section, the selected Finite Element results are being discussed and analysed. Firstly, the quasi-static buckling results are examined, followed by the vibratory driving results and the impact results. Finally, errors, limitations, and potential improvements of the FE model are being discussed.

Quasi-static buckling

The results from the quasi-static simulations seem to be realistic. The corner between the flange and the web is the stiffest, with the middle of the web, and the edge of the flange being less stiff, in that order, as would be expected. The buckling behaviours seem to behave non-linearly, as both elastic and plastic material behaviour occur during the whole of the buckling processes. Even when the contact force is low, a small portion of the contact area reaches plasticity, making the whole of the processes behave plastic. This changes the loading and unloading stiffnesses, as well, making linearisation of the buckling behaviours complex. The change in stiffness during the simulations is probably a result of the current deformed shape of the cross-section being more, or less, stiff. When the contact force versus vertical displacement plots starts to plateau, extrusion buckling is initiated, which would cause problems during physical vibratory driving. Figure 6.9, that shows the buckling behaviour of the corner between the flange and the web during an impact simulation, indicates that extrusion buckling could be reached rather quickly during regular vibratory driving. The figure is also similar to Figure 6.10, that shows the quasi-static buckling behaviour of the corner between the flange and the web, meaning that quasi-static simulations probably are a reasonable method of predicting impact buckling behaviour.

Vibratory driving

Generally, the vibratory driving results shows good resemblance with the reference case results. Driving at two, six, and ten metres penetration depths gave global penetration speeds of 110 mm/s, 145 mm/s, and 150 mm/s, respectively, compared to the 80 mm/s, 120 mm/s, and 130 mm/s of the reference case at those penetration depths. This is a 37.5%, 21%, and 15% difference, respectively, at those three penetration depths. The difference in global penetration speed ensues mainly from the difference in downwards displacement. The reason for this difference is thought to be both that the leader force was calibrated towards the uniaxial MDOF model rather than the FE model, and that the toe resistance was omitted in the FE model. Inclusion of the toe resistance is predicted to have given more accurate global penetration speeds, as the general displacement behaviour of the model is similar to the reference case. Furthermore, the accelerations from the simulations show good resemblance to the reference case, as well. Near the sheet pile-head, the acceleration at all three penetration depths, show the same magnitude as the reference case downward acceleration while the upward accelerations generally are slightly lower than in the reference case. At the sheet pile toe, the accelerations from the model seem to be of the same magnitude as in the reference case in the upward direction while the downward accelerations are slightly higher than in the reference case. The pile toe accelerations, additionally, seem to be influenced by other frequencies than the driving frequency. This is theorised to be the effect of internal vibrations in the sheet pile. A more realistic damping in the model, from the surrounding soil, and within the sheet pile, would probably have dampened out the high amplitudes, and reduced the influence of other frequencies. This could potentially have been achieved if the soil resistance would have been applied in each node, rather than in intervals, which might would have hindered the nodes within the sheet pile from oscillating. The reason for the accelerations near the sheet pile-head to be more uniform, is thought to be the effect of being close to the applied vibratory forces, which increases the influence the vibratory driving has on the nodes.

Impacts at the web, and at the corner between the flange and the web

Impacts at the middle of the web, and at the corner between the flange and the web, with the eccentric moments of both 6 kgm and 12 kgm, show resembling results. The vertical displacement of the sheet pile stops at around the impact location, and there is a clear distinction in acceleration amplitude, in the acceleration versus time plots, before and after impacts, with a general increase of 30% for upwards acceleration. It is difficult to accurately determine the acceleration change after impacts, as there is an evident influence from high frequencies. It is reasonable to assume that high frequencies will follow an impact. How realistic these frequencies are, is another matter. Presumably, these frequencies would have been dampened out if a more realistic damping would have been applied to the model. With this in mind, the Fast Fourier Transformations seem to give a more distinct indication that an impact has occurred, as they generally gave a higher increase in acceleration amplitude, at the driving frequency, than the acceleration versus time plots. Potentially, the indication that high frequencies start to appear could be a sign of impact, as well. This is, however, difficult to theorise around, as no experimental field study have been found where an impact occurred, which could have either confirmed or denied this theory. The buckling displacement at these impact locations are minor with the lower eccentric moment, both vertically and laterally, and are assumed to be neglectable in a practical scenario. With the higher eccentric moment, however, the buckling displacements at the middle of the web starts to extrude, which might make the sheet pile insufficient if continued vibratory driving had occurred. The corner between the flange and the web seems to be too stiff for any sufficient buckling to happen.

Impacts at the edge of the flange

Impacts at the edge of the flange results in a different behaviour. With an eccentric moments of 6 and 12 kgm, it is problematic to determine when an impact has occurred. With the lower eccentric moment, the vibratory driving of the sheet pile continues after the first impact with a new lesser global penetration speed. With the higher eccentric moment, the vibratory driving of the sheet pile seems to continue after the first impact with the same global penetration speed, as if no impact had occurred. The acceleration versus time plots tells the same story, it is challenging to determine if any impacts have happened at all, as the acceleration amplitudes are approximately the same before and after the impacts. A small number of overtones are present after the first impact, which might be an indication. However, during physical vibratory driving, in realistic soil conditions, overtones are assumed to be more common, with varying intervals of grain sizes and soil layer densities. Therefore, the Fast Fourier Transformations seem to give the best indication that an impact has occurred, where an acceleration amplitude increase of 15% and 28% ensued after the first impact, for the lower and higher eccentric moments, respectively. Those plots indicate, as well, that the influence from other frequencies is minor. The buckling displacements at the edge of the flange is troublesome, for both the lower and higher eccentric moment. Extrusion buckling seem to be initiated for both scenarios. Given enough time, the sheet pile would have been made insufficient by making it impossible to connect another sheet pile to the existing one, while also removing the ground water resistance of the sheet pile wall. The combination of it being difficult to notice these impacts, and the catastrophic effect of them, makes it two ominous scenarios.

General

As mentioned above, the damping in the FE model is probably not realistic. If the soil model, in Section 5.3, would have been made more realistic, and the implementation of it in the FE model had been made more continuous along the sheet pile, better results would probably have been given. The stiffness-proportional damping added, of 1% at the natural frequency of approximately 105Hz, could possibly have been increased to reduce the influence of the non-physical frequencies. Experimental field studies must probably be performed to more accurately capture the damping of the system, because currently the applied damping is just based upon assumptions.

The conducted convergence study could have been performed more thoroughly, as the accelerations were still converging at the chosen element size of the sheet pile. More accurate simulation results would probably have been given with a finer mesh. However, due to time, and computational limitations, a finer mesh of the model would have been unreasonable. The chosen element size did also seem to provide results good enough to prove the usefulness of the model, and to confirm its legitimacy.

As always, human- and computational reliability does not always align, resulting in errors. This could potentially have influenced the established FE model, and its simulated results. Hopefully, it has not had too large of an effect.

A major limitation with the created FE model was that the lateral soil support was modelled with displacement boundary conditions, rather than with a lateral soil behaviour. The consequence of this is that compression waves could be captured with the model, but not bending waves. Potentially, abrupt changes in bending waves could have been a more advantageous indication that an impact had occurred, than abrupt changes in compression waves.

7 Uniaxial MDOF model

A uniaxial Multi-Degree of Freedom (MDOF) model was created to study if the vibratory driving and impact with a boulder could be modelled using a simpler, and faster, model than the FE model. The method used when creating the model is described in Section 7.1, while the simulation method is described in Section 7.2. A convergence study is presented in Section 7.3. A model calibration where the model was tuned against the reference case is presented in Section 7.4. The simulations that were carried out using the MDOF model are described in Section 7.5 while the results of the simulations are shown in Section 7.6. Finally, a discussion of the results is presented in Section 7.7.

7.1 Model

The uniaxial MDOF model was created using springs, masses and sliders, as shown in Figure 7.1. Some simplifications were made compared to the uniaxial model that was described in Section 2.6.4. Firstly, the isolation spring between the bias mass and vibrating mass was omitted, and the bias mass was instead assumed to be represented by a static force, meaning that the isolation was assumed to be perfect. Secondly, the soil resistances were represented using only springs and sliders, i.e., the dashpots were omitted. The reason for this was to use a simpler model that could easily be implemented in the FE model.

The model parameters from Chapter 5 were used when creating the model, relevant parameters are summarised in Table 7.1 for simplicity.

Table 7.1: Model parameters of the sheet pile and vibrator unit.

Parameter	Value	Unit
Sheet pile length, L_p	14	m
Sheet pile cross-section area, A_p	84.98	cm^2
Sheet pile perimeter, Ω_p	170.6	cm
Young's modulus, steel, E_s	210	GPa
Density, steel, ρ_s	7,800	kg/m^3
Driving frequency, f_d	41	Hz
Eccentric moment, M_e	0–12	kgm
Dynamic mass of vibrator unit, m_v	2,450	kg
Bias mass of vibrator unit, m_0	1,020	kg
Leader force, F_l	−140–70	kN

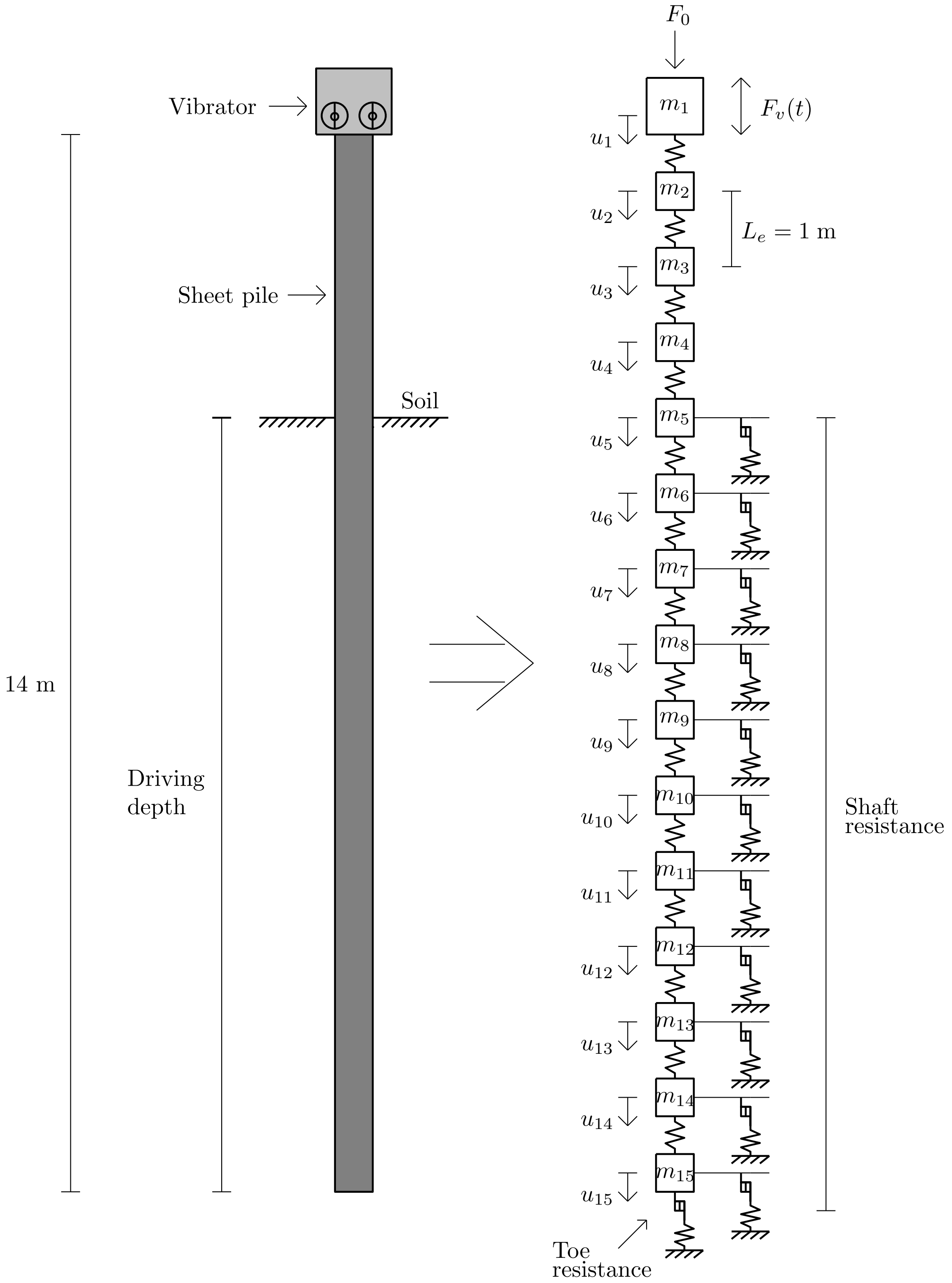

Figure 7.1: Illustration of the uniaxial MDOF model of the sheet pile–vibrator system.

7.1.1 Sheet pile

The sheet pile was modelled using linear spring elements, each with a length L_e of one metre. The element stiffness matrix was calculated as

$$\boldsymbol{K_e} = \frac{E_s \cdot A_p}{L_e} \begin{bmatrix} 1 & -1 \\ -1 & 1 \end{bmatrix} \tag{7.1}$$

and the element mass matrix as

$$\boldsymbol{M_e} = \rho_s \cdot A_p \cdot L_E \begin{bmatrix} 0.5 & 0 \\ 0 & 0.5 \end{bmatrix} \tag{7.2}$$

with the sheet pile area A_p, Young's modulus E_s and density ρ_s from Table 7.1. These matrices were then assembled to global mass and stiffness matrices, $\boldsymbol{M}$ and $\boldsymbol{K}$, representing the model shown in Figure 7.1.

7.1.2 Damping

Material damping for the sheet pile was included in the model by using stiffness proportional Rayleigh damping. The first non-rigid natural frequency was estimated to about 105 Hz by doing an eigenvalue analysis with the assumption that the sheet pile–vibrator system is vibrating freely. The damping was then included in the model using the damping matrix $\boldsymbol{C}$ determined as

$$\boldsymbol{C} = \beta \cdot \boldsymbol{K} \tag{7.3}$$

where $\boldsymbol{K}$ is the global stiffness matrix and β is the stiffness proportional damping constant determined as

$$\beta = \frac{2\zeta}{\omega_n} \tag{7.4}$$

with the damping ratio ζ assumed to 1% and the natural frequency ω_n in rad/s. The main reason for including some damping was to avoid overtones that distorts the acceleration data (although it did not have a large influence on the displacements, velocities, and penetration speed).

7.1.3 Vibrator

The action from the vibrator was modelled using the method described in Section 2.4.1, thus the unbalanced vertical force was modelled as

$$F_v(t) = M_e \cdot \omega^2 \cdot sin(\omega t) \tag{7.5}$$

and the static surcharge force as

$$F_0 = m_0 \cdot g + F_l \tag{7.6}$$

where M_e is the eccentric moment, ω is the driving frequency in rad/s, t is the time, m_0 is the bias mass, and F_l is the leader force. The eccentric moment M_e and leader force F_l were varied in the different analyses. The dynamic mass of the vibrator was included by adding it to the top node in the system (m_1 in Figure 7.1).

7.1.4 Shaft resistance

Shaft resistance was included in the model by adding springs and sliders to each node below the ground level and where the linear soil model for shaft resistance, described in Section 5.3, was used to describe the spring–slider behaviour. A maximum shaft resistance force $R_{s,max}$ was calculated for each slider, based on the dynamic shaft resistance profile τ_d from Section 5.2, as

$$R_{s,max} = \Omega_p \int_{z-L_e/2}^{z+L_e/2} \tau_d \, dz \tag{7.7}$$

where z is the depth of the node, Ω_p is the sheet pile perimeter and L_e is the sheet pile element length. The limits for each slider were set to $-R_{s,max} \leq R_s \leq R_{s,max}$. The stiffness for each spring was calculated as

$$k_s = \frac{R_{s,max}}{Q_s} \tag{7.8}$$

with the shaft quake $Q_s = 2.5$ mm.

7.1.5 Toe resistance

Toe resistance was included in the model by adding a spring and a slider to the node corresponding to the toe of the sheet pile and where the linear soil model for toe resistance, described in Section 5.3, was used to describe the spring–slider behaviour. A maximum toe resistance force $R_{t,max}$ was calculated for the slider, based on the dynamic toe resistance profile q_d from Section 5.2, as

$$R_{t,max} = A_p \cdot q_d(z) \tag{7.9}$$

where z is the depth of the sheet pile toe and A_p is the sheet pile area. The limits for the slider were set to $0 \leq R_t \leq R_{t,max}$. The stiffness for the spring was calculated as

$$k_t = \frac{R_{t,max}}{Q_t} \tag{7.10}$$

with the toe quake $Q_t = 2.8$ mm.

7.1.6 Impact with boulder

Impact with a boulder was modelled by changing the behaviour of the toe resistance spring so that it corresponded to the impact behaviours observed in the FE model, where quasi-static simulations of the sheet pile buckling behaviour were performed. The method used to determine the behaviour is described in detail in Section 6.4.1.

The purpose of modelling the impact was to study if the MDOF model would produce results that correspond well to the FE model. With regard to this, it was decided that it was sufficient to study only one of the impacts, and the impact at the center of the web was chosen.

The impact behaviour from the FE model was simplified so that it was easier to implement in the MDOF model. Firstly, a linear loading stiffness and a maximum load were estimated based on the contact force versus displacement curve in Section 6.4.1. Secondly, the unloading stiffness was assumed to be the same as the loading stiffness.

Table 7.2 shows the parameters that were used to model the impact behaviour while the contact force versus displacement curve is shown in Figure 7.2, where the linear approximation is also shown. The impact location is shown in Figure 7.3.

Table 7.2: Parameters describing the impact behaviour.

Parameter	Value	Unit
Loading stiffness	100	MN/m
Unloading stiffness	100	MN/m
Maximum load	300	kN

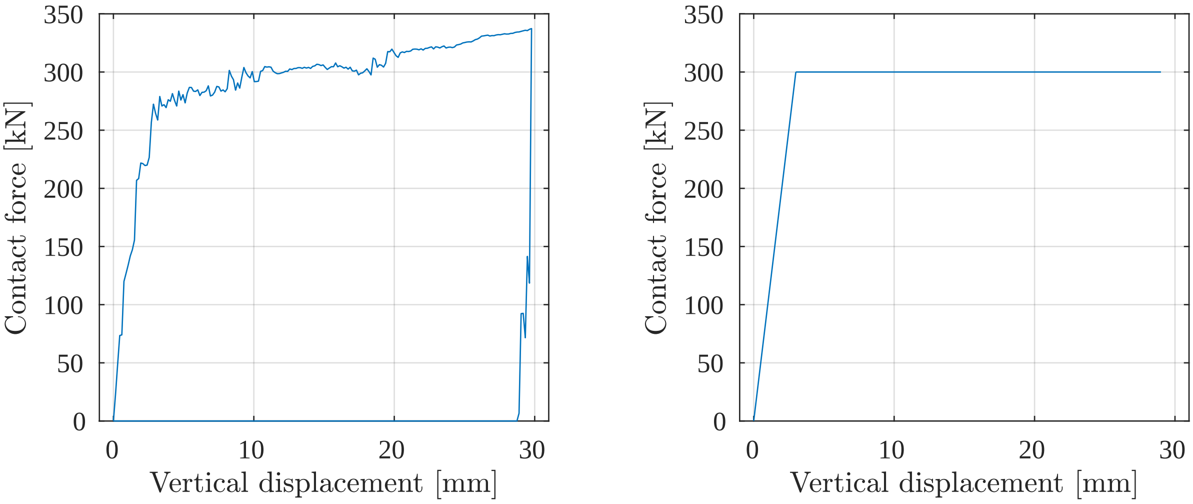

(a) **(b)**

Figure 7.2: (a) Contact force versus displacement for web impact. (b) Linear approximation of contact force versus displacement.

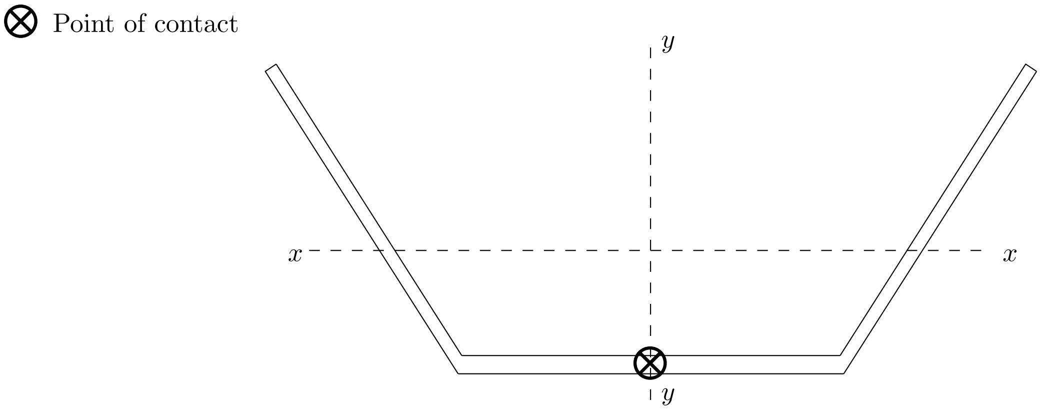

Figure 7.3: Illustration of the impact location simulated.

7.2 Simulation method

The simulations were carried out using the Central Difference Method, where the iteration scheme for MDOF systems, as shown in Section 3.1, were implemented. All initial conditions that were needed to start the iteration scheme was set to zero, however, this should have had no effect on the results as the iterations were continued until it was certain that a steady state had been reached. The time step size was set to five microseconds, which is motivated with the convergence study in Section 7.3.

The MATLAB code that was written to set up the model, and run the simulations is included in Appendix B.1.

7.3 Convergence study

A convergence study was carried out to ensure that a small enough time-step was used in the simulations. The convergence study was done by comparing the peak toe accelerations during steady state for different time steps (for normal driving without impact). The input parameters in Table 7.3 was used in the convergence study. The peak toe acceleration as a function of the time step size is shown in Figure 7.4, from which it was concluded that a time step size of five microseconds was sufficient.

Table 7.3: Parameters used in the convergence study.

Parameter	Value	Unit
Penetration depth	10	m
Eccentric moment, M_e	6	kgm
Leader force, F_l	0	kN

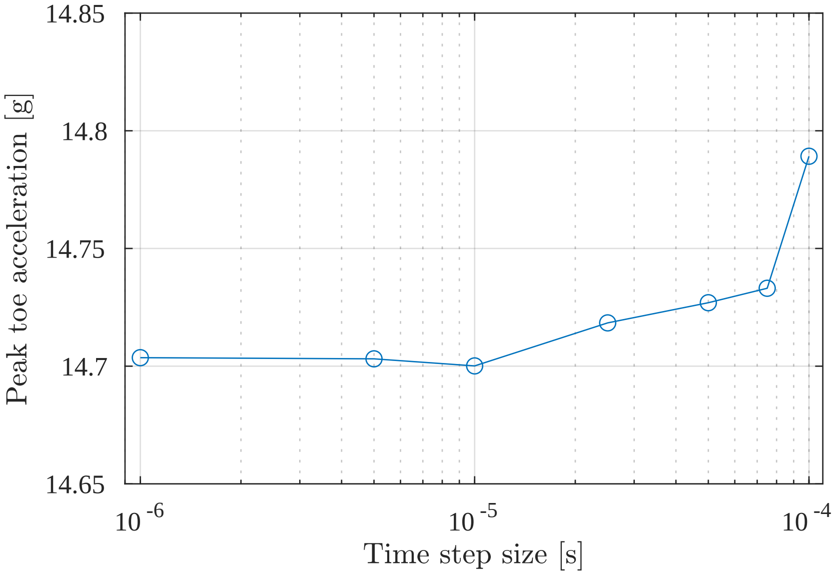

Figure 7.4: Convergence study for the time step size. Peak toe acceleration as a function of the time step size.

7.4 Model calibration

A model calibration was carried out to try to fit the model to the experimental results from the reference case. The two quantities that were unknown from the reference case were the setting of the eccentric moment and the additional driving force from the leader. As stated previously, Viking [2] assumed the eccentric moment to 6 kgm when evaluating the results in the reference case and it was therefore concluded that the eccentric moment should be set to 6 kgm in the model. The calibration then consisted of calibrating the leader force so that the model produced results that correspond to the reference case. Here it was decided that it was most beneficial to calibrate the leader force such that the model produced penetration speeds that corresponded well to the reference case.

By assuming that the leader force varies with the penetration depth according to Figure 7.5b, the model produces penetration speeds that varies with the penetration depth according to Figure 7.5a, which is fairly close to the penetration speeds from the reference case. It can be seen in Figure 7.5b that the leader force increases fairly linearly with the penetration depth. This was assumed to be reasonable as the total shaft resistance more or less increases linearly with the penetration depth and thus the leader force would need to have a similar variation if the target is a constant penetration speed.

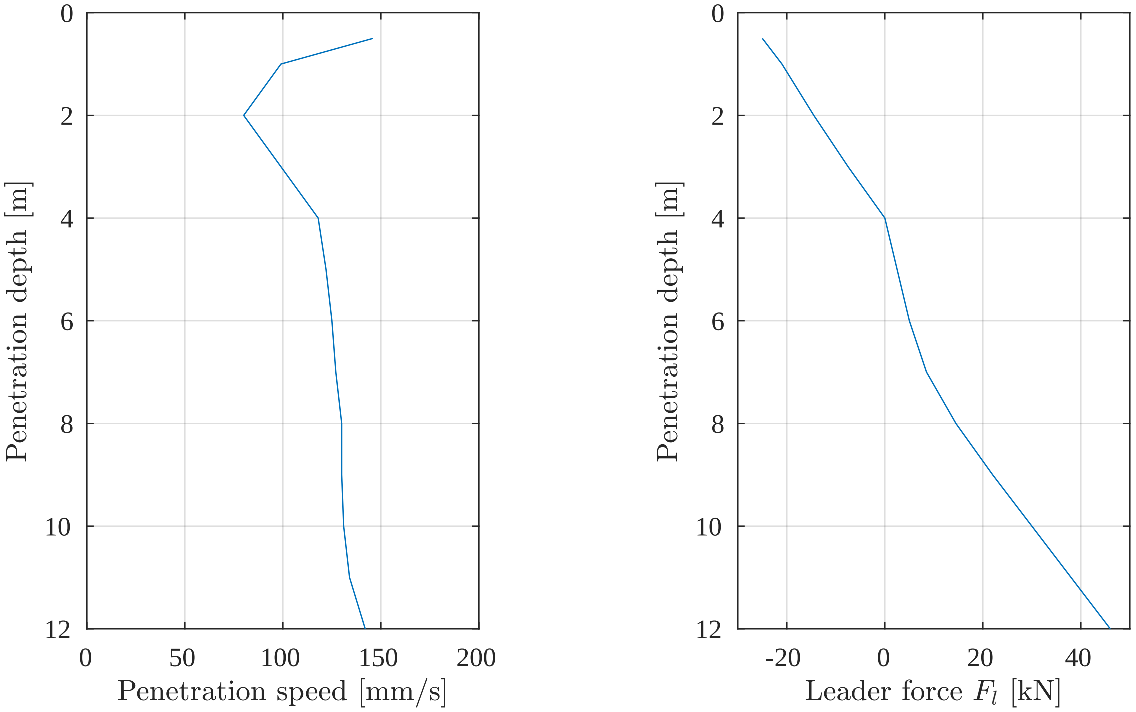

(a) **(b)**

Figure 7.5: (a) Penetration speed as a function of the penetration depth. (b) Leader force as a function of the penetration depth.

7.5 Simulations

The simulations that were carried out with the MDOF model are described in this section, while selected results from the simulations are shown in Section 7.6.

7.5.1 Vibratory driving simulations

Vibratory driving at the penetration depths of two, six, and ten metres were simulated to study if the model produces result that correspond well with the reference case. The simulations were run until it was certain that a steady state had been reached

The parameters used in the three simulations are shown in Table 7.4.

Table 7.4: Input parameters for vibratory driving simulations.

Penetration depth [m]	Eccentric moment M_e [kgm]	Leader force F_l [kN]
10	6	30
6	6	5
2	6	-14.5

7.5.2 Impact simulations

The impact described in Section 7.1.6 was simulated. The penetration depth was assumed to be ten metres, and two different eccentric moments, 6 and 12 kgm, were studied for the impact. The impact simulations were, as previously mentioned, carried out by changing the behaviour of the toe resistance spring so that it corresponded to the contact force versus displacement curve from the FE model. The simulations were carried out by running an ordinary vibratory driving simulation until a steady state had been reached and then changing the behaviour of the toe resistance spring.

The parameters used in the simulations are shown in Table 7.5.

Table 7.5: Input parameters for impact simulations.

Parameter	Value	Unit
Penetration depth	10	m
Eccentric moment, M_e	6 & 12	kgm
Leader force, F_l	30	kN

7.5.3 Parameter study

A parameter study of how the driving frequency effects the vibratory driving was conducted. Driving frequencies in the chosen vibrators range (0–41 Hz) was studied as well as hypothetical frequencies outside of the vibrators range. The parameter study was carried out by running an ordinary vibratory driving simulation (without impact) for each chosen driving frequency. The simulations were run until it was certain that a steady state had been reached.

The parameters used in the parameter study are shown in Table 7.6.

Table 7.6: Input parameters for parameter study.

Parameter	Value	Unit
Driving frequency, f_d	15–120	Hz
Penetration depth	10	m
Eccentric moment, M_e	6	kgm
Leader force, F_l	30	kN

7.6 Results

Selected results from the simulations are presented in this section. Some brief comments on the results are also provided while a more in-depth discussion of the results is provided in Section 7.7. Note that the positive direction is downwards, e.g., a positive displacement corresponds to a downward displacement.

7.6.1 Vibratory driving simulations

Selected results from the vibratory driving simulations at two, six and ten metres penetration depth are presented in this section. The results were taken at a time when a steady state had been reached.

Vibratory driving at two metres depth

Figures 7.6–7.8 show displacement and accelerations for a penetration depth of two metres.

Figure 7.6 shows the displacement one metre below the sheet pile-head. The upward displacement amplitude is approximately 3 mm while the downward displacement amplitude is approximately 5 mm. The penetration speed is about 79 mm/s. The results from the reference case at two metres depth show an upward displacement amplitude of about 3 mm, a downward displacement amplitude of about 5 mm and a penetration speed of about 80 mm/s.

Figures 7.7 and 7.8 show the acceleration one metre below the sheet pile-head and at the sheet pile toe, respectively. The acceleration one metre below the sheet pile-head varies between 13.5g in the upward direction and 14g in the downward direction. The acceleration at the sheet pile toe varies between 18g in the upward direction and 14.5g in the downward direction. The results from the reference case at two metres depth show accelerations at the sheet pile toe varying between 15g in the upward direction and 11g in the downward direction.

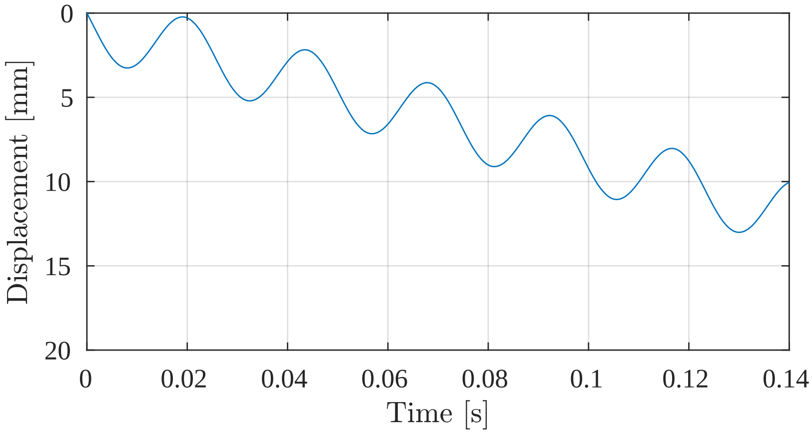

Figure 7.6: Displacement of sheet pile, 1 m below the sheet pile-head, versus time for 2 m penetration depth.

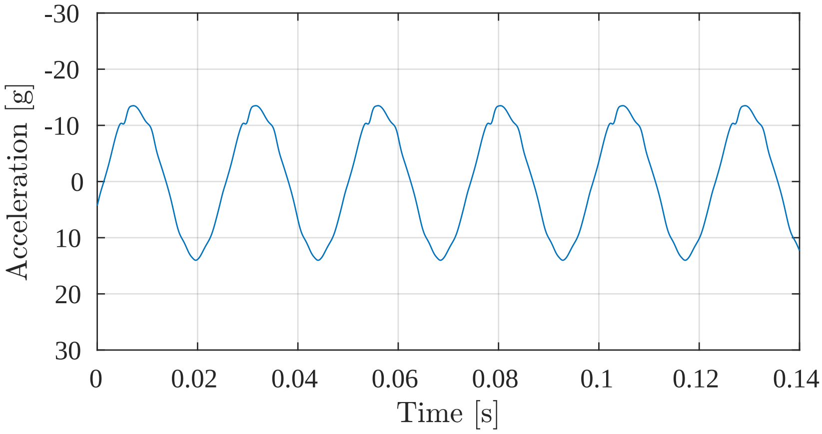

Figure 7.7: Acceleration of sheet pile, 1 m below the sheet pile-head, versus time for 2 m penetration depth.

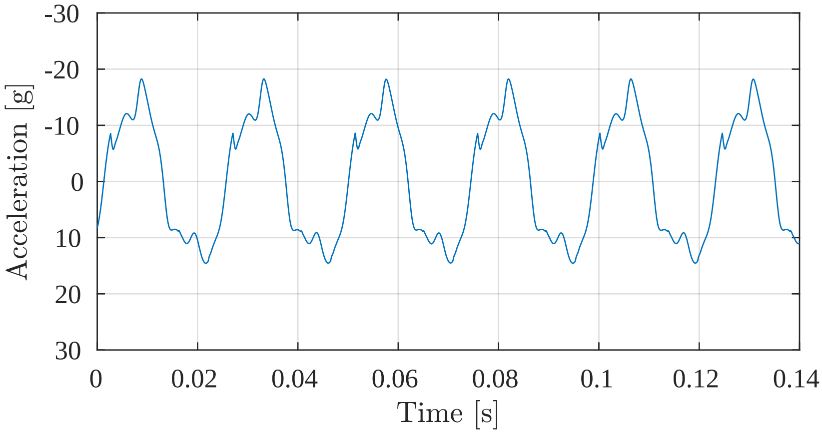

Figure 7.8: Acceleration of sheet pile toe versus time for 2 m penetration depth.

Vibratory driving at six metres depth

Figures 7.9–7.11 show displacement and accelerations for a penetration depth of six metres.

Figure 7.9 shows the displacement one metre below the sheet pile-head. The upward displacement amplitude is approximately 2.6 mm while the downward displacement amplitude is approximately 5.7 mm. The penetration speed is about 124 mm/s. The results from the reference case at six metres depth show a upward displacement amplitude of about 2.5 mm, a downward displacement amplitude of about 5 mm and a penetration speed of about 120 mm/s.

Figures 7.10 and 7.11 show the acceleration one metre below the sheet pile-head and at the sheet pile toe, respectively. The acceleration one metre below the sheet pile-head varies between 13g in the upward direction and 14g in the downward direction. The acceleration at the sheet pile toe varies between 19g in the upward direction and 16g in the downward direction. The results from the reference case at six metres depth show accelerations at the sheet pile toe varying between 18g in the upward direction and 12g in the downward direction.

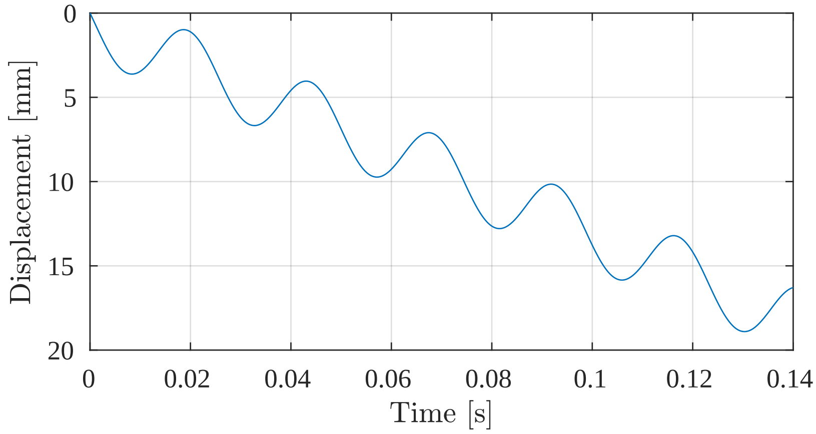

Figure 7.9: Displacement of sheet pile, 1 m below the sheet pile-head, versus time for 6 m penetration depth.

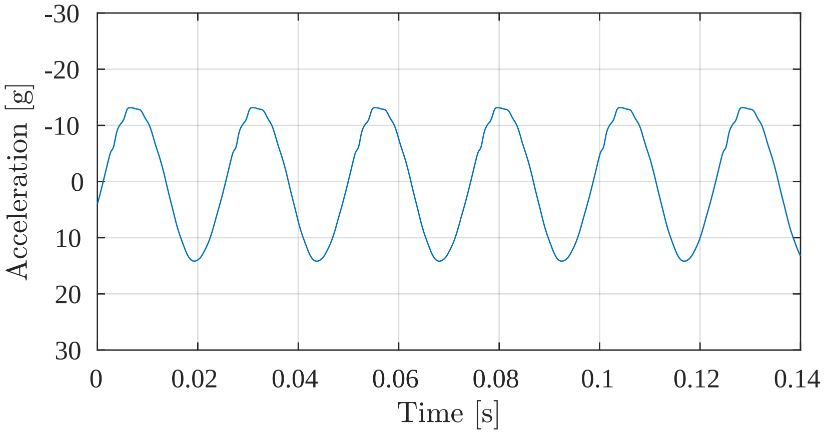

Figure 7.10: Acceleration of sheet pile, 1 m below the sheet pile-head, versus time for 6 m penetration depth.

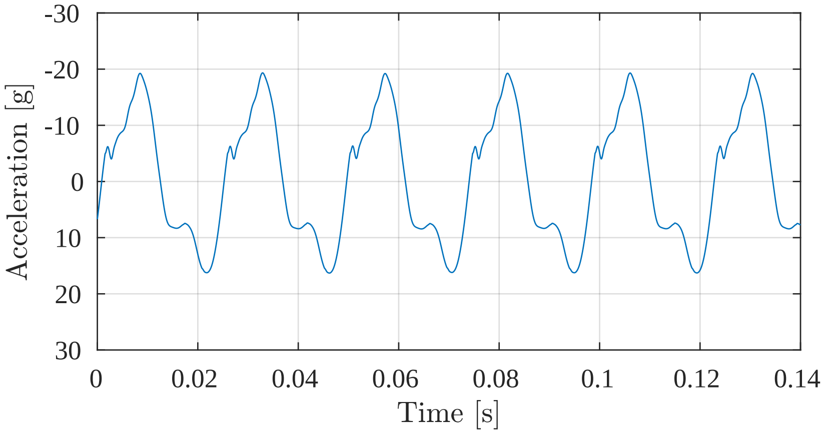

Figure 7.11: Acceleration of sheet pile toe versus time for 6 m penetration depth.

Vibratory driving at ten metres depth

Figures 7.12–7.14 show displacement and accelerations for a penetration depth of ten metres.

Figure 7.12 shows the displacement one metre below the sheet pile-head. The upward displacement amplitude is approximately 2.9 mm while the downward displacement amplitude is approximately 6.1 mm. The penetration speed is about 129 mm/s. The results from the reference case at ten metres penetration depth show a upward displacement amplitude of about 2.5 mm, a downward displacement amplitude of about 5 mm and a penetration speed of about 130 mm/s.

Figures 7.13 and 7.14 show the acceleration one metre below the sheet pile-head and at the sheet pile toe, respectively. The acceleration one metre below the sheet pile-head varies between 14.5g in the upward direction and 15.5g in the downward direction. The acceleration at the sheet pile toe varies between 21.5g in the upward direction and 18.5g in the downward direction. The results from the reference case at six metres penetration depth show accelerations at the sheet pile toe varying between 15g in the upward direction and 12g in the downward direction.

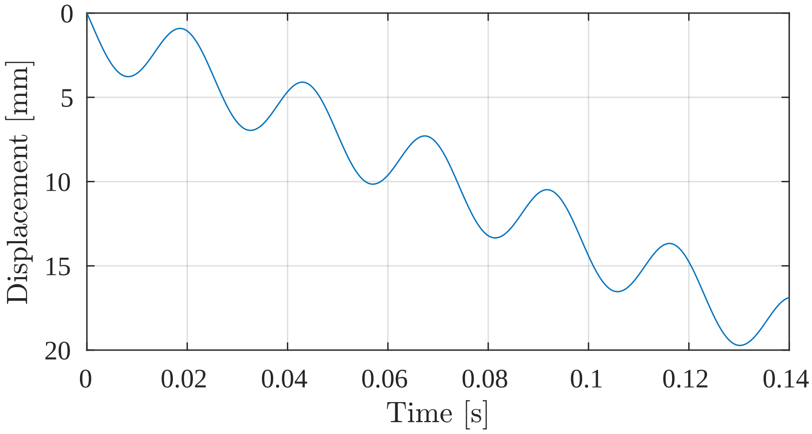

Figure 7.12: Displacement of sheet pile, 1 m below the sheet pile-head, versus time for 10 m penetration depth.

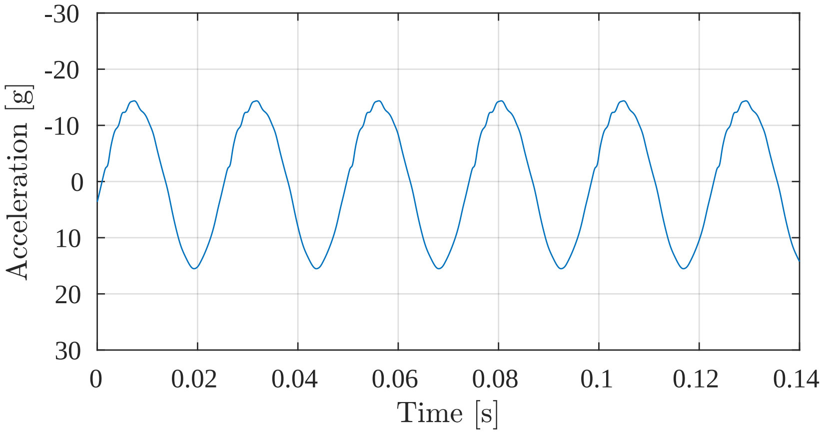

Figure 7.13: Acceleration of sheet pile, 1 m below the sheet pile-head, versus time for 10 m penetration depth.

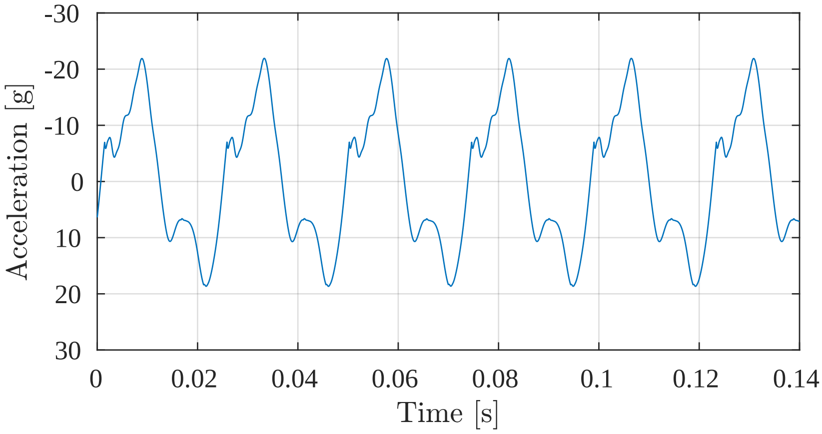

Figure 7.14: Acceleration of sheet pile toe versus time for 10 m penetration depth.

7.6.2 Impact simulations

Selected results from the impact simulations with eccentric moments of 6 and 12 kgm are presented in this section.

Impact–eccentric moment of 6 kgm

Figures 7.15 and 7.16 show displacement and acceleration, one metre below the sheet pile-head, before and after impact with an eccentric moment of 6 kgm. Figure 7.17 shows Fast Fourier Transformations (FFTs) of the acceleration before and after impact. The first contact occurs at about $t = 0.107$ s.

Figure 7.15 shows that the penetration speed is approximately 129 mm/s before the impact and 0 mm/s after the impact. Figure 7.16 shows that the acceleration varies between 14.5g in the upward direction and 15.5g in the downward direction before the impact, which corresponds to a peak-to-peak amplitude of 30g. The acceleration varies between 21g in the upward direction and 18g in the downward direction after the impact, which corresponds to a peak-to-peak amplitude of 39g. Thus, the impact results in a 45% increase in upward acceleration, a 16% increase in downward acceleration and a 30% increase in peak-to-peak amplitude.

Figure 7.17 shows an acceleration amplitude of 14.5g at 41 Hz before the impact and an acceleration amplitude of 18.5g at 41 Hz after the impact. Thus, the impact results in a 28% increase in acceleration amplitude at 41 Hz. Some influence of frequencies between 0–41 Hz can be seen both before and after the impact. There is also a slight influence from higher frequencies after the impact, where an acceleration amplitude of 1.4g at 80 Hz is the most apparent.

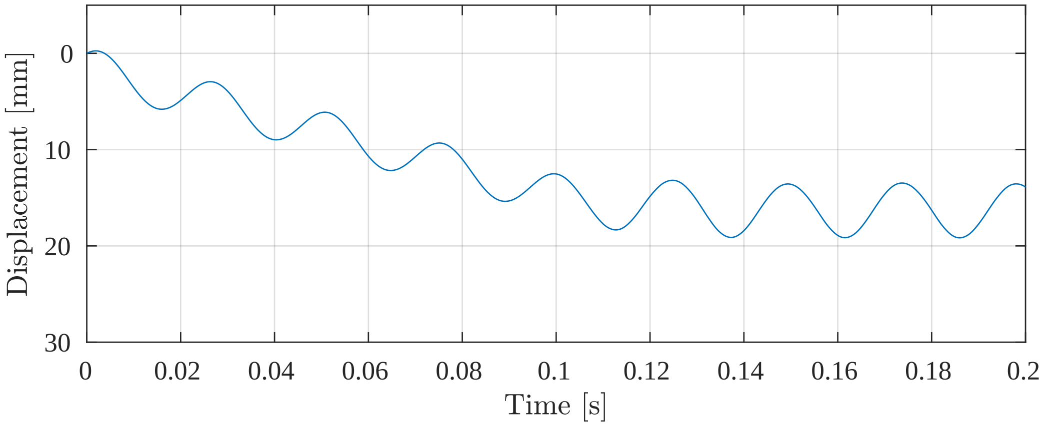

Figure 7.15: Displacement of sheet pile, 1 m below the sheet pile-head, versus time for for an eccentric moment of 6 kgm.

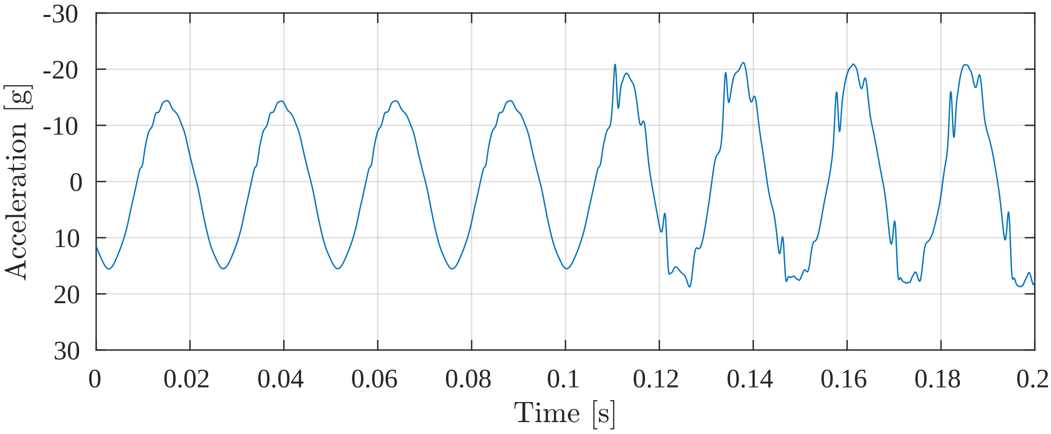

Figure 7.16: Acceleration of sheet pile, 1 m below the sheet pile-head, versus time for an eccentric moment of 6 kgm.

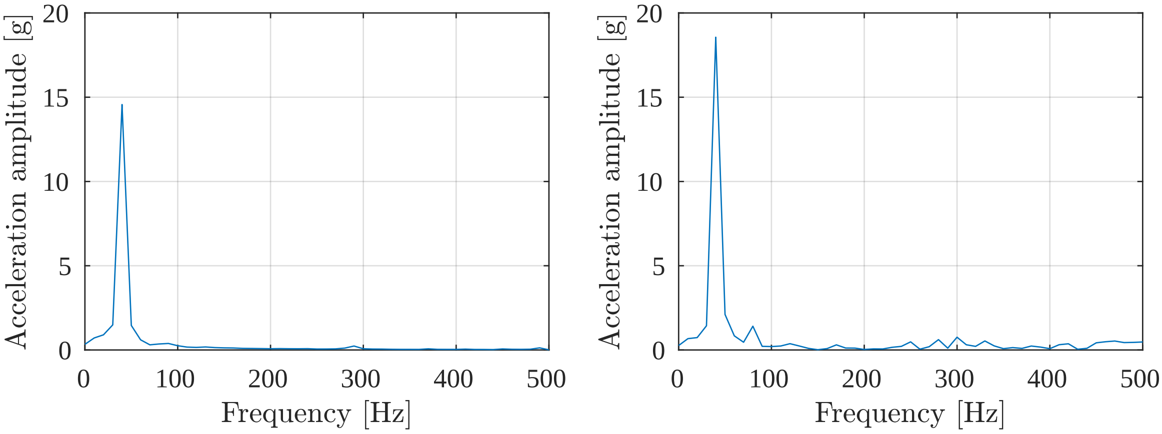

(a) **(b)**

Figure 7.17: FFT of sheet pile acceleration. (a) Before impact. (b) After impact.

Impact–eccentric moment of 12 kgm

Figures 7.18 and 7.19 show displacement and acceleration, one metre below the sheet pile-head, before and after impact for an eccentric moment of 12 kgm. Figure 7.20 shows FFTs of the acceleration before and after impact. The first contact occurs at about $t = 0.108$ s.

Figure 7.18 shows that the penetration speed before the impact is approximately 470 mm/s and 0 mm/s after the impact. Figure 7.19 shows that the acceleration varies between 25.5g in the upward direction and 27g in the downward direction before the impact, which corresponds to a peak-to-peak amplitude of 52.5g. The acceleration varies between 38g in the upward direction and 30g in the downward direction after the impact, which corresponds to a peak-to-peak amplitude of 68g. Thus, the impact results in a 49% increase in upward acceleration, a 11% increase in downward acceleration and a 30% increase in peak-to-peak amplitude.

Figure 7.20 shows an acceleration amplitude of 26g at 41 Hz before the impact and an acceleration amplitude of 31.5g at 41 Hz after the impact. Thus, the impact results in a 21% increase in acceleration amplitude at 41 Hz. Some influence of frequencies between 0–41 Hz can be seen both before and after the impact. There is also a slight influence from higher frequencies after the impact, where an acceleration amplitude of 2.7g at 80 Hz is the most apparent.

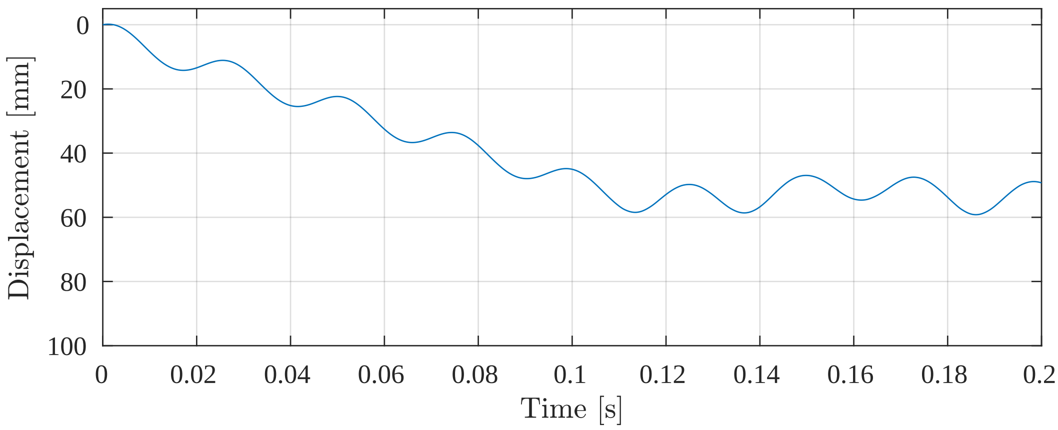

Figure 7.18: Displacement of sheet pile, 1 m below the sheet pile-head, versus time for for an eccentric moment of 12 kgm.

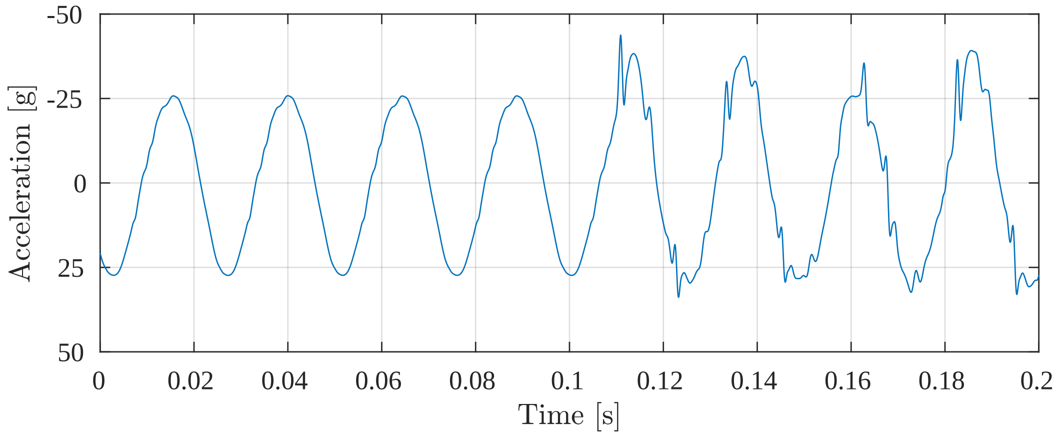

Figure 7.19: Acceleration of sheet pile, 1 m below the sheet pile-head, versus time for an eccentric moment of 12 kgm.

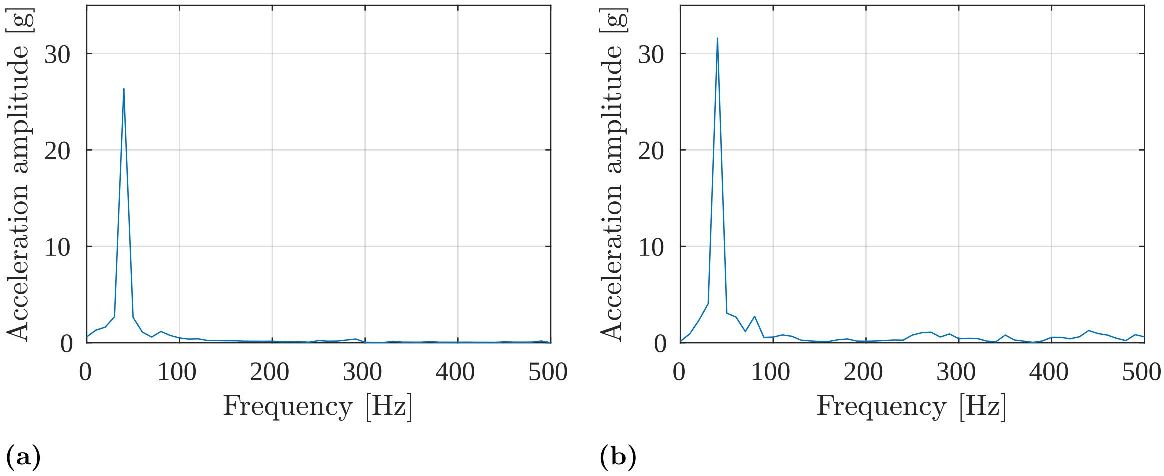

(a)

(b)

Figure 7.20: FFT of sheet pile acceleration. (a) Before impact. (b) After impact.

7.6.3 Parameter study

Selected results from the parameter study, where the driving frequency was varied between 15–120 Hz, are shown in this section. The results were taken at a time when a steady state had been reached.

Figure 7.21 shows the penetration speed, one metre below the sheet pile-head, as a function of the driving frequency. Figure 7.21a shows that a (hypothetical) peak penetration speed of about 11,000 mm/s occur at a driving frequency of 105 Hz. Figure 7.21b shows that the penetration speed varies between 105–155 mm/s for driving frequencies between 15–41 Hz, with a peak of 155 mm/s at a driving frequency of 37 Hz.

Figure 7.22 shows the peak acceleration, one metre below the sheet pile-head, as a function of the driving frequency. Figure 7.22a shows that a peak acceleration of 364g occurs at a driving frequency of 105 Hz. Figure 7.22b shows that the peak acceleration varies rather linearly from 5–15.5g, for driving frequencies between 15–41 Hz.

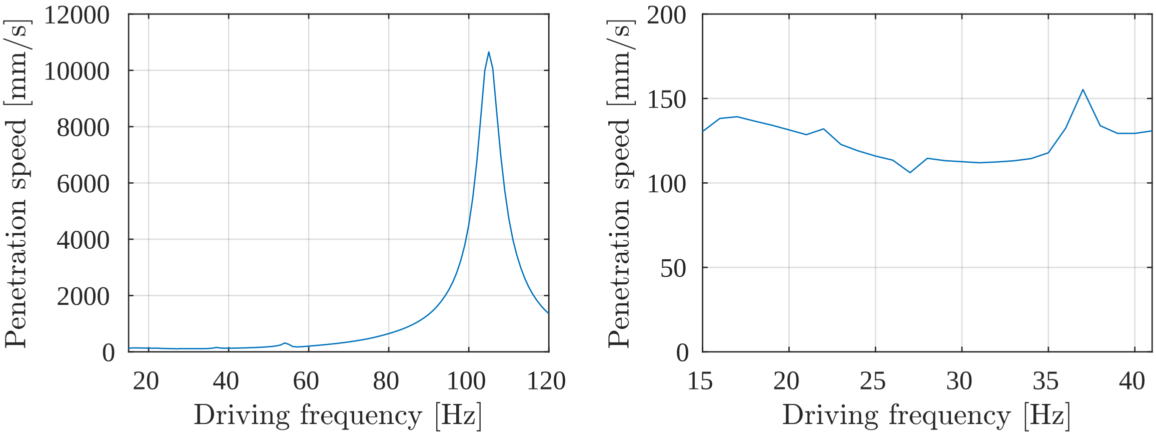

(a) **(b)**

Figure 7.21: Penetration speed versus driving frequency. (a) 15–120 Hz. (b) 15–41 Hz.

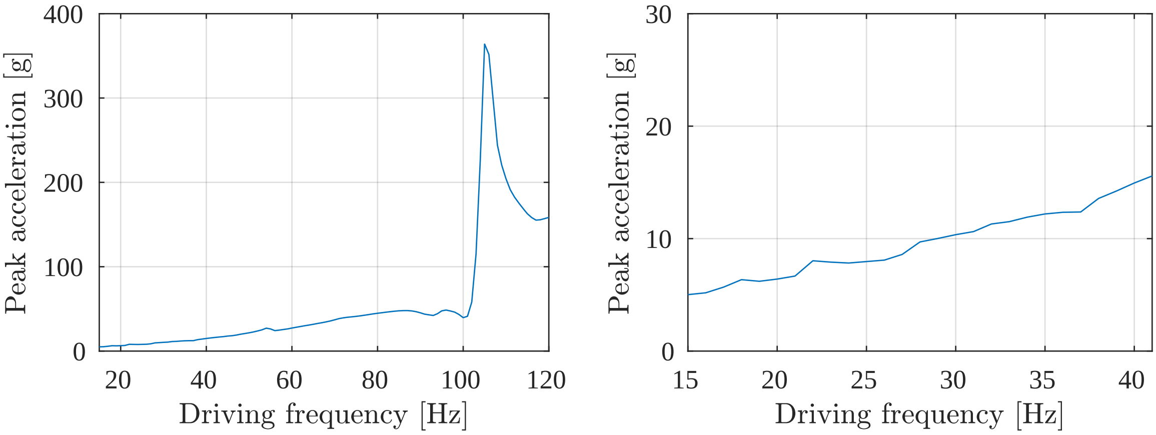

(a) **(b)**

Figure 7.22: Peak acceleration versus driving frequency. (a) 15–120 Hz. (b) 15–41 Hz.

7.7 Analysis

A discussion of the results in Section 7.6 are presented in this section, and comments on the model calibration in Section 7.4 are also provided.

Model calibration

The model calibration was carried out mainly because there was no information regarding the setting of the leader force in the reference case. As a result of this, the variation of the leader force with the penetration depth was estimated so that the penetration speeds in the model corresponded to the ones observed in the reference case. The result of the calibration is a leader force that increases approximately linearly with the penetration depth. This does not appear to be unreasonable considering that the shaft resistance increases more or less linearly with the penetration depth. However, due to the lack of information regarding the setting of the leader force in the reference case, there is no obvious method to verify if the estimated leader force variation is actually accurate.

Vibratory driving simulations

The model produced penetration speeds that are approximately identical to the reference case, which was expected since that was the target of the model calibration. The small deviations in the penetration speeds can be attributed to that the model calibration was carried out in an approximate manner, without any fine-tuning.

The displacement amplitudes produced by the model correspond rather well to the reference case. The general shape of the displacement curves corresponds well to the reference case. However, some deviations can be seen. The model produced upward and downward displacement amplitudes that are slightly higher than in the reference case. The maximum deviation in displacement amplitude is at ten metres penetration depth, where the model produced a downward displacement amplitude (6.1 mm) that is about 22% higher than the corresponding downward displacement amplitude in the reference case (5 mm). A part of the deviations can probably be attributed to human errors when estimating the displacement amplitudes from the plots in the reference case.

The accelerations produced by the model correspond fairly well to the reference case, although there are some deviations. The toe accelerations produced by the model are higher in both the upward and downward direction. The shapes of the toe acceleration curves are also different than in the reference case, where more overtones seems to be present in the toe accelerations produced by the model. The maximum deviation in toe acceleration amplitude is at ten metres penetration depth, where the model produced a downward acceleration amplitude (18.5g) that is about 54% higher than the corresponding downward acceleration amplitude in the reference case (12g).

There were unfortunately no data for the head accelerations in the reference case, but for the sake of comparison it is assumed that the head accelerations in the reference case would have been approximately the same as the toe accelerations. The head accelerations produced by the model are generally lower than in the reference case in the upward direction and higher than in the reference case in the downward direction. The shape of the head acceleration curves corresponds rather well to the curves in the reference case. The maximum deviation in head acceleration amplitude is at six metres penetration depth, where the model produced a upward acceleration amplitude (13g) that is about 28% lower than the corresponding upward acceleration amplitude in the reference case (18g).

The deviations in the accelerations in general, and the toe accelerations in particular, might indicate that there is not enough damping in the model, causing the sheet pile (springs) to oscillate in higher frequencies than the driving frequency. The fact that the shaft resistance is added at discrete points in the model rather than as a continuous friction might also contribute to these oscillations. A part of the deviations in the accelerations can probably also be attributed to errors when estimating the acceleration amplitudes from the plots in the reference case.

Impact simulations

The impact simulations show that the penetration speed goes to zero almost instantly when the impact occurs, which indicates that the relatively simple impact model works fairly well. The acceleration amplitude in both upward and downward direction increases after impact, where there generally is a higher increase in upward acceleration than in downward acceleration and were the increase in peak-to-peak acceleration were 30% for both studied eccentric moments. Some noise in the accelerations can also be seen after the impacts. The FFTs of the accelerations indicates that the impacts result in a 20–30% increase in acceleration amplitude at the driving frequency of 41 Hz. The FFTs also show that there are some minor influences from higher frequencies after the impact.

Parameter study

The parameter study indicates that the driving frequency only has a slight influence on the penetration speed and acceleration in the frequency range of 15–41 Hz, which is a fairly representative frequency range for today's vibratory units. For the penetration speed there seems to be an optimum frequency at about 37 Hz for the considered case, but more studies with different penetration depths, eccentric moments etc. would need to be conducted to confirm this. The parameter study also indicates that there is resonance at the hypothetical driving frequency of 105 Hz. This was not unexpected considering that the first non-rigid natural frequency had previously been estimated to 105 Hz through an eigenvalue analysis.

8 SDOF model

A Single-Degree of Freedom (SDOF) model was created with the purpose of studying if a simpler and faster model than the MDOF model could be used to simulate vibratory driving and an event where a sheet pile encounters a boulder during vibratory driving. The method used when creating the model is described in Section 8.1, while the simulation method is described in Section 8.2. A convergence study is presented in Section 8.3. The simulations that were carried out using the SDOF model are described in Section 8.4 while the results of the simulations are shown in Section 8.5. Finally, a discussion of the results is presented in Section 8.6.

8.1 Model

The SDOF model relies on the assumption that the sheet pile–vibrator system behaves like a rigid body. This means that the head and the toe of the sheet pile is assumed to always have the same acceleration. The SDOF model is essentially identical to the uniaxal MDOF model, apart from that the longitudinal behaviour of the sheet pile is neglected. The model is visualised in Figure 8.1.

The model parameters from Chapter 5 were used when creating the model, relevant parameters are summarised in Table 8.1 for simplicity.

Table 8.1: Model parameters of the sheet pile and vibrator unit.

Parameter	Value	Unit
Sheet pile length, L_p	14	m
Sheet pile cross-section area, A_p	84.98	cm^2
Sheet pile perimeter, Ω_p	170.6	cm
Young's modulus, steel, E_s	210	GPa
Density, steel, ρ_s	7,800	kg/m^3
Driving frequency, f_d	41	Hz
Eccentric moment, M_e	0–12	kgm
Dynamic mass of vibrator unit, m_v	2,450	kg
Bias mass of vibrator unit, m_0	1,020	kg
Leader force, F_l	−140–70	kN

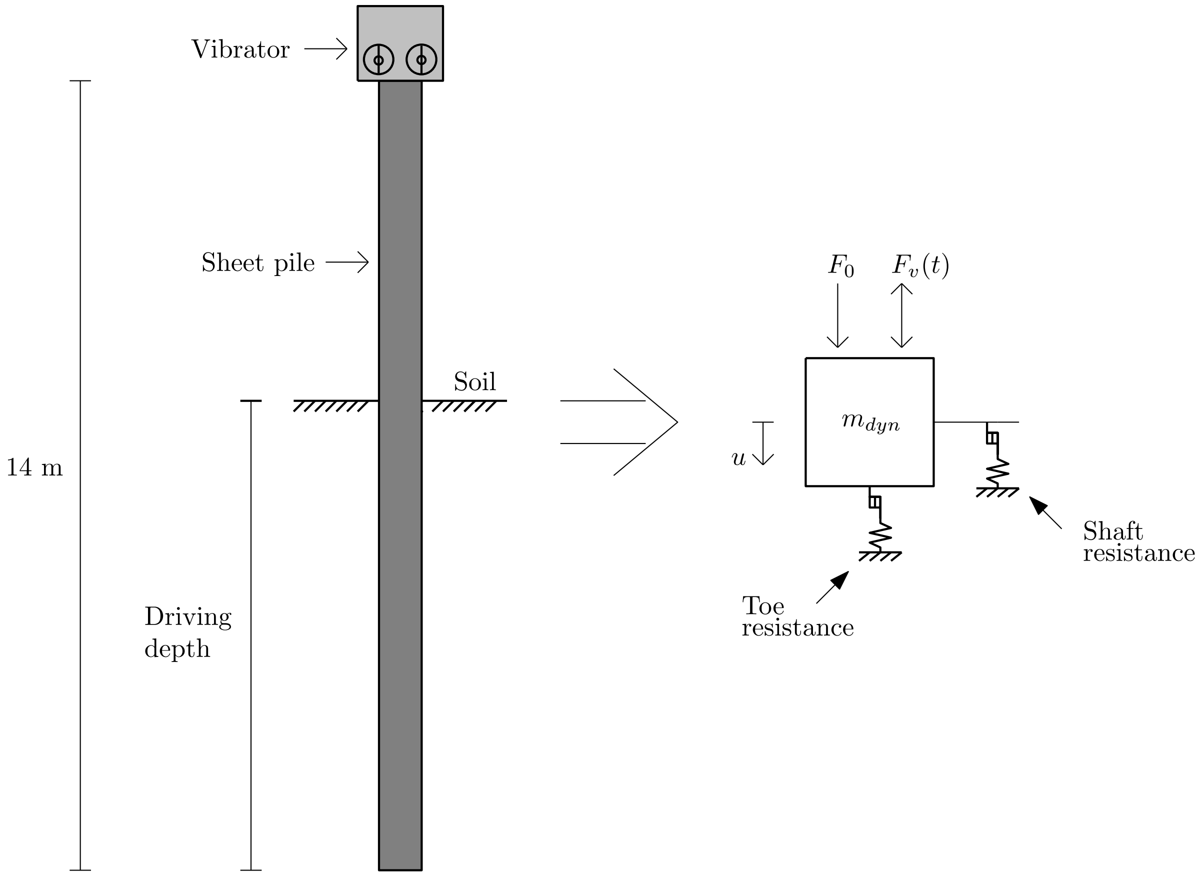

Figure 8.1: Illustration of the SDOF model of the sheet pile–vibrator system.

8.1.1 Dynamic mass

As the longitudinal behaviour of the sheet pile is neglected and the system is modelled with a single degree of freedom, the sheet pile–vibrator system is modelled as a single dynamic mass subjected to external forces. The dynamic mass m_{dyn} is the sum of the dynamic vibrator mass m_v and the sheet pile mass m_p

$$m_{dyn} = m_v + m_p \tag{8.1}$$

where m_v is the dynamic vibrator mass and where the sheet pile mass was calculated based on the sheet pile length L_p, density ρ_s and sheet pile area A_p as $m_p = L_p A_p \rho_s$.

8.1.2 Vibrator

The action from the vibrator was modelled using the method described in Section 2.4.1, thus the unbalanced vertical force was modelled as

$$F_v(t) = M_e \cdot \omega^2 \cdot sin(\omega t) \tag{8.2}$$

and the static surcharge force as

$$F_0 = m_0 \cdot g + F_l \tag{8.3}$$

where M_e is the eccentric moment, ω is the driving frequency in rad/s, t is the time, m_0 is the bias mass, and F_l is the leader force. The eccentric moment M_e was varied in the different simulations, while the leader force F_l was assumed to vary with the penetration depth as determined in the model calibration in Section 7.4.

8.1.3 Shaft resistance

Shaft resistance was included in the model with a spring and a slider, where the linear soil model for shaft resistance, described in Section 5.3, was used to describe the spring–slider behaviour. A maximum shaft resistance force $R_{s,max}$ was calculated as

$$R_{s,max} = \Omega_p \int_0^z \tau_d \, dz \tag{8.4}$$

with the dynamic shaft resistance profile τ_d from Section 5.2 and where z is the depth of the sheet pile toe and Ω_p is the perimeter of the sheet pile. The limits for the slider were set to $-R_{s,max} \leq R_s \leq R_{s,max}$. The stiffness for the spring was calculated as

$$k_s = \frac{R_{s,max}}{Q_s} \tag{8.5}$$

with the shaft quake $Q_s = 2.5$ mm.

8.1.4 Toe resistance

Toe resistance was included in the model with a spring and a slider, where the linear soil model for toe resistance, described in Section 5.3, was used to describe the spring–slider behaviour. A maximum toe resistance force $R_{t,max}$ was calculated as

$$R_{t,max} = A_p \cdot q_d(z) \tag{8.6}$$

with the dynamic toe resistance profile q_d from Section 5.2 and where z is the depth of the sheet pile toe and A_p is the sheet pile area. The limits for the slider were set to $0 \leq R_t \leq R_{t,max}$. The stiffness for the spring was calculated as

$$k_t = \frac{R_{t,max}}{Q_t} \tag{8.7}$$

with the toe quake $Q_t = 2.8$ mm.

8.1.5 Impact with boulder

Impact with a boulder was modelled in the same manner as the MDOF model, i.e. by changing the behaviour of the toe resistance so that it corresponded to the contact behaviour observed in the FE model. The method used to determine the behaviour is described in detail in Section 6.4.1. The impact at the center of the web was studied, and the same behaviour as in the MDOF model was assumed. The parameters describing the impact behaviour is repeated in Table 8.2 for simplicity. See Section 7.1.6 for a description of how the parameters were estimated. The impact location is visualised in Figure 8.2.

Table 8.2: Parameters describing the impact behaviour.

Parameter	Value	Unit
Loading stiffness	100	MN/m
Unloading stiffness	100	MN/m
Maximum load	300	kN

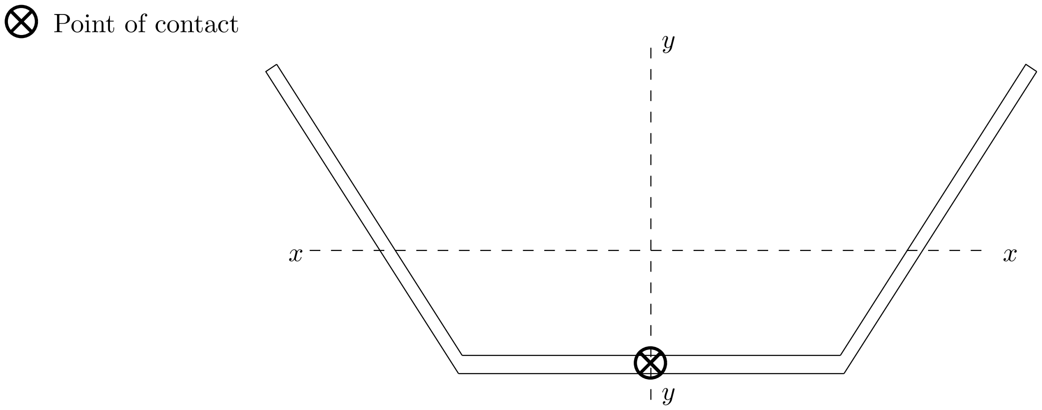

Figure 8.2: Illustration of the impact location.

8.2 Simulation method

The simulations were carried out using the Central Difference Method by implementing the iteration scheme for SDOF systems from Section 3.1. The initial conditions needed to start the iteration scheme was set to zero, however, this should have had no effect on the results as the iterations were continued until a steady state had been reached. The time step size was set to 5 microseconds, which is motivated with the convergence study in Section 8.3.

The MATLAB code that was written to set up the model, and run the simulations is included in Appendix B.2.

8.3 Convergence study

A convergence study was carried out to ensure that a small enough time-step was used in the simulations. The convergence study was done by visually comparing the accelerations during steady state for different time steps. The input used in the convergence study is summarised in Table 8.3. The peak acceleration as a function of the time step size is shown in Figure 8.3, from which it was concluded that a time step size of 5 microseconds was sufficient.

Table 8.3: Parameters used in the convergence study.

Parameter	Value	Unit
Penetration depth	10	m
Eccentric moment, M_e	6	kgm
Leader force, F_l	30	kN

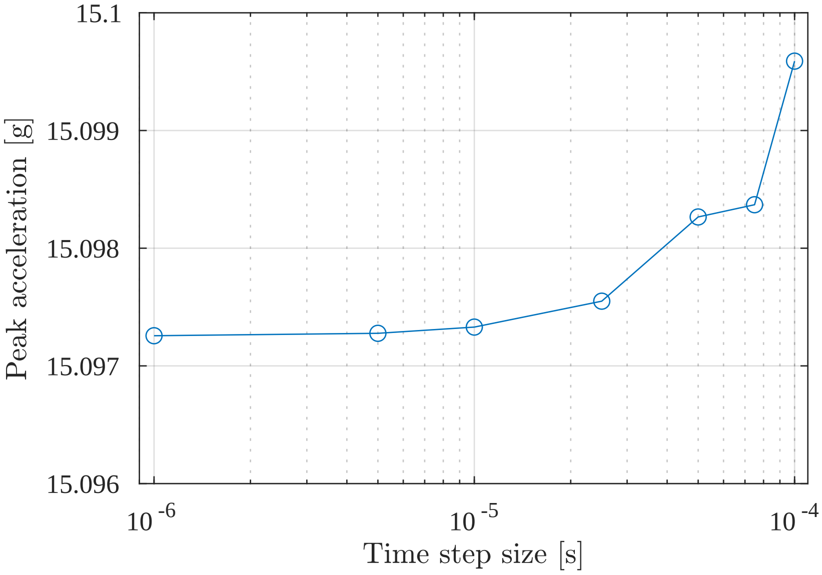

Figure 8.3: Convergence study for the time step size. Peak acceleration as a function of the time step size.

8.4 Simulations

The simulations that were carried out with the SDOF model are described in this section, while selected results from the simulations are shown in Section 7.6.

8.4.1 Vibratory driving simulations

Vibratory driving at two, six and ten metres penetration depth were simulated to study if the model produces result that correspond well with the reference case. The simulations were run until it was certain that a steady state had been reached

The parameters used in the three simulations are shown in Table 8.4.

Table 8.4: Input parameters for vibratory driving simulations.

Penetration depth [m]	Eccentric moment M_e [kgm]	Leader force F_l [kN]
10	6	30
6	6	5
2	6	−14.5

8.4.2 Impact simulations

The impact described in Section 8.1.5 was simulated. The penetration depth was assumed to ten metres and two different eccentric moments, 6 and 12 kgm, were studied for the impact. The impact simulations were, as previously mentioned, carried out by changing the behaviour of the toe resistance so that it corresponded to the contact force versus displacement curves from the FE model. The simulations were carried out by running an ordinary vibratory driving simulation until a steady state had been reached and then changing the behaviour of the toe resistance.

The parameters used in the simulations are shown in Table 8.5.

Table 8.5: Input parameters for impact simulations.

.

Parameter	Value	Unit
Penetration depth	10	m
Eccentric moment, M_e	6 & 12	kgm
Leader force, F_l	30	kN

8.5 Results

Selected results from the simulations with the SDOF model are presented in this section. Some brief comments on the results are also provided while a more in-depth discussion of the results is provided in Section 8.6. Note that the positive direction is downwards, e.g., a positive displacement corresponds to a downward displacement.

8.5.1 Vibratory driving simulations

Selected results from the vibratory driving simulations at two, six and ten metres penetration depth are presented in this section. The results were taken at a time when a steady state had been reached.

Vibratory driving at two metres depth

Figures 8.4 and 8.5 show displacement and acceleration for a penetration depth of two metres.

Figure 8.4 shows the displacement of the sheet pile. The upward displacement amplitude is approximately 3.3 mm while the downward displacement amplitude is approximately 4.7 mm. The penetration speed is about 55 mm/s. The results from the reference case for two metres penetration depth shows an upward displacement amplitude of about 3 mm, a downward displacement amplitude of about 5 mm and a penetration speed of about 80 mm/s.

Figure 8.5 shows the acceleration of the sheet pile. The acceleration varies between 13g in the upward direction and 13.5g in the downward direction. The results from the reference case for two metres penetration depth show accelerations at the sheet pile toe varying between 15g in the upward direction and 11g in the downward direction.

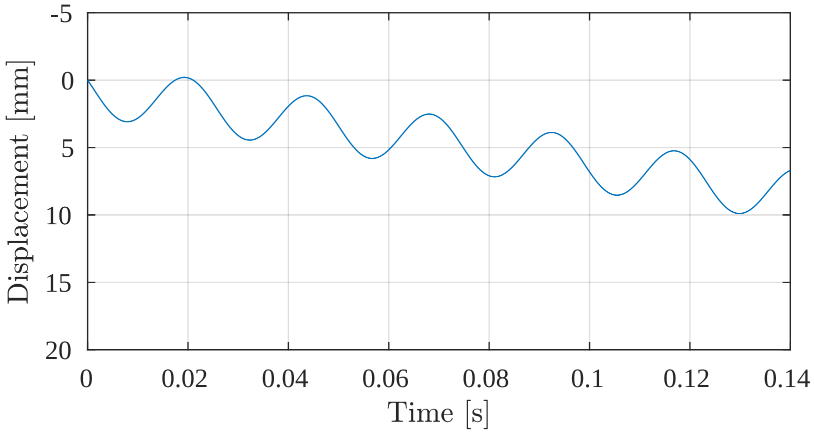

Figure 8.4: Displacement of sheet pile versus time for 2 m penetration depth.

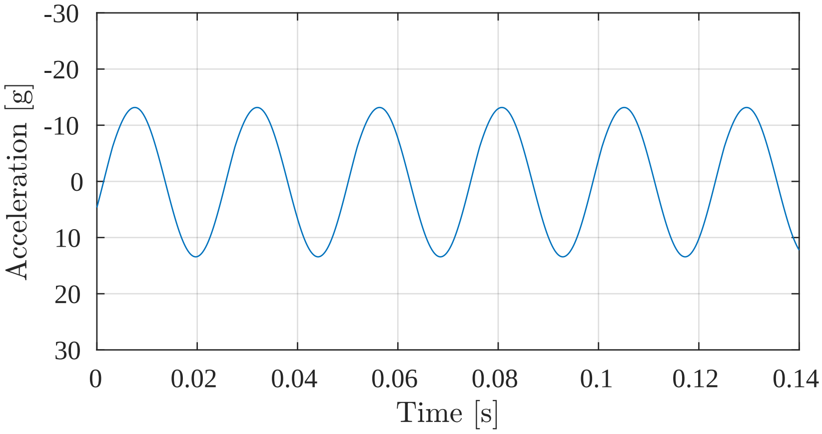

Figure 8.5: Acceleration of sheet pile versus time for 2 m penetration depth.

Vibratory driving at six metres depth

Figures 8.6 and 8.7 show displacement and acceleration for a penetration depth of six metres.

Figure 8.6 shows the displacement of the sheet pile. The upward displacement amplitude is approximately 3 mm while the downward displacement amplitude is approximately 5.3 mm. The penetration speed is about 92 mm/s. The results from the reference case for six metres penetration depth show an upward displacement amplitude of about 2.5 mm, a downward displacement amplitude of about 5 mm and a penetration speed of about 120 mm/s.

Figure 8.7 shows the acceleration of the sheet pile. The acceleration varies between 13.5g in the upward direction and 14g in the downward direction. The results from the reference case for six metres penetration depth show accelerations at the sheet pile toe varying between 18g in the upward direction and 12g in the downward direction.

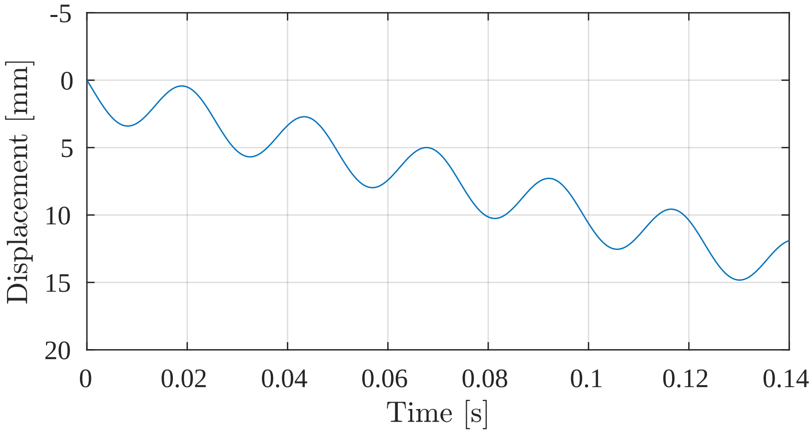

Figure 8.6: Displacement of sheet pile versus time for 6 m penetration depth.

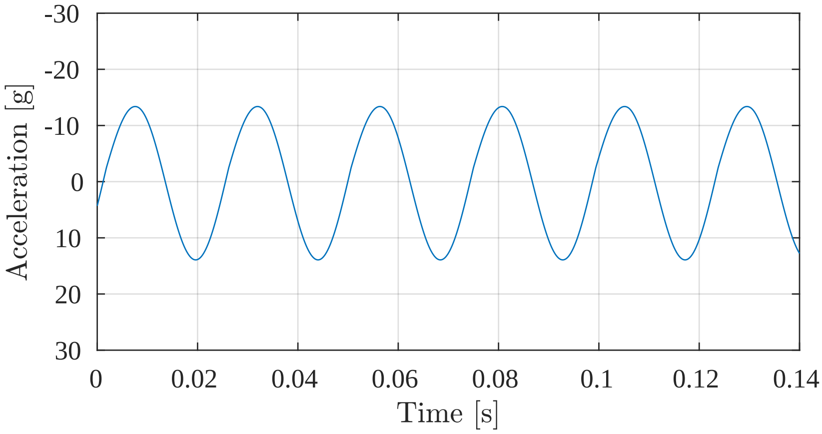

Figure 8.7: Acceleration of sheet pile versus time for 6 m penetration depth.

Vibratory driving at ten metres depth

Figures 8.8 and 8.9 show displacement and acceleration for a penetration depth of ten metres.

Figure 8.8 shows the displacement of the sheet pile. The upward displacement amplitude is approximately 3.1 mm while the downward displacement amplitude is approximately 5.8 mm. The penetration speed is about 107 mm/s. The results from the reference case for ten metres penetration depth show an upward displacement amplitude of about 2.5 mm, a downward displacement amplitude of about 5 mm and a penetration speed of about 130 mm/s.

Figure 8.9 shows the acceleration of the sheet pile. The acceleration varies between 14g in the upward direction and 15g in the downward direction. The results from the reference case for ten metres penetration depth show accelerations at the sheet pile toe varying between 15g in the upward direction and 12g in the downward direction.

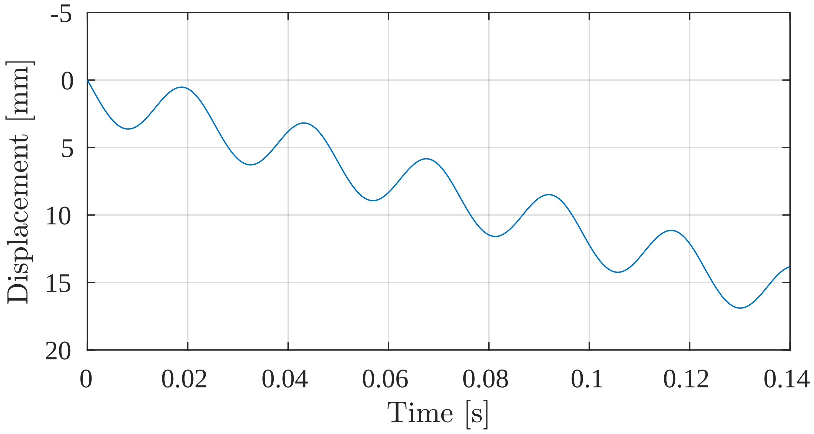

Figure 8.8: Displacement of sheet pile versus time for 10 m penetration depth.

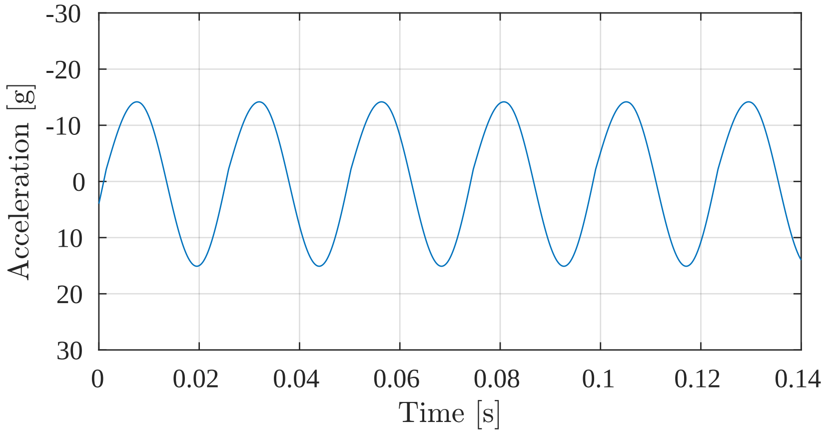

Figure 8.9: Acceleration of sheet pile versus time for 10 m penetration depth.

8.5.2 Impact simulations

Selected results from the impact simulations with eccentric moments of 6 and 12 kgm are presented in this section.

Impact–eccentric moment of 6 kgm

Figures 8.10 and 8.11 show displacement and acceleration before and after impact for an eccentric moment of 6 kgm. The first contact occurs at about $t = 0.108$ s.

Figure 8.10 shows that the penetration speed is approximately 107 mm/s before the impact and 0 mm/s after the impact. Figure 8.11 shows that the acceleration varies between 14g in the upward direction and 15g in the downward direction before the impact, which corresponds to a peak-to-peak amplitude of 29g. The acceleration varies between 20g in the upward direction and 18g in the downward direction after the impact, which corresponds to a peak-to-peak amplitude of 38g. Thus, the impact results in a 43% increase in upward acceleration, a 20% increase in downward acceleration and a 31% increase in peak-to-peak amplitude.

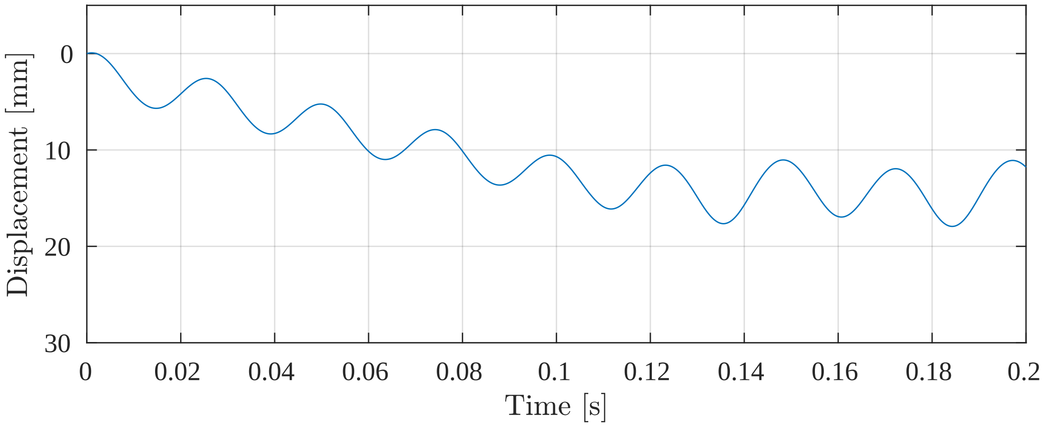

Figure 8.10: Displacement of sheet pile versus time for for an eccentric moment of 6 kgm.

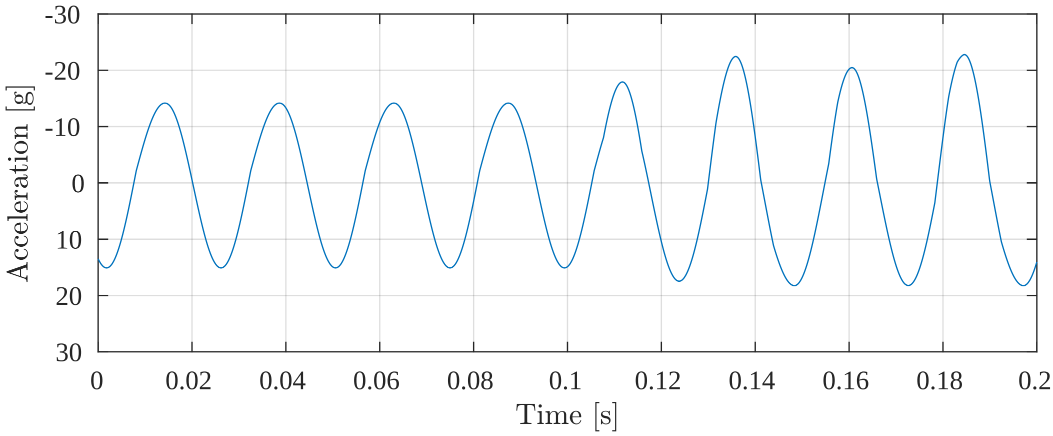

Figure 8.11: Acceleration of sheet pile versus time for an eccentric moment of 6 kgm.

Impact–eccentric moment of 12 kgm

Figures 8.12 and 8.13 shows displacement and acceleration before and after impact for an eccentric moment of 12 kgm. The first contact occurs at about $t = 0.108$ s.

Figure 8.12 shows that the penetration speed before the impact is approximately 393 mm/s and 0 mm/s after the impact. Figure 8.13 shows that the acceleration varies between 26g in the upward direction and 28g in the downward direction before the impact, which corresponds to a peak-to-peak amplitude of 54g. The acceleration varies between 34g in the upward direction and 30g in the downward direction after the impact, which corresponds to a peak-to-peak amplitude of 64g. Thus, the impact results in a 31% increase in upward acceleration, a 7% increase in downward acceleration and a 19% increase in peak-to-peak amplitude.

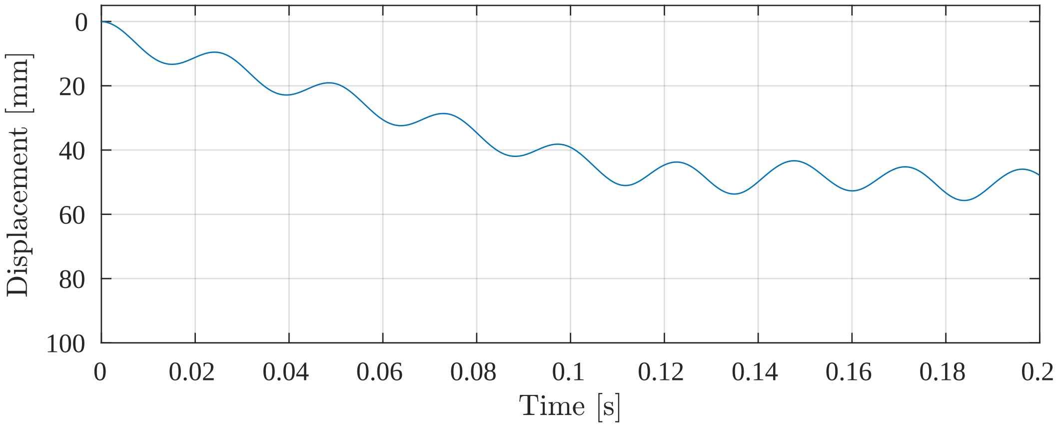

Figure 8.12: Displacement of sheet pile versus time for for an eccentric moment of 12 kgm.

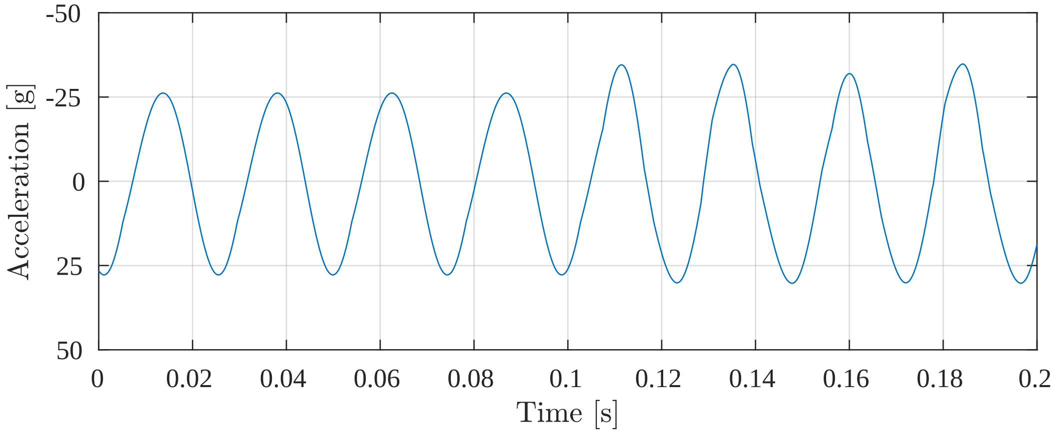

Figure 8.13: Acceleration of sheet pile versus time for an eccentric moment of 12 kgm.

8.6 Analysis

A discussion of the results in Section 8.5 are presented in this section.

Vibratory driving simulations

The model produced penetration speeds that are slightly lower than in the reference case. The maximum deviation in penetration speed is at two metres penetration depth, where the model produced a penetration speed (55 mm/s) that is about 31% lower than the corresponding penetration speed in the reference case (80 mm/s). The reason why the penetration speeds are consistently lower than in the reference case is not obvious, but it might be reasonable to assume that it is an effect of neglecting the longitudinal behaviour of the sheet pile.

The displacement amplitudes produced by the model correspond rather well to the reference case. The general shape of the displacement versus time curves also correspond well to the reference case. However, some deviations can be seen. The model produced upward and downward displacement amplitudes that in general are slightly higher than in the reference case. The maximum deviation in displacement amplitude is at ten metres penetration depth, where the model produced an upward displacement amplitude (3.1 mm) that is about 24% higher than the corresponding upward displacement amplitude in the reference case (2.5 mm). A part of these deviations can probably be attributed to human errors when estimating the displacement amplitudes from the plots in the reference case.

The accelerations produced by the model correspond fairly well to the reference, although there are some deviations. The maximum deviation in acceleration amplitude is at six metres penetration depth, where the model produced an upward acceleration amplitude (13.5g) that is about 25% lower than the corresponding upward acceleration amplitude in the reference case (18g). A part of these deviations can, as previously mentioned, probably be attributed to human errors when estimating the acceleration amplitudes from the plots in the reference case.

Impact simulations

The impact simulations show that the penetration speed goes to zero almost instantly when the impact occurs, which indicates that the relatively simple impact model works fairly well. The acceleration amplitude in both upward and downward direction increases after impact, where there generally is a higher increase in upward acceleration than in downward acceleration. The increase in peak-to-peak amplitude is 31% for the case with 6 kgm eccentric moment and 19% for the case with 12 kgm eccentric moment. The acceleration curves do not display any noticeable noise after the impacts, which was expected since the longitudinal behaviour of the sheet pile was neglected in this model.

9 Discussion

This chapter presents a general discussion of the results of the master's dissertation, and of the methods used to produce the results. Comparisons of the results from the three models are also presented. Note that a more in-depth discussion of the individual results is provided in Sections 6.6, 7.7, and 8.6.

Model comparison

The results from the vibratory driving simulations are similar for all three models. The displacement amplitudes and acceleration amplitudes are of the same magnitude and the characteristics of the vibratory driving behaviours are similar, as well. The uniaxial MDOF model and FE model both display similar overtones in the toe accelerations. This behaviour could not be seen in the SDOF model since the longitudinal behaviour of the sheet pile was neglected. The penetration speeds from the uniaxial MDOF model and FE model are very similar while the SDOF model produced slightly lower penetration speeds. The similar results in all three models indicate that it might be more efficient to simulate vibratory driving with simpler models. Furthermore, it seems like the uniaxial MDOF model is the most advantageous model when considering that it produces results that are very similar to the results from the FE model, and that it requires a lot less time to run the simulations.

The results from the impact simulations are also similar for the three models. The displacements and accelerations before and after impact are of the same magnitude in all three models. The Fast Fourier Transformations in the uniaxial MDOF model and FE model also show similar results. This again indicates that it might be more advantageous to use simpler models to simulate impacts during vibratory driving. However, it should be noted that it might be a bit cumbersome to model the impacts that have a higher degree of non-linearity (for example the impact at the flange edge) in the uniaxial MDOF model and SDOF model. Furthermore, the simple models do not provide any visualisation of the damage that has occurred. Finally, there might also be some dynamic effects that get neglected when determining the impact behaviour through quasi-static analysis.

Overtones in toe accelerations

Both the uniaxial MDOF model and FE model displayed rather significant overtones in the toe accelerations. This was somewhat reduced by including material damping in the models, but the overtones are still rather significant. This could probably have been reduced further by including more damping in the models. Furthermore, in the FE model, it would probably be beneficial to apply the shaft resistance over the pile shaft instead of at discrete points. Exactly how to do this without making the computations very heavy is not obvious. Another method to reduce the influence of high frequencies could be to perform modal reductions. The effect of the surrounding soil, and the vibrator unit, however, makes it complex to determine the modal behaviour theoretically.

Soil model

The soil model used in the dissertation is a rather simple linear model. The linear soil model was chosen as it gave results that corresponded relatively well to the reference case. It was also rather easy to implement the linear soil model in the FE model. The hyperbolic soil model, that was presented in the literature review, was tested in the uniaxial MDOF model in an early stage of the master's dissertation. The results from these tests did not correspond well to the reference case, for example, the penetration speeds were considerably lower than in the reference case. Based on this, it might be tempting to assume that the linear soil model is a more accurate representation of the true physical behaviour of the soil. However, one should be careful with such assumptions as linearity is fairly seldom in the physical world. It seems that not much is known about the dynamic soil resistances during vibratory driving, and the authors of the master's dissertation found few material models that describe these behaviours. It would therefore be of interest to conduct field studies where the dynamic resistances are accurately measured during vibratory driving. If a large number of such field studies were carried out it might be possible to establish accurate material models that describe the variation of the dynamic resistances during vibratory driving.

Stop criterion

The results from the impact simulations indicate that a stop criterion possibly could be based on abrupt changes in acceleration amplitude. The results indicate that it would be advantageous to continuously perform Fast Fourier Transformations of the accelerations and stop the vibratory driving if there is an abrupt increase of the acceleration amplitude at the driving frequency. Exactly how large the increase should be for the driving to stop cannot be concluded from the dissertation, mainly because a limited number of impact locations and boulder shapes were studied, and because the results from the impact simulations have not been verified with experimental field tests. Furthermore, the results from impacts at the flange edge indicate that it might be problematic to form a stop criterion solely based on changes in vertical acceleration, as these changes were rather small for the impacts at the flange edge. It might therefore be advantageous to also include lateral accelerations in a future stop criterion.

10 Conclusion and suggestions for further investigations

The purpose of the master's dissertation was to investigate if numerical models could be used to simulate vibratory driving of sheet piles, both with and without impact with boulders, and to investigate if a stop criterion could be based upon these numerical models.

The results of the vibratory driving simulations without impact indicate that the established FE model, MDOF model, and SDOF model all could simulate vibratory driving fairly well, where the FE model and uniaxial MDOF model gave almost identical results. It is therefore concluded that, with regards to the vibratory driving simulations only, the uniaxial MDOF model is the most efficient. The results of the impact simulations were also similar in all three models. However, based on the complexity of the impacts, it is concluded that the FE model is best suited for the impact simulations.

Based on the above, it was concluded that it would be beneficial to further develop both the uniaxial MDOF model and the FE model; the uniaxial model can be used to make quick vibro-driveability simulations, while modelling of the vibratory driving in the FE model is a prerequisite for making more accurate impact simulations.

The work with the dissertation resulted in the conclusion that there is a lack of accurate models of how the shaft resistance and toe resistance varies during vibratory driving. Further investigation on the subject is needed if truly accurate models of vibratory driving are to be established.

Finally, the results of the dissertation indicate that it might be possible to enforce a stop criterion by attaching accelerometers to the sheet pile head, and creating a system that continuously does FFTs of the accelerations and that stops the vibratory driving if there is a significant and abrupt change in acceleration amplitude at the driving frequency.

Suggestions for further investigations

During the work with the master's dissertation, some further investigation areas were discovered that would contribute to the current understanding of vibratory driving of sheet piles, and that would contribute in the development of a stop criterion. Furthermore, to confirm, and improve the models established in the dissertation, further investigation is needed. A list of potential continuations of the master's dissertation is presented below:

- Not much is known about the reduction in dynamic soil resistance during vibratory driving, and how the soil resistances vary during vibratory driving. The phenomenon of soil liquefaction during vibratory driving needs to be studied further, as well. This could probably be studied through experimental field studies.
- The models in the dissertation could be improved by calibrating them against further experimental field studies. It would be advantageous to calibrate the models against field studies where all vibratory related parameters are known, i.e., driving frequency, leader force variation, etc. The calibration could then be focused on other model parameters, such as damping and soil behaviour.
- The models in the dissertation could be improved by making them more advanced, e.g., by including interlocking friction, lateral soil pressure, failure of the impact obstacle, displacement of the impact obstacle, etc.
- Rather than using only vertical accelerations to develop a stop criterion, it could potentially be more advantageous to also base it upon lateral acceleration. This might also be a good way of detecting impacts at the flange edges, which proved to be problematic with the models in the dissertation.
- Studies regarding the effects of driving the sheet piles at the centre of gravity, rather than at the web, would be of interest.

Bibliography

[1] A. Ryner, A. Fredriksson and H. Stille. *Sponthandboken.* Byggforskningsrådet, Stockholm, 1996.

[2] K. Viking. *Vibro-driveability - a field study of vibratory driven sheetpiles in non-cohesive soils.* Doctoral Thesis: Department of Civil och Architectural Engineering, KTH Royal Institute of Technology, Stockholm, 2002.

[3] ThyssenKrupp. *Sheet Piling Handbook 3rd edition.* ThyssenKrupp, Germany, 2010.

[4] A. Holeyman, P. Peralta and N. Charue. "Boulder-soil-pile dynamic interaction". In: *Frontiers in Offshore Geotechnics III* (2015).

[5] J. Menno Maarten. *Pile tip deformation caused by obstacles.* Dept. of Marine Technology, Norwegian Univ. of Science and Technology, 2018.

[6] K. Viking and A. Garcia Benito. "Stoppdrivningskriterier för vibrodriven spont –en blind fläck i regelverket". In: *Bygg & teknik* 1 (2021).

[7] R. Moulai-Khatir, M. W. O'Neill and C. Vipulanandan. *Program VPDA Wave Equation Analysis for Vibratory Driving of Piles.* Dept of Civil and Environmental Engineering, Univ. of Houston, 1994.

[8] D. Van Rompaey, C. Legrand and A. Holeyman. "A prediction method for the installation of vibratory driven piles". In: *Transactions on the Built Environment* 14 (1995).

[9] A. Holeyman. *Soil Behavior under Vibratory Driving.* Swets & Zeitlinger, Lisse, 2002.

[10] K. Massarsch. *Vibratorers användningsmöjligheter vid drivning av pålar och spont.* Pålkommissionen, Rapport 99, Linköping, 2000.

[11] A. K. Chopra. *Dynamics of Structures: Theory and Applications to Earthquake Engineering, Fourth Edidtion.* Prentice Hall, New Jersey, USA, 2012.

[12] Dassault Systèmes. *SIMULIA User Assistance 2021.* Providence: Dassault Systèmes, 2021.

[13] N. Ottosen and H. Petersson. *Introduction to the Finite Element Method.* Prentice Hall, 1992.

[14] R. Larsson. *CPT-sondering utrustning – utförande – utvärdering. En in-situ metod för bestämning av jordlagerföljd och egenskaper i jord.* Swedish Geotechnical Institute, 2015.

[15] R. Lund Tebäck. *Dynamisk Finita element-analys av vibrodriven spontplanka.* Lund University: Division of Geotechnical Engineering, May, 2019.

Appendix A

Additional theory

A.1 Hyperbolic soil models

The hyperbolic soil models suggested by Moulai-Khatir et al. [7] is presented below. The hyperbolic soil models are shown in Figure A.1 where the shaft resistance τ (stress) varies between the maximum shaft resistance τ_{max} and minimum shaft resistance τ_{min}, and the toe resistance q (stress) varies between the maximum toe resistance q_{max} and 0.

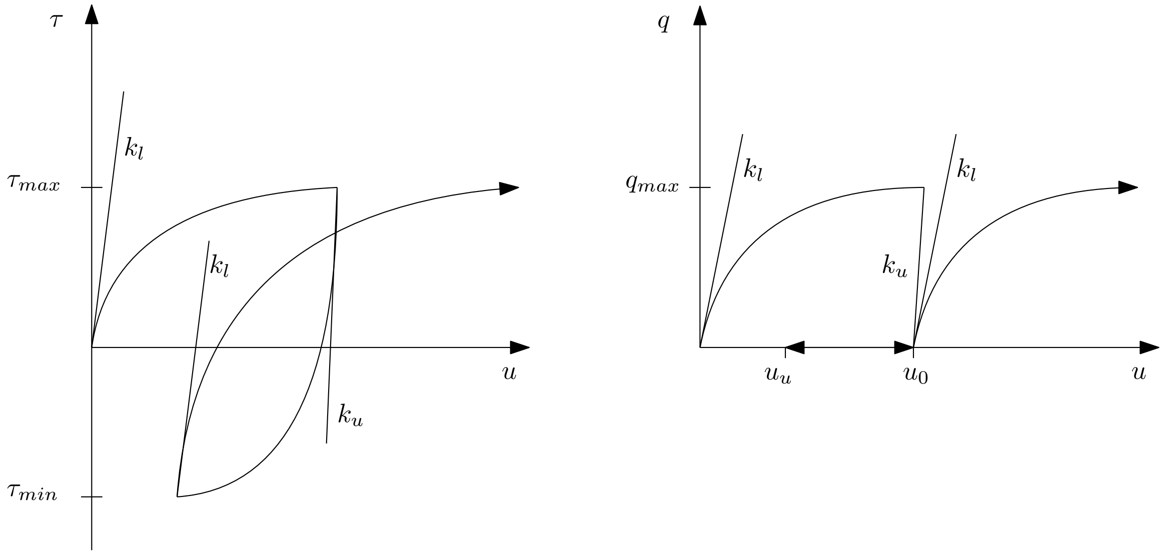

Figure A.1: Variation of shaft resistance τ, and toe resistance q with the displacement D, modified after Moulai-Khatir et al. [7].

The loading curve for the shaft resistance in Figure A.1 is determined as

$$\tau = \tau_p + \frac{k_l \cdot (D - D_p)}{(1 + (\frac{k_l \cdot (D-D_p)}{\tau_{max}-\tau_p})^{\mu})^{\frac{1}{\mu}}}, \tag{A.1}$$

and the unloading curve as

$$\tau = \tau_p - \frac{k_u \cdot (D_p - D)}{(1 + (\frac{k_u \cdot (D_p-D)}{\tau_p-\tau_{min}})^{\mu})^{\frac{1}{\mu}}}, \tag{A.2}$$

where u_p is the displacement at the previous load reversal, τ_p is the load at the previous load reversal, k_l is the loading stiffness, k_u is the unloading stiffness, and μ is an empirical shape parameter.

The loading curve for the toe resistance in Figure A.1 is determined as

$$q = q_p + \frac{k_l \cdot (D - D_p)}{(1 + (\frac{k_l \cdot (D - D_p)}{q_{max} - q_p})^{\mu})^{\frac{1}{\mu}}} \tag{A.3}$$

if the load at previous reversal q_p was larger than 0, and as

$$q = \frac{k_l \cdot (D - D_0)}{(1 + (\frac{k_l \cdot (D - D_o)}{q_{max}})^{\mu})^{\frac{1}{\mu}}} + q_p \tag{A.4}$$

if the load at previous reversal was 0.

The unloading curve for the toe resistance in Figure A.1 is determined as

$$q = q_p + (D - D_p) \cdot k_u. \tag{A.5}$$

Furthermore, the toe resistance is assumed to be zero between the points u_u and u_0 in Figure A.1, as the toe is not in contact with the soil. Moulai-Khatir et al. [7] presented the parameters shown in Table A.1 for the hyperbolic model for H-piles and open-ended pipe piles driven in saturated sands. The parameters were, according to Moulai-Khatir et al. [7], obtained from large scale laboratory tests.

Table A.1: Parameters for hyperbolic soil model, based on Moulai-Khatir et al. [7].

	Pipe pile	H-pile
Toe loading stiffness	2,006 MN/m^3	2,082 MN/m^3
Shaft loading stiffness	1.75 MN/m^3	1.78 MN/m^3
Toe loading exponent, μ	2.31	2.32
Shaft loading exponent, μ	2.53	2.46
Toe unloading stiffness	2,169 MN/m^3	2,112 MN/m^3
Shaft unloading stiffness	1.76 MN/m^3	1.82 MN/m^3
Toe unloading exponent, μ	2.30	2.35
Shaft unloading exponent, μ	2.34	2.41

A.2 Amplitude values of dynamic soil resistances

The profiles for the amplitude values of the dynamic shaft resistance τ_d and dynamic toe resistance q_d (stresses) were estimated with the method described in Section 2.5.3 and based on the simplified soil resistances and friction ratio in Figure A.2, repeated here for simplicity. The method used to estimate the amplitude values of the dynamic soil resistances is summarised below.

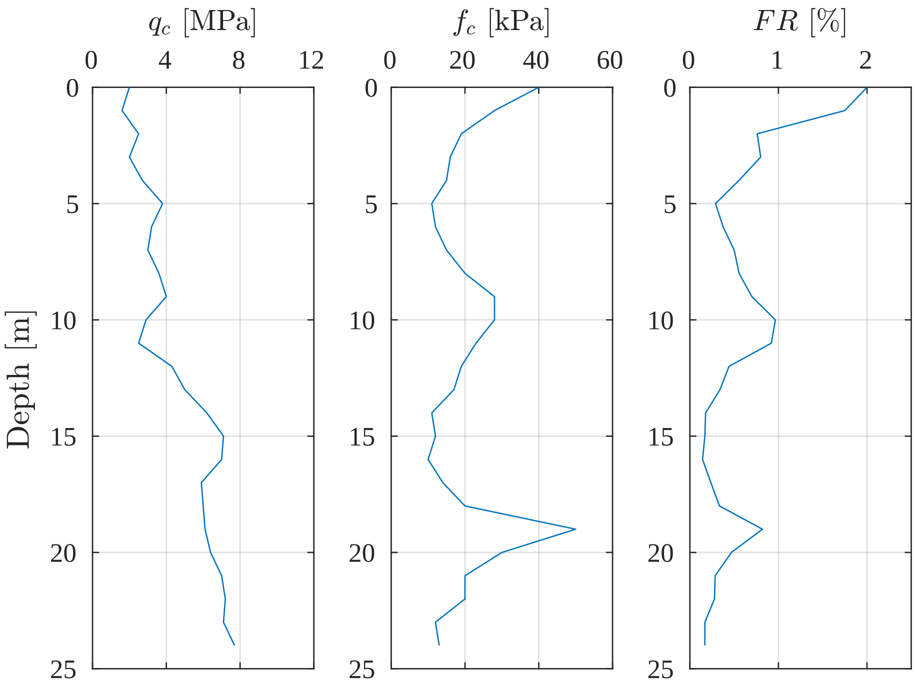

Figure A.2: Simplified tip resistance q_c, skin friction f_c, and friction ratio FR, plotted versus soil depth.

The acceleration amplitude for the sheet pile was estimated as

$$a = \frac{M_e \omega^2}{m_{dyn}} = \frac{6 \cdot (41 \cdot 2 \cdot \pi)^2}{2450 + 930} = 117.8 \text{ m/s}^2 \tag{A.6}$$

which corresponds to the acceleration ratio

$$\alpha_r = \frac{117.8}{g} = 12\text{g} \tag{A.7}$$

where the eccentric moment was assumed to $M_e = 6$ kgm, the driving frequency was assumed to 41 Hz and the dynamic mass m_{dyn} was assumed to (2450 + 930) kg, which corresponds to the dynamic mass of the vibrator and the mass of the sheet pile, respectively.

The liquefied soil resistances q_l and τ_l were calculated as:

$$\tau_l = \tau_s \cdot \left[(1 - \frac{1}{L}) \cdot e^{-\frac{1}{FR}} + 1/L\right] \tag{A.8}$$

$$q_l = q_s \cdot \left[(1 - \frac{1}{L}) \cdot e^{-\frac{1}{FR}} + 1/L\right], \tag{A.9}$$

where the static toe resistance q_s was taken as the tip resistance q_c in Figure A.2, the static shaft resistance τ_s as the skin friction f_c in Figure A.2, and the friction ratio FR from Figure A.2. The empirical liquefaction factor L was assumed to 7. The estimated liquefied soil resistances are shown in Figure A.3.

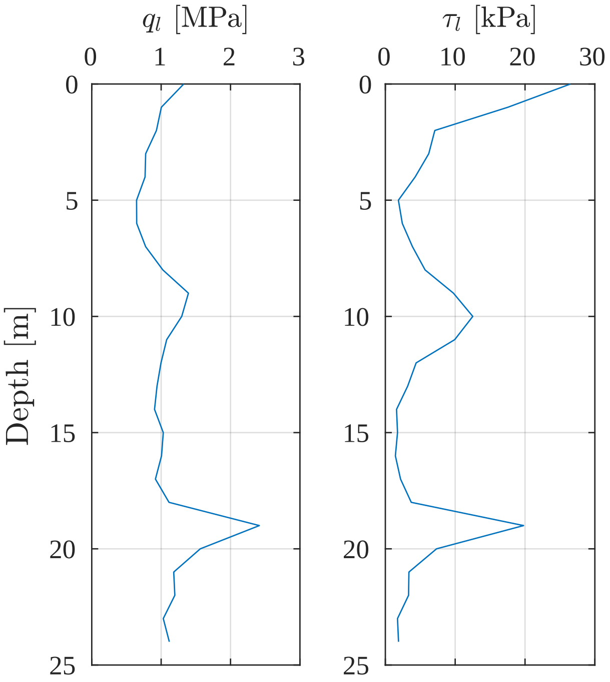

Figure A.3: Estimated liquefied toe resistance q_l, and liquefied shaft resistance τ_l, plotted versus penetration depth.

The dynamic soil resistances τ_d and q_d were calculated as:

$$\tau_d = (\tau_s - \tau_l) \cdot e^{-\alpha_r} + \tau_l \tag{A.10}$$

$$q_d = (q_s - q_l) \cdot e^{-\alpha_r} + q_l. \tag{A.11}$$

The influence of the acceleration ratio is visualised in Figure A.4, where the dynamic shaft resistance at ten metres penetration depth is plotted as a function of the acceleration ratio. The resulting profiles for the dynamic toe and shaft resistances are shown in Figure A.5.

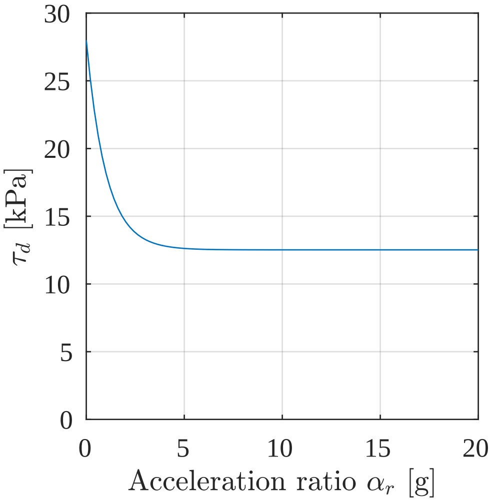

Figure A.4: Influence of the acceleration ratio on the dynamic shaft resistance.

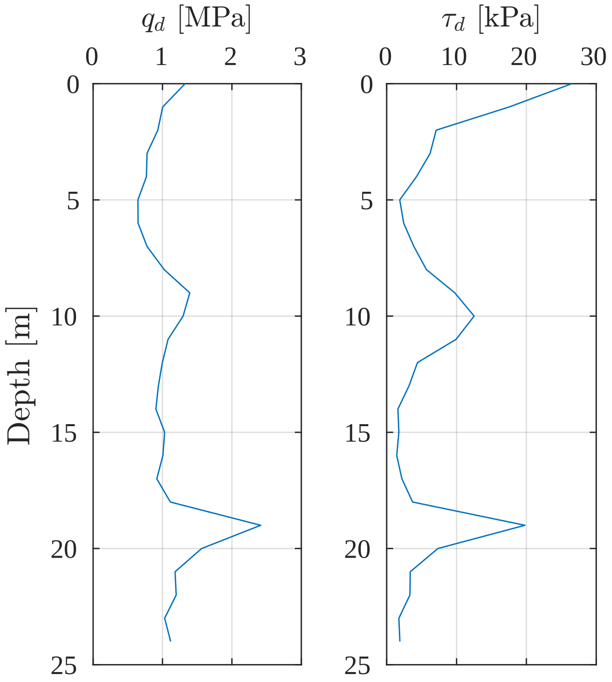

Figure A.5: Estimated dynamic toe resistance q_d, and dynamic shaft resistance τ_d, plotted versus penetration depth.

Now the next step would have been to estimate a new acceleration ratio, taking the resistances into account. However, Figure A.4 shows that this is not necessary as the acceleration ratio would need to be lowered from $\sim$ 12g to $\sim$ 4g for the dynamic shaft resistances to change. Thus, it was assumed that the dynamic soil resistance profiles in Figure A.5 are valid.

A.3 Rayleigh damping

This section is based upon Chopra [11].

Rayleigh damping is the combination of mass-proportional damping, and stiffness-proportional damping in a structure. The damping constants α, and β, together with the established orthogonal mass-, and stiffness matrices $\boldsymbol{M}$, and $\boldsymbol{K}$, respectively, form the damping matrix $\boldsymbol{C}$ such as

$$\boldsymbol{C} = \alpha \boldsymbol{M} + \beta \boldsymbol{K}. \tag{A.12}$$

The damping coefficients are dependant on specific damping ratios ζ_n at any two modes of vibration, at the corresponding natural frequency ω_n. This expression can be formulated as

$$\zeta_n = \frac{\alpha}{2\omega_n} + \frac{\beta\omega_n}{2}, \tag{A.13}$$

and can be seen in Figure A.6. Generally, approximately the same damping ratios occur for several modes of vibration. To get a frequency and damping ratio proportion that corresponds to experimental tests, and physical behaviour, the damping coefficients α, and β must be solved from two algebraic expressions of Equation (A.13). Two damping ratios, and corresponding natural frequencies, must be chosen to give the proportion that deviates the least from experimental tests results, and physical behaviour.

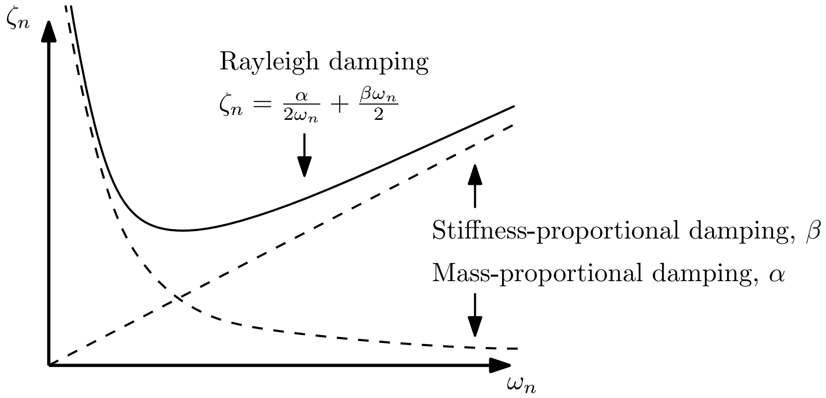

Figure A.6: Variation of damping ratio versus natural frequency for Rayleigh damping, mass-proportional damping, and stiffness proportional damping.

The stiffness-proportional damping can be interpreted as the energy dissipation arising from inner deformation in the structure, while the mass-proportional damping can be seen as air damping the structure, which often is neglectable.

Appendix B

MATLAB code

B.1 Uniaxial MDOF model

```
% Anton Andersson & Johannes Jonsson
% Development of stop criterion for vibratory driving of steel sheet piles
% Master’s Dissertation
% Uniaxial MDOF model
clear all
close all

% General
g = 9.81;
```

Input

```
Depth = 10;         % Penetration depth
Me = 6;             % Eccentric moment
Fl = 30e3;          % Leader force
```

Sheet pile parameters

```
Lp = 14;            % Length
Ap = 84.98*1e-4;    % Area
Pp = 1.706;         % Perimeter
Ep = 210e9;         % Young’s modulus
fy = 355e6;         % Yield stress
rho = 7800;         % Density
mp = Lp*rho*Ap;     % Pile mass
```

Vibrator parameters

```
fd = 41;            % Driving frequency
m0 = 1020;          % Bias mass
mv = 2450;          % Vibrator dynamic mass
F0 = m0*g + Fl;     % "Static load" + leader load
mdyn = mv + mp;     % Total dynamic mass
```

```
w = 2*pi*fd;        % Angular frequency
P0 = Me*w^2;        % Amplitude of harmonic load
```

Dynamic toe and shaft resistance based on CPT

```
L = 7;                          % Liquefaction factor 4-10
zCPT = linspace(0,24,25);       % Depth of CPT points

% Shaft friction from CPT
fc = 1e3*[40 28 19 16 15 11 12 15 20 28 28 23 ...
    19 17 11 12 10 14 20 50 30 20 20 12 13];

% Toe resistance from CPT
qc = 1e6*[2 1.6 2.5 2 2.7 3.8 3.2 3 3.6 4 2.9 2.5 ...
    4.3 5 6.2 7.1 7 5.9 6 6.1 6.4 7 7.2 7.1 7.7];

FR = 100*fc./qc;                                % Friction ratio
aratio = (Me*w^2)/(g*mdyn);                     % Estimated Acceleration [g]
Tl = fc.*((1-1/L).*exp(-1./FR)+1/L);            % Liquefied Shaft Resistance
Td = (fc-Tl).*exp(-aratio)+Tl;                  % Dynamic shaft resistance
ql = qc.*((1-1/L).*exp(-1./FR)+1/L);            % Liquefied Toe Resistance
qd = (qc-ql).*exp(-aratio)+ql;                  % Dynamic Toe resistance
```

Model parameters

```
nel = 14;                           % Number of elements
Lel = Lp/nel;                       % Element length
z = Depth-Lp:Lel:Depth;             % Depth for each node, (-) above ground
for i = 1:nel
    Edof(i,:) = [i; i; i+1];        % Topology
end
ndof = max(max(Edof));              % Number of nodes
```

Stiffness and mass

```
Ke = Ep*Ap/Lel*[1 -1; -1 1];       % Element sheet pile stiffness
Me = rho*Ap*Lel*[0.5 0; 0 0.5];    % Element sheet pile mass
K = zeros(ndof,ndof);
M = zeros(ndof,ndof);
M(1,1) = mv;                       % Add dynamic vibrator mass to first node

% Calculate stiffness and mass matrices
for i=1:nel
    index = Edof(i,2:end);
    K(index,index) = K(index,index) + Ke;
    M(index,index) = M(index,index) + Me;
```

```
end
```

Gravitational forces

```
gvec = g*ones(ndof,1);              % Gravity vector [g ; g ; g ;... g]
fextg = M*gvec;                     % Gravity force vector
```

Soil resistance vectors

```
% Interpolate to get more points before intergration
zint = 0:Lel/2:24;
Ts_int = interp1(zCPT,fc,zint);
qs_int = interp1(zCPT,qc,zint);
Td_int = interp1(zCPT,Td,zint);
qd_int = interp1(zCPT,qd,zint);

% Calculate maximum dynamic shaft resistance for each node
for i = 1:ndof

    % Integration limits
    zlim1 = z(i) - Lel/2;
    zlim2 = z(i) + Lel/2;

    if zlim1 < 0
        zlim1 = 0;
    end
    if zlim2 < 0
        zlim2 = 0;
    end
    if zlim2 > Depth
        zlim2 = Depth;
    end

    if zlim1 == 0 && zlim2 == 0
        RsMax = 0;
        continue
    end

    lim1indx = find(zint == zlim1);
    lim2indx = find(zint == zlim2);

    % Maximum dynamic shaft resistance vector
    RsMax(i,1) = Pp*trapz(zint(lim1indx:lim2indx),Td_int(lim1indx:lim2indx));

end
```

```
% Shaft resistance spring stiffness for each node
Qs = 2.5e-3;                    % Quake, (elastic limit)
for j = 1:ndof
    ks(j) = RsMax(j)/Qs;
end

% Toe resistance
RtMax = zeros(ndof,1);
zToeindx = find(zint == Depth);         % Index for bottom node
RtMax(ndof) = Ap*qd_int(zToeindx);      % Max toe resistance

% Toe resistance spring stiffness for each node
Qt = 2.8e-3;       % Toe quake  (elastic limit)
for j = 1:ndof
    kt(j) = RtMax(j)/Qt;
end
```

Material damping for sheet pile

```
wn = sqrt(eig(K,M));        % Natural frequencies
xi = 0.01;                  % Damping ratio
betaD = 2*xi/wn(2);         % Stiffness proportional damping
alphaD = 0;                 % Mass proportional damping
C = alphaD*M + betaD*K;
```

Total time and size of timestep

```
tottime = 1;                        % Total simulation time
dt = 5e-6;                          % Size of timestep
nstep = round(tottime/dt);          % Number of steps
```

Initial quantities

```
t = 0;                          % Initial time
u0 = zeros(ndof,1);             % Initial displacements
uprim0 = zeros(ndof,1);         % Initial velocities
fext_0 = zeros(ndof,1);         % Initial forces
ubiz0 = zeros(ndof,1);          % Initial accelerations

% Initial accelerations if inital disp., vel. and/or forces is not 0.
% ubiz0 = M\(fext_0 - C*uprim0 - K*u0);

u_1 = u0 - dt*uprim0 + dt^2*ubiz0/2;        % Displacements at i-1

% Iteration quantities
khat = M/dt^2+C/(2*dt);      a = M/dt^2-C/(2*dt);     b = K - 2*M/dt^2;
```

```
% Special case for initial step
in = 1;

% Vectors and matrices
Rs = zeros(ndof,1);
Rt = zeros(ndof,1);
u = zeros(ndof,nstep);
uRt = zeros(ndof,nstep);
```

Start iteration

```
for i = 1:nstep

    % Current time
    t = t + dt;
    tvec(i) = t;

    % Special case for first iteration
    if in == 1
        ui = u0;
        u_i = u_1;
        v_i = uprim0;
    else
        ui = u(:,i);
        u_i = u(:,i-1);
        v_i = v(:,i-1);
    end

    % Determine shaft resistance
    for j = 1:ndof

        % Set shaft resistance to zero if node is above ground
        if RsMax(j) == 0
            Rs(j) = 0;
            continue
        end

        % Displacement increment
        du = ui(j) - u_i(j);

        % If increment in u is 0, set increment in Rs to 0
        if du == 0
            dRs(j) = 0;
        else
            dRs(j) = du*ks(j);
        end
```

```
    % New shaft resistance
    Rs(j) = Rs(j) + dRs(j);

    % If new shaft resistance is larger than max, set to max
    % If new shaft resistance is smaller than min, set to min
    if abs(Rs(j)) >= RsMax(j)
        Rs(j) = sign(Rs(j))*RsMax(j);
    end
end

% Determine toe resistance
for j = 1:ndof

    % Set toe resistance to zero if node is not at bottom
    if RtMax(j) == 0
        Rt(j) = 0;
        continue
    end

    % Displacement increment
    du = ui(j) - u_i(j);

    % If increment in u is 0, set increment in Rs to 0
    % else set dRs = du*kt
    if du == 0
        dRt(j) = 0;
    else
        dRt(j) = du*kt(j);
    end

    % If previous Rt was larger than 0, and current Rt will be smaller
    % than zero, set displacement limit for when loading happens again
    if Rt(j) > 0 & Rt(j) + dRt(j) <= 0
        uRt(j) = ui(j);
    end

    % New toe resistance
    Rt(j) = Rt(j) + dRt(j);

    % If new toe resistance is larger than max, set to max
    if Rt(j) >= RtMax(j)
        Rt(j) = RtMax(j);
    end

    % If new toe resistance is smaller than 0, set to 0
    if Rt(j) < 0
        Rt(j) = 0;
```

```
        end

        % If current displacement is less than limit for loading,
        % set toe resistance to 0
        if ui(j) < uRt(j)
            Rt(j) = 0;
        end
    end

    % External forces
    fext = fextg - Rs - Rt;
    fext(1,1) = fext(1,1) + F0 + P0*sin(w*t);

    % Iteration "force"
    phat = fext - a*u_i - b*ui;

    % Solve for u(i+1)
    u(:,i+1) = khat\phat;

    % Calculate velocities and accelerations
    v(:,i) = (u(:,i+1)-u_i)/(2*dt);
    A(:,i) = (u(:,i+1)-2*ui + u_i)/(dt^2);

    % Reset "in" for first iteration
    in = 0;
end
```

B.2 SDOF model

```
% Anton Andersson & Johannes Jonsson
% Development of stop criterion for vibratory driving of steel sheet piles
% Master's Dissertation
% SDOF model
clear all
close all

% General
g = 9.81;
```

Input

```
Depth = 10;         % Penetration depth
Me = 6;             % Eccentric moment
Fl = 30e3;          % Leader force
```

Sheet pile parameters

```
Lp = 14;            % Length
Ap = 84.98*1e-4;    % Area
Pp = 1.706;         % Perimeter
Ep = 210e9;         % Young's modulus
fy = 355e6;         % Yield stress
rho = 7800;         % Density
mp = Lp*rho*Ap;     % Pile mass
```

Vibrator parameters

```
fd = 41;            % Driving frequency
m0 = 1020;          % Bias mass
mv = 2450;          % Vibrator dynamic mass
F0 = m0*g + Fl;     % "Static load" + leader load
mdyn = mv + mp;     % Total dynamic mass
w = 2*pi*fd;        % Angular frequency
P0 = Me*w^2;        % Amplitude of harmonic load
```

Dynamic toe and shaft resistance based on CPT

```
L = 7;                          % Liquefaction factor 4-10
zCPT = linspace(0,24,25);       % Depth of CPT points

% Shaft friction from CPT
fc = 1e3*[40 28 19 16 15 11 12 15 20 28 28 23 ...
    19 17 11 12 10 14 20 50 30 20 20 12 13];

% Toe resistance from CPT
qc = 1e6*[2 1.6 2.5 2 2.7 3.8 3.2 3 3.6 4 2.9 2.5 ...
    4.3 5 6.2 7.1 7 5.9 6 6.1 6.4 7 7.2 7.1 7.7];

FR = 100*fc./qc;                            % Friction ratio
aratio = (Me*w^2)/(g*mdyn);                 % Estimated Acceleration [g]
Tl = fc.*((1-1/L).*exp(-1./FR)+1/L);        % Liquefied Shaft Resistance
Td = (fc-Tl).*exp(-aratio)+Tl;              % Dynamic shaft resistance
ql = qc.*((1-1/L).*exp(-1./FR)+1/L);        % Liquefied Toe Resistance
qd = (qc-ql).*exp(-aratio)+ql;              % Dynamic Toe resistance
```

Soil resistances

```
% Shaft resistance
ulimpos = find(zCPT == Depth);

% Maximum total shaft resistance
```

```
RsMax = Pp*trapz(zCPT(1:ulimpos),Td(1:ulimpos));

Qs = 2.5e-3;            % Quake, (elastic limit)
ks = RsMax/Qs;          % Shaft resistance loading/unloading stiffness

% Toe resistance
RtMax = Ap*qd(ulimpos);     % Maximum toe resistance
Qt = 2.8e-3;                % Toe quake  (elastic limit)
kt = RtMax/Qt;              % Toe resistance loading/unloading stiffness
```

Total time and size of timestep

```
tottime = 1;                        % Total simulation time
dt = 5e-6;                          % Size of timestep
nstep = round(tottime/dt);          % Number of steps
```

Initial quantities

```
t = 0;                      % Initial time
u0 = 0;                     % Initial displacement
uprim0 = 0;                 % Initial velocity
ubiz0 = 0;                  % Initial acceleration
fext_0 = 0;                 % Initial force
u_1 = 0;                    % Displacement at i-1

% Iteration quantities
khat = mdyn/dt^2;      a = mdyn/dt^2;     b = -2*mdyn/dt^2;

% Special case for initial step
in = 1;

% Initial values
Rs = 0;
Rt = 0;
uRt = 0;
u = 0;
```

Start iteration

```
for i = 1:nstep

    % Current time
    t = t + dt;
    tvec(i) = t;

    % Special case for first iteration
```

```
    if in == 1
        ui = u0;
        u_i = u_1;
        v_i = uprim0;
    else
        ui = u(i);
        u_i = u(i-1);
        v_i = v(i-1);
    end

% Determine shaft resistance

    du = ui - u_i;           % Displacement increment

    % If increment in u is 0, set increment in Rs to 0
    if du == 0
       dRs = 0;
    end

    if du > 0
        dRs = du*ks;
    end

    if du < 0
        dRs = du*ks;
    end

    % New shaft resistance
    Rs = Rs + dRs;

    % If new shaft resistance is larger than max, set to max
    % If new shaft resistance is smaller than min, set to min
    if abs(Rs) >= RsMax
        Rs = sign(Rs)*RsMax;
    end


% Determine toe resistance

    du = ui - u_i;           % Displacement increment

    % If increment in u is 0, set increment in Rt to 0
    % else set dRt = du*kt
    if du == 0
        dRt = 0;
    else
        dRt = du*kt;
    end
```

```
    % If previous Rt was larger than 0, and current Rt will be smaller
    % than zero, set displacement limit for when loading happens again
    if Rt > 0 && Rt + dRt <= 0
        uRt = ui;
    end

    % New toe resistance
    Rt = Rt + dRt;

    % If new toe resistance is larger than max, set to max
    if Rt >= RtMax
        Rt = RtMax;
    end

    % If new toe resistance is smaller than 0, set to 0
    if Rt < 0
        Rt = 0;
    end

    % If current displacement is less than limit for loading,
    % set toe resistance to 0
    if ui < uRt
        Rt = 0;
    end

    % External forces
    fext = F0 + P0*sin(w*t) + mdyn*g - Rs - Rt;

    % Iteration "force"
    phat = fext - a*u_i - b*ui;

    % Solve for u(i+1)
    u(i+1) = phat/khat;

    % Calculate velocity and acceleration
    v(i) = (u(i+1)-u_i)/(2*dt);
    A(i) = (u(i+1)-2*ui + u_i)/(dt^2);

    % Reset "in" for first iteration
    in = 0;
end
```

Appendix C

Abaqus .inp code

Below is the .inp input code for the Abaqus finite element model. The inclusion of the model's mesh was removed to save space.

```
*Heading
** Job name: Inputfileappendix Model name: Model-1
** Generated by: Abaqus/CAE 2019
*Preprint, echo=NO, model=NO, history=NO, contact=NO
**
** PARTS
**
*Part, name=Spont
*End Part
**
*Part, name=Sten
*End Part
**
**
** ASSEMBLY
**
*Assembly, name=Assembly
**
*Instance, name=Spont-1, part=Spont
*End Instance
**
*Instance, name=Sten-1, part=Sten
0.348500030469895,           0.,        -0.237
*End Instance
**
*Element, type=CONN3D2
1,  , *Connector Section, elset=Wire-2-Set-1, behavior=Cartesian4
Cartesian,
"Datum csys-1",
*Element, type=CONN3D2
2,  , *Connector Section, elset=Wire-14-Set-1, behavior=Cartesian5
Cartesian,
"Datum csys-1",
*Element, type=CONN3D2
3,  , *Connector Section, elset=Wire-15-Set-1, behavior=Cartesian6
```

```
Cartesian,
"Datum csys-1",
*Element, type=CONN3D2
4,  , *Connector Section, elset=Wire-16-Set-1, behavior=Cartesian7
Cartesian,
"Datum csys-1",
*Element, type=CONN3D2
5,  , *Connector Section, elset=Wire-17-Set-1, behavior=Cartesian8
Cartesian,
"Datum csys-1",
*Element, type=CONN3D2
6,  , *Connector Section, elset=Wire-18-Set-1, behavior=Cartesian9
Cartesian,
"Datum csys-1",
*Element, type=CONN3D2
7,  , *Connector Section, elset=Wire-19-Set-1, behavior=Cartesian10
Cartesian,
"Datum csys-1",
*Element, type=CONN3D2
8,  , *Connector Section, elset=Wire-20-Set-1, behavior=Cartesian11
Cartesian,
"Datum csys-1",
*Element, type=CONN3D2
9,  , *Connector Section, elset=Wire-21-Set-1, behavior=Cartesian12
Cartesian,
"Datum csys-1",
*Element, type=CONN3D2
10,  , *Connector Section, elset=Wire-5-Set-1, behavior=Cartesian3
Cartesian,
"Datum csys-1",
*Elset, elset=Allaconnectors, generate
  1,  10,   1
*Elset, elset=Wire-2-Set-1
 1,
*Elset, elset=Wire-5-Set-1
 10,
*Elset, elset=Wire-14-Set-1
 2,
*Elset, elset=Wire-15-Set-1
 3,
*Elset, elset=Wire-16-Set-1
 4,
*Elset, elset=Wire-17-Set-1
 5,
*Elset, elset=Wire-18-Set-1
 6,
*Elset, elset=Wire-19-Set-1
 7,
```

```
*Elset, elset=Wire-20-Set-1
 8,
*Elset, elset=Wire-21-Set-1
 9,
*Orientation, name="Datum csys-1"
          1.,           0.,           0.,           0.,           1.,           0.
1, 0.
*Element, type=MASS, elset=Mass_noder_Dynamic_mass_
*Mass, elset=Mass_noder_Dynamic_mass_
273.,
*End Assembly
*Connector Behavior, name=Cartesian4
*Connector Elasticity, component=3
 2.1e+06,
*Connector Plasticity, component=3
*Connector Hardening, definition=TABULAR
5250.,0.,0.
*Connector Behavior, name=Cartesian5
*Connector Elasticity, component=3
 1.136e+06,
*Connector Plasticity, component=3
*Connector Hardening, definition=TABULAR
2840.,0.,0.
*Connector Behavior, name=Cartesian6
*Connector Elasticity, component=3
896000.,
*Connector Plasticity, component=3
*Connector Hardening, definition=TABULAR
2240.,0.,0.
*Connector Behavior, name=Cartesian7
*Connector Elasticity, component=3
528000.,
*Connector Plasticity, component=3
*Connector Hardening, definition=TABULAR
1320.,0.,0.
*Connector Behavior, name=Cartesian8
*Connector Elasticity, component=3
368000.,
*Connector Plasticity, component=3
*Connector Hardening, definition=TABULAR
920.,0.,0.
*Connector Behavior, name=Cartesian9
*Connector Elasticity, component=3
534800.,
*Connector Plasticity, component=3
*Connector Hardening, definition=TABULAR
1337.,0.,0.
*Connector Behavior, name=Cartesian10
```

```
*Connector Elasticity, component=3
820000.,
*Connector Plasticity, component=3
*Connector Hardening, definition=TABULAR
2050.,0.,0.
*Connector Behavior, name=Cartesian11
*Connector Elasticity, component=3
 1.32e+06,
*Connector Plasticity, component=3
*Connector Hardening, definition=TABULAR
3300.,0.,0.
*Connector Behavior, name=Cartesian12
*Connector Elasticity, component=3
 1.9e+06,
*Connector Plasticity, component=3
*Connector Hardening, definition=TABULAR
4750.,0.,0.
*Connector Behavior, name=Cartesian3
*Connector Elasticity, component=3
 3.76e+06,
*Connector Plasticity, component=3
*Connector Hardening, definition=TABULAR
9400.,0.,0.
*Amplitude, name=Period, definition=PERIODIC
1,           257.61,              0.,                0.
             0.,              1.
**
** MATERIALS
**
*Material, name=Jord
*Density
2300.,
*Elastic
 9e+08, 0.3
*Plastic
1.,0.
*Material, name=Stål
*Damping, beta=3.03e-05
*Density
7800.,
*Elastic
 2.1e+11, 0.3
*Plastic
 3.55e+08,0.
*Material, name=Sten
*Density
2650.,
*Elastic
```

```
 5e+10, 0.2
**
** INTERACTION PROPERTIES
**
*Surface Interaction, name="Sten friktion"
*Friction
 1e+08,
*Surface Behavior, pressure-overclosure=HARD
**
** PREDEFINED FIELDS
**
** Name: Predefined Field-1   Type: Velocity
*Initial Conditions, type=VELOCITY
Velocity_bc, 3, 0.4
** ----------------------------------------------------------------
**
** STEP: Explicit
**
*Step, name=Explicit, nlgeom=YES
*Dynamic, Explicit
, 0.5
*Bulk Viscosity
0.06, 1.2
**
** BOUNDARY CONDITIONS
**
** Name: Lateral_bc Type: Displacement/Rotation
*Boundary
Lateral_bc, 1, 1
Lateral_bc, 2, 2
** Name: Sten Type: Displacement/Rotation
*Boundary
Sten_bc, 1, 1
Sten_bc, 2, 2
Sten_bc, 3, 3
**
** LOADS
**
** Name: Dynmassa   Type: Surface traction
*Dsload, op=NEW, follower=NO, constant resultant=YES
Clamp, TRVEC, 600863., 0., 0., -1.
** Name: Gravity   Type: Gravity
*Dload
Gravity, GRAV, 9.81, 0., 0., -1.
** Name: Static   Type: Surface traction
*Dsload, op=NEW, follower=NO, constant resultant=YES
Clamp, TRVEC, 250410., 0., 0., -1.
** Name: Surcharge   Type: Surface traction
```

```
*Dsload, op=NEW, follower=NO, constant resultant=YES
Clamp, TRVEC, 750000., 0., 0., -1.
** Name: Vibro   Type: Surface traction
*Dsload, op=NEW, amplitude=Period, follower=NO, constant resultant=YES
Clamp, TRVEC, 9.954e+06, 0., 0., -1.
**
** INTERACTIONS
**
** Interaction: Stenfriktion
*Contact, op=NEW
*Contact Inclusions, ALL EXTERIOR
*Contact Property Assignment
 ,  , "Sten friktion"
**
** OUTPUT REQUESTS
**
*Restart, write, number interval=1, time marks=NO
**
** FIELD OUTPUT: Whole model
**
*Output, field, time interval=0.001
*Node Output
A, U, V
*Element Output, directions=YES
S,
*Contact Output
CFORCE,
**
** FIELD OUTPUT: Connector
**
*Element Output, elset=Allaconnectors, directions=YES
CTF,
**
** HISTORY OUTPUT: H-Output-1
**
*Output, history, variable=PRESELECT, time interval=0.001
**
** HISTORY OUTPUT: Connector
**
*Output, history, time interval=0.0025
*Element Output, elset=Allaconnectors
CTF1, CTF2, CTF3, CTM1, CTM2, CTM3
*End Step
```